2019

CHARACTERIZATION OF NANOSTRUCTURE, MATERIALS, AND ELECTRON EMISSION PERFORMANCE OF NEXT-GENERATION THERMIONIC SCANDATE CATHODES

Xiaotao Liu
University of Kentucky, 656638650@qq.com
Author ORCID Identifier:
https://orcid.org/0000-0003-1603-4566
Digital Object Identifier: https://doi.org/10.13023/etd.2019.034

STUDENT AGREEMENT:

I represent that my thesis or dissertation and abstract are my original work. Proper attribution has been given to all outside sources. I understand that I am solely responsible for obtaining any needed copyright permissions. I have obtained needed written permission statement(s) from the owner(s) of each third-party copyrighted matter to be included in my work, allowing electronic distribution (if such use is not permitted by the fair use doctrine) which will be submitted to UKnowledge as Additional File.

I hereby grant to The University of Kentucky and its agents the irrevocable, non-exclusive, and royalty-free license to archive and make accessible my work in whole or in part in all forms of media, now or hereafter known. I agree that the document mentioned above may be made available immediately for worldwide access unless an embargo applies.

I retain all other ownership rights to the copyright of my work. I also retain the right to use in future works (such as articles or books) all or part of my work. I understand that I am free to register the copyright to my work.

REVIEW, APPROVAL AND ACCEPTANCE

The document mentioned above has been reviewed and accepted by the student's advisor, on behalf of the advisory committee, and by the Director of Graduate Studies (DGS), on behalf of the program; we verify that this is the final, approved version of the student's thesis including all changes required by the advisory committee. The undersigned agree to abide by the statements above.

Xiaotao Liu, Student

Dr. T. John Balk, Major Professor

Dr. Matthew J. Beck, Director of Graduate Studies

CHARACTERIZATION OF NANOSTRUCTURE, MATERIALS, AND ELECTRON EMISSION PERFORMANCE OF NEXT-GENERATION THERMIONIC SCANDATE CATHODES

DISSERTATION

A dissertation submitted in partial fulfillment of the
requirements for the degree of Doctor of Philosophy in the
College of Engineering
at the University of Kentucky

By
Xiaotao Liu
Lexington, Kentucky
Director: Dr. T. John Balk, Professor of Chemical and Materials Engineering
Lexington, Kentucky
2019

ABSTRACT OF DISSERTATION

CHARACTERIZATION OF NANOSTRUCTURE, MATERIALS, AND ELECTRON EMISSION PERFORMANCE OF NEXT-GENERATION THERMIONIC SCANDATE CATHODES

Scandate cathodes, where scandia is added to the tungsten cathode pellets, have recently received substantial and renewed research interest owing to significantly improved electron emission capabilities at lower temperatures, as compared with conventional dispenser cathodes. However, there are several persistent issues including non-uniform electron emission, lack of understanding regarding scandium's role in the emission mechanism, and unreliable reproducibility in terms of scandate cathode fabrication. As a result, scandate cathodes have not yet been widely implemented in actual vacuum electron devices (VEDs).

The surface structure and chemical composition of multiple scandate cathodes – prepared with the powder using the liquid-solid (L-S) technique – and exhibiting excellent emission behavior were characterized to give insight into the fundamental mechanism(s) of operation. This was achieved with high-resolution electron microscopy techniques that include high-precision specimen lift-out. These studies showed that the micron-sized tungsten particles that compose the largest fraction of the cathode body are highly faceted and decorated with nanoscale Ba/BaO (~10 nm), as well as larger (~150 nm) Sc_2O_3 and $BaAl_2O_4$ particles. The experimentally identified facets were confirmed through Wulff analysis of the tungsten crystal shape and were determined to consist of {110}, {100}, and {112} facets, in increasing order of surface area prevalence. Furthermore, it is estimated that Ba atoms decorating the tungsten crystal surfaces are present in quantities such that monolayer coverage is possible at elevated temperatures.

The high-resolution electron microscopy techniques used to investigate the cross section (near-surface) of the L-S scandate cathodes also revealed that the $BaAl_2O_4$ particles (100-500 nm) that attach to the larger tungsten particles are either adjacent to the smaller Sc_2O_3 nanoparticles or encompass them. Furthermore, high-resolution chemical analysis and 3D elemental tomography show that the two oxides always appear to be physically distinct from each other, despite their close proximity. 3D elemental tomography also showed that the Sc_2O_3 particles can sometimes appear inside the larger tungsten particles, but are inhomogeneously distributed. Nanobeam electron diffraction confirmed that the crystal structure of the tungsten particles are body-centered cubic, and imply that the structure remains unchanged despite the numerous complex chemical reactions that take place throughout the impregnation and activation procedures.

The role of Sc and the emission mechanism for scandate cathodes are discussed. Based on characterization results and materials computation, the role of Sc in scandate cathodes is possibly related to tuning the partial pressure of oxygen in order to establish an oxygen-poor atmosphere around the cathode surface, which is a necessary condition for the formation of the (near) equilibrium tungsten shape. A thin Ba-Sc-O surface layer (~8

nm) was detected near the surface of tungsten particles, using electron energy loss spectroscopy in the scanning transmission electron microscope. This stands in stark contrast to models invoking a ~100 nm Ba-Sc-O semiconducting surface layer, which are broadly discussed in the literature. These results provide new insights into understanding the emission mechanism of scandate cathodes.

KEYWORDS: Scandate cathodes, surface features, facets, emission testing, internal microstructure, emission mechanism

Xiaotao Liu

(Name of Student)

03/06/2019

Date

CHARACTERIZATION OF NANOSTRUCTURE, MATERIALS, AND ELECTRON EMISSION PERFORMANCE OF NEXT-GENERATION THERMIONIC SCANDATE CATHODES

By
Xiaotao Liu

Dr. T. John Balk
Director of Dissertation

Dr. Matthew J. Beck
Director of Graduate Studies

03/06/2019
Date

ACKNOWLEDGMENTS

During the period of my PhD. study, there are many people who helped me quite a lot in both the academical research and daily life. It would not be possible for the dissertation without their kind assistance and support.

Firstly, I would like to sincerely thank my advisor Dr. T. John Balk. It is unforgettable for the past several years that I worked in your research group. Many thanks to your guidance throughout my doctoral study which has proved invaluable and helped me a lot for doing research. Thanks for all your advices, suggestions and discussions in every meeting that we had and thanks for all your efforts that you made for working on all the papers. I know that it is a tremendous amount of work especially for reviewing and improving the manuscripts sentence by sentence. I also appreciate your encouragement when I was making presentations on academic conferences.

I would also like to thank Dr. Matthew J. Beck, Dr. Stephen E. Rankin and Dr. Julius M. Schoop, the members of my doctoral committee. Thanks for your consent to become my committee members and thanks for your time and efforts reviewing my dissertation and attending my defense. I also thank Dr. Beth S. Guiton, I really appreciate that you agreed to attend my doctoral defense as the outside examiner.

Special thanks to my labmates as well as friends: Nicolas Briot, Tyler Maxwell, Michael Detisch, Artashes Ter-Isahakyan, Azin Akbari, Maria Kosmidou and Xiaomeng Zhang and other members. I do have a great time with you and I appreciate all your help and collaboration during my Ph.D. I also want to thank Dr. Dali Qian who helped me a lot in operating the transmission electron microscopy. I also thank Dr. Qunfei Zhou for her

useful discussions and suggestions for my research and Bernard K. Vancil (e beam, inc.) for providing the scandate cathode samples.

Lastly, I would like to thank my family for their love, support and encouragement. Thanks to my beloved parents, without your support I won't finish my doctoral study. Thanks to my other family members, they are my brother, my sister-in-law, my sister, my niece and my nephew. Especially for my brother, thank you a lot for taking a good care of our parents, and let me focus on my study in the united states.

I also want to acknowledge the Defense Advanced Research Projects Agency (DARPA) where this project (under the grant number of N66001-16-1-4041) is funded and the Electron Microscopy Center at University of Kentucky where I performed majority of my experiments and gained a lot of hands-on skills for materials characterization.

TABLE OF CONTENTS

ACKNOWLEDGMENTS iii

LIST OF TABLES viii

LIST OF FIGURES ix

CHAPTER 1. Introduction 1

1.1 Motivation and objective of this research 1

1.2 Outline of this work 1

CHAPTER 2. Bachground 3

2.1 Historical development of thermionic cathodes 3

2.2 B type cathodes 4

2.2.1 Development and fabrication of B type cathodes 4

2.2.2 Physical model for B type cathodes 5

2.3 M type cathodes 7

2.3.1 Development of M type cathodes 7

2.3.2 Emission level and issues of M type cathodes 8

2.3.3 Emission mechanism of M type cathodes 9

2.4 Various Scandate cathodes 11

2.4.1 Development of scandate cathodes 11

2.4.2 Pressed scandate Cathode 12

2.4.3 Top-layer scandate Cathode 13

2.5 Impregnated scandate cathodes 14

2.5.1 Fabrication of impregnated scandate cathodes 15

2.5.1.1 L-S and L-L doping techniques 15

2.5.1.2 Fabrication of scandate cathodes 18

2.5.2 Configuration of scandate cathodes 18

2.6 Emission properties of scandate cathodes 20

2.7 Emission models for scandate cathodes 21

2.7.1 Model of Ba-Sc-O monolayer 22

2.7.2 Model of 100 nm Ba-Sc-O surface layer 25

2.8 Unsolved issues for scandate cathodes 27

CHAPTER 3. Materials and methodes 29

3.1 Fabrication of precursor powder and scandate cathodes 29

3.1.1 Preparation of liquid-solid (L-S) powder 29

3.1.2 Preparation of liquid-liquid (L-L) powder 30

3.1.3 Scandate cathodes fabrication 30
3.2 Materials Characterization.....31
3.2.1 SEM 31
3.2.2 EDS 32
3.2.3 EBSD and TKD 32
3.2.4 XRD 35
3.2.5 XPS 36
3.2.6 TEM lamella preparation 37
3.2.7 (S)TEM.....40
3.2.8 3D reconstruction.....41
3.2.9 Emission testing.....42
3.2.10 Wulff analysis on crystal shapes.....43
CHAPTER 4.Scandate cathode surface characterization: Emission testing, elemental analysis and morphological evaluation 44
4.1 Introduction 44
4.2 Material and methods.....46
4.3 Results and discussion.....48
4.3.1 Emission testing.....48
4.3.2 Characterization of cathode surface morphology.....49
4.3.3 Chemical analysis 60
4.3.4 Quantifying the amount of Ba on W surfaces 63
4.3.5 XRD, XPS and TEM analysis 69
4.3.6 Characteristics of scandate cathodes and possible role of scandium 76
4.4 Conclusions 76
CHAPTER 5. Near-surface material phases and microstructure of scandate Cathodes…79
5.1 Introduction 79
5.2 Materials and methods 81
5.3 Results 82
5.3.1 Surface morphology of scandate cathodes 82
5.3.2 Elemental analysis of phases in cross-section samples 84
5.3.3 Confirmation of crystal structure of W grains 94
5.3.4 3D tomographic reconstruction 96
5.4 Discussion.....99
5.5 Conclusions 102
CHAPTER 6.Studying on L-L scandate cathodes: Probing the Ba-Sc-O surface layer and 3D tomography……..…104
6.1 Introduction 104

6.2 Materials and methods 105

6.3 Results 107
6.3.1 Surface morphologies of L-L scandate cathodes.....107
6.3.2 Emission performance of L-L scandate cathodes.....110
6.3.3 Probing the Ba-Sc-O surface layer 110
6.3.4 TKD and TEM tomography 115

6.4 Discussion.....118

6.5 Conclusions 119

CHAPTER 7. Surface microstructural comparison between poisoned and well emitted scandate cathodes……..121

7.1 Introduction 121

7.2 Materials and methods 122

7.3 Results and Discussion.....123
7.3.1 Emission curves of the poisoned scandate cathode 123
7.3.2 Morphology and surface particles identification 124
7.3.3 Chemical analysis on surface decorating particles 126
7.3.4 Faceting and rounding behavior of poisoned scandate cathode 129

7.4 Conclusions 132

CHAPTER 8. Conclusions and future work.....134

APPENDIX. Terms in thermionic dispenser cathodes.....140

Vita……158

LIST OF TABLES

Table 4.1 Computed values of relative surface energy and proportion of total surface area for each facet type, based on the ideal crystal shape from the Wulff analysis (see Fig. 4a). Normalized surface energy is reported with respect to the surface energy of a {100} facet……...……..56

Table 4.2 Measured and calculated values related to the amount of Ba on the surface of W. The existence of metallic Ba or oxidized BaO was considered, including calculation of the corresponding surface density of Ba adatoms in each case. This also allowed the determination of how many W unit cells are associated with one Ba adatom, for each combination of W facet orientation and Ba/BaO material phase……..……67

Table 5.1 Quantified measurement of particle composition, obtained from EDS point analysis of the regions marked in Fig. 5.6……..93

Table 7.1 Quantified results of the surface particles of the poisoned scandate cathode…….……128

LIST OF FIGURES

Figure 2.1 Historical perspectives of thermionic cathodes emission capabilities [1]……4

Figure 2.2 Model of impregnated tungsten cathode showing changes with time during life [2].……..…….....7

Figure 2.3 Auger spectrum of a normal Os-Ru coated M type cathode [3]……10

Figure 2.4 Reduction process from tungsten oxide to tungsten [4]…….16

Figure 2.5 SEM images of scandia doped tungsten powders by L-S doping method (a), and by Sol-Gel doping technique (b) [4]……..…..…….....17

Figure 2.6 A schematic diagram of a dispenser cathode (a) [5], and an image of a real scandate cathode (b)……...……..19

Figure 2.7 Typical Cross section of a scandate cathode [6]……....……..20

Figure 2.8 Schematic of the Ba-Sc-o monolayer model. The inset on upper-right corner shows a typical auger electron spectrum of the W-Sc_2O_3 containing film [7]……..……22

Figure 2.9 Change in surface atom concentration as a result of heat-treatment at 1150 $^{\circ}C_b$ evaluated by Auger electron spectroscopy. Auger intensity ration with respect to W is measured for a (W- $Sc_2W_3O_{12}$) coated cathode (impregnated) and a nonimpregnated cathode sample (not impregnated) [8]……..……..23

Figure 2.10 Change in electron emission of W-scandia cathodes by activation heating at 1150 $^{\circ}C_b$. The cathode diameter is 1.23 mm and the distance of a cathode and an anode is 7mm [7]…….…….…….24

Figure 2.11 Surface elemental depth profiles of a scandate cathode developed by Wang's group [9]……..26

Figure 2.12 Diffusion of Sc, Ba and O during activation and surface migration of Ba, Sc along the surface. (a) Changes of AES atomic concentration ratios of Sc/W, Ba/W and O/W during activation. (b) Variation of Auger peak-to-peak height (APPH) ratios of Ba/W and Sc/W from pore to W grain [9]……...27

Figure 3.1 L-S precursor powder in which Sc_2O_3 fails to adhere well, forms Sc_2O_3clumps (a) and tungsten particles with insufficient Sc_2O_3 (b) [10]…….....30

Figure 3.2 Schematic diagram for EBSD observation [11]…….……34

Figure 3.3 Set-up configuration of TKD in a SEM chamber [12]……35

Figure 3.4 Procedures of TEM sample preparation using a FIB……..39

Figure 3.5 Cathode with a guard ring……..……42

Figure 4.1 CSD test results for three cathodes investigated here. Emission current as a function of cathode (W pellet) brightness temperature ($°C_b$). The knee temperatures were 820 $°C_b$, 837 $°C_b$ and 822 $°C_b$……..……49

Figure 4.2 SEM micrographs acquired on a typical surface region of a scandate cathode. (a) and (b) Low-magnification images showing a flat surface with visible cracks. (c) Secondary electron (SE) micrograph and (d) corresponding backscattered electron (BSE) micrograph. (e) SE and (f) BSE image pair at higher magnification, showing faceted and equiaxed W particles, with nanoparticles decorating the facets……...…51

Figure 4.3 Size distribution of W particles, as measured on scandate cathode surfaces. The average size of W particles (d_c) was 1.17 μm, as fitted by a lognormal function….....53

Figure 4.4 Wulff construction of ideal W crystal shape utilizing Wulffmaker. (a) Calculated crystal shape for W that matches experimentally observed grains. (b) SEM image of W particle in the same orientation as the Wulff shape in (a), showing agreement between experiment and calculation. (c) and (d) Two additional W particles with different orientation, both of which match the same calculated Wulff shape when rotated appropriately (inset) ……54

Figure 4.5 Quantitative characterization of Ba/BaO nanoparticles on various facets of W particles. (a) Typical SEM micrograph of faceted W, with calculated crystal shape (inset). (b) Average number of Ba/BaO nanoparticles on each facet type, for the W particle in image (a). Based on measurements of 15 tungsten particles, (c) areal density of Ba/BaO nanoparticles and (d) average size of Ba/BaO nanoparticles, for each facet type……...58

Figure 4.6 SEM micrographs for measurement of steps within microfaceted regions between adjacent facet pairs. Representative examples of these microfacets are shown for (a) {100}/{112} facets, (b) {110}/{112} facets, and (c) {112}/{112} facets. 21 W particles were observed, and the number of steps within each microfaceted region was counted, with average normalized results presented in the bar chart of (d)…..……60

Figure 4.7 SEM images and EDS spectra of the two types of larger (~100 nm) oxide nanoparticles that exist on the tungsten surfaces of scandate cathodes. (a)

Image acquired in SE mode for a typical surface area, and (b) the corresponding BSE image of the same area. EDS spectra for the different oxide particles, indicated by black arrows as (c) particle A and (d) particle B…….…….62

Figure 4.8 EDS elemental map of a typical scandate cathode surface area. An SEM micrograph (BSE imaging mode) is shown at upper left, and a composite map showing the distribution of all relevant elements is shown at upper right. Additionally, individual maps indicate the elemental distributions of W, Sc, O, Ba and Al…….……....63

Figure 4.9 Schematic of the proposed transformation model, illustrating the reorganization of Ba adatoms on the W facets of a scandate cathode. During cooling, the surface layer of Ba atoms transforms into discrete nanoparticles that decorate the W facets. These nanoparticles would subsequently oxidize upon exposure to air……...……...…65

Figure 4.10 Theoretical positions of Ba adatoms on {100}, {110} and {112} W surface facets. (a) Unit cell of W. The relevant surface structures are shown for each facet: (b) the {100} surface plane; (c) the {110} surface plane; (d) the {112} surface plane. Red rectangles indicate unit cells on the W surface for {100}, {110}and {112} orientations, while yellow rectangles represent unit cells for adsorbed Ba (two Ba atoms lie within each of these unit cells). In all cases, four W unit cells are required to accommodate two Ba atoms, for complete coverage of Ba atoms on the W surface…….……..…….69

Figure 4.11 XRD scan of the scandate cathode. The peaks detected here were all attributed to the BCC tungsten phase; no oxide peaks were observed……..…...70

Figure 4.12 XPS spectra for relevant elements expected to exist on the scandate cathode surface. (a) Ba 3d, (b) Al 2p, (c) O1s, (d) Sc 2p, (e) Ca 2p and (f) W 4f…....72

Figure 4.13 TEM observations of a lift-out lamella from a scandate cathode. (a) Low-magnification bright-field image. (b) Higher-magnification image of W particle denoted by red dashed rectangle in (a). Facets are indicated by arrows. Two Pt layers were deposited on the W surface, denoted as Pt-e and Pt-i, to protect the cathode surface during FIB milling. The inset in (b) is a selected-area electron diffraction pattern of the W grain, at location B, indicating the presence of BCC W. (c) High-angle annular dark field STEM image showing atomic number contrast, with uniform brightness up to the surface of the W grain. (d) Bright-field TEM image reveals microfacets on the W surface. No Ba-Sc-O surface oxide layer was observed here. The layer seen at the lower edges of the central W grains (blue arrow in image (b), also visible in image (c)) is redeposited W from FIB milling, and is only observed on surfaces that were not protected by Pt……..……..……...75

Figure 5.1 Surface morphology of two scandate cathodes. (a) and (b) are low- and high-magnification SEM images of the surface of cathode #1. (c) and (d) are low- and high- magnification SEM micrographs of cathode #2. All micrographs were obtained in secondary electron imaging mode……..…84

Figure 5.2 EDS elemental mapping of a cross-section TEM lamella from scandate cathode #1. (a) Low-magnification HAADF image of the electron-transparent sample region; (b) composite elemental map showing the distribution of W (red), Ba (blue) and Sc (green) in the TEM lamella; (c)-(h) elemental distribution maps for W, Sc, Ga, Ba, Al and O……86

Figure 5.3 Structural and elemental analysis of a Ba-Al-O particle at the cathode surface. (a) HAADF image, with green square showing the area for EELS mapping, as well as blue and yellow boxes showing sites for EDS analysis of the Ba-Al-O particle and neighboring W grain, respectively; (b) selected area diffraction pattern acquired from the Ba-Al-O particle; (c)-(f) EELS elemental maps of O, Al, Ba and W; these four maps share the same scale bar……...……..……....88

Figure 5.4 EDS elemental analysis of a Ba-Al oxide particle that also exhibits an encased Sc signal. (a) Low-magnification HAADF image of near-surface region of the cathode sample; (b) high- magnification HAADF image showing the area scanned for EDS mapping, which corresponds to the red box in image (a); (c) composite elemental map showing distributions of W, Ba and Sc; (d)-(h) individual elemental maps of W, Ba, Al, O and Sc, where the red box in (h) outlines the region of EDS quantitative measurement……..89

Figure 5.5 (a) HAADF image of near-surface cathode region where structure and elemental distribution were investigated by tomography. (b)-(e) HAADF image and EDS elemental maps, shown as 2D slices from the 3D tomogram, of a Ba-Al oxide particle that encases a smaller Sc-containing particle and

sits on a W grain. Sc is distinct from both the W particle and the Ba-Al oxide……90

Figure 5.6 High spatial resolution EDS elemental mapping of Ba-Al oxide and adjacent Sc-containing particle. (a) Low-magnification HAADF image; (b) high-magnification HAADF image of area mapped by EDS, corresponding to red box in image (a), blue and yellow boxes denote locations of EDS point analysis; (c)-(g) elemental maps of Sc, Ca, Ba, Al and O. (b)-(g) share the same scale bar……...……..92

Figure 5.7 High spatial resolution characterization of a Sc-containing particle located in the interior region of a W grain. (a) Low-magnification HAADF image showing the near-surface region of the cathode; (b) zoomed HAADF micrograph corresponding to the red box in (a). Inset in (b) are a HAADF image and W elemental distribution map, revealing nanoscale W particles within the 100 nm Sc-containing particle……...…….94

Figure 5.8 Crystal structure of the W matrix in scandate cathode #1, characterized using scanning nanobeam diffraction. It is demonstrated that the W matrix has the BCC structure, which is inferred from diffraction patterns obtained at locations ranging from the middle of the W grain to its surface. The beam direction and zone axis for the grain orientation shown here are indexed as [-111]……...……95

Figure 5.9 Schematic illustration of the sample, ion beam and electron beam for serial sectioning in the FIB-SEM, in order to perform 3D tomographic reconstruction……....97

Figure 5.10 3D reconstruction of a W particle from scandate cathode #2, generated by FIB serial sectioning and imaging in the SEM. (a) Secondary electron SEM micrograph of the selected W particle, (b) reconstructed tomogram, and (c) spatial distribution of Sc/Sc_2O_3 inside the W particle. Note that the viewing direction of image (c) is rotated with respect to that of images (a) and (b)…98

Figure 5.11 SEM micrographs of (a) tungsten powder and (b) scandia-doped tungsten powder. Both images were recorded in secondary electron imaging mode……...99

Figure 6.1 Back-scattered electron micrographs of scandate cathodes. Images are acquired with a FIB-SEM under the immersion mode. (a) and (b) from the cathode #1, (c) and (d) from the cathode #2……..……108

Figure 6.2 Figure 6.2 SEM images of scandate cathodes. (a), (b) a pair of SEM images from an L-S scandate cathode, (c), (d) are from an L-L scandate cathode #2. The insets in (b) and (d) are the corresponding Wulff shapes……109

Figure 6.3 Plots of current versus brightness temperature (W)……110

Figure 6.4 Nano-AES analysis on surface elemental distribution scandate cathode #1..112

Figure 6.5 EELS chemical maps and corresponding electron energy loss spectrum. (a) HAADF image, green box inside indicates the area for EELS analysis; (b)

layered chemical map showing Sc and Ba; (c), (d) and (e) maps of Sc, O and Ba; (f) electron energy loss spectrum……..…..…..113

Figure 6.6 Nano-beam diffraction study on crystal structure of the Ba-Sc-O surface layer. (a) STEM image of a partial tungsten grain with the surface layer; (b)-(e) diffraction patterns correspond to the sites of B-E as indicated in image (a)……...115

Figure 6.7 TKD results on a lamella extracted from L-L scandate cathode #2. (a) Forescatter diodes (FSD) image, (b) inverse pole figure and (c) phase map……..……..116

Figure 6.8 3D tomography on a lamella extracted from L-L scandate cathode #2. (a)-(e) 3D elemental distribution of Ba, Al, Sc, O and W, (f) 3D layered map. Note that the volume (x, y, z) = (906, 875, 133) nm……..…….117

Figure 6.9 Back-scattered electron images of L-L scandia doped tungsten powder. (a) BSE image showing tungsten particles with scandia coverage, (b) cleaved surface of one tungsten particle showing internal pores with filled by scandia nanoparticles……..118

Figure 7.1 Emission curves of the poisoned scandate cathode. Black curve is the measurement at 0 hour while the red curve is after 4200 hours……124

Figure 7.2 Scanning electron micrographs of the poisoned scandate cathode. (a) and (c) are secondary electron images, (b) and (d) are the corresponding back scattered electron images…….125

Figure 7.3. Size distribution of tungsten particles of poisoned (left) and healthy (right) scandate cathodes……126

Figure 7.4 EDS analyses of the poisoned scandate cathode. (a) SEM image, (b)-(d) relative EDS spectra for particles A, B and the matrix-tungsten……..127

Figure 7.5 EDS mapping on a representative area of the poisoned scandate cathode. (a) SEM image showing the area for mapping, (b) layered image, below is the elemental maps of W, Al, Ba, Sc, O and C…….129

Figure 7.6 (a)-(f) the proposed equilibrium crystal shape in the vicinity of the crystal vertex depends on temperature. (g)-(i) The actual crystal shape observed after quenching. The observed shape depends on the cooling rat and may differ from the equilibrium shape. During quenching small step-like facets may be form as shown in (g) [13]……..130

Figure 7.7 Theoretical and experimental tungsten crystal shape for the poinsoned scandate cathode. (a) [13] Crystal shape follows a function of temperature on the basis of Equilibrium Crystal Shape (ECS), T_v and T_e are vertex-rounding and edge-rounding temperature, respectively. (b) Experimentally observed tungsten shapes form the poisoned scandate cathode, showing vertices rounding and edge rounding……...132

CHAPTER 1. INTRODUCTION

1.1 Motivation and objective of this research

Though scandate cathodes exhibit a great potential to replace the conventional B type cathodes, the most widely implemented electron emitting cathodes even till to date, owing to high current density and a relatively lower operating temperature [6,14,15]. There are still several issues for scandate cathodes, i.e., unclear emission mechanism, low reproducibility for production, and uneven emission etc, have not been resolved before making them practical for applications [1,4,6,16–19]. These problems, to a large extent, are due to the facts that we have yet fully understood the cathode materials at a fundamental level. That is the motivation where this thesis gets started.

In this work, efforts are made to study the materials and nanostructures of scandate cathodes. We aim at gaining a better understanding of the materials constituting the scandate cathodes and then try to elucidate the emission mechanism of them. With achieving more knowledges on scandate cathodes, it is anticipated that the scandate cathodes can be well understood and further improved for meeting the requirements for practical applications, e.g., microwave tubes and, traveling wave tubes (TWT) electron vacuum devices (VEDs) [10,18,20–23].

1.2 Outline of this work

Various scandate cathodes were thoroughly investigated using electron-microscopies based materials characterization techniques, in combination with XRD, XPS and Nanoauger spectroscopy. An outline of this work is described below.

Chapter 1 describes the motivation and objectives of this work.

Chapter 2 talks the research background.

Chapter 3 describes the materials and methods that get involved in this thesis.

Chapter 4 presents the results of surfaces characterization of well emitted scandate cathodes (L-S scandate cathodes, which means the cathodes are made by liquid-solid powder). In this chapter we carefully analyzed the morphological features of tungsten particles constituting cathodes surface, and the surface decorating nanoparticles as well as the crystal structure of the matrix-W.

Chapter 5 reports the near-surface material phases and microstructure of scandate cathodes that exhibited excellent electron emission (L-S scandate cathodes). The microscale or nanoscale particles as observed on cross section samples extracted from scandate cathodes are comprehensively studied for understanding the complex chemical reactions that took place during the impregnation and activation processes.

Chapter 6 presents the results for surface features of well emitted L-L scandate cathodes (L-L scandate cathodes are developed with the liquid-liquid precursor powder). Special attentions are paid to identify the very thin Ba-Sc-O surface layer which is incongruent to the previously proposed models in literature.

Chapter 7 presents the surface features comparison between poisoned and well emitted scandate cathodes. The faceting and rounding behavior of tungsten particles is discussed with respect to temperature dependence and the influence of oxygen pressure.

Chapter 8 talks about conclusions and future work.

CHAPTER 2. BACKGROUND

2.1 Historical development of thermionic cathodes

Thermionic cathodes working as electron emitters to generate electron beams are often considered as a crucial technology and which can be applied widely, ranging from civilian communication to military and space-based technologies like microwave tubes, TWTs, and VEDs [2,6,9]. Though the field of thermionic electron emission is considered a relatively "matured" technology, thermionic cathodes, especially for scandate cathodes, are still being studied a lot in order to meet the demanding requirements for practical applications. In addition, in recent years with the advent of modern surface analytical facilities, e.g., XPS, AES and high-resolution microscopies, it enables one to gain a better understanding of the physics and chemistry of the emitter surface which, in turn, stimulates the research on thermionic cathodes and brings more improvements on them.

Fig. 2.1 shows the changes that have taken place with respect to emission capabilities of various thermionic cathodes in the past decades. It is obviously that scandate cathodes significantly superior to the conventional dispenser cathodes in terms of emission abilities. Note that stable operation in closed spaced diodes (CSD) at 100 A/cm^2 has been routinely obtained for these scandate cathodes as reported in the references [21,24]. Dispenser cathodes means that the so called active materials (low work function compounds) can dispense continuously to the emitting surface from the body of the cathode. Typical dispenser cathodes include tungsten matrix cathode which is known as the B type cathodes and the coated tungsten matrix cathode which is also called as M type cathode. Apart from them, there are some other dispenser cathodes, i.e., mixed metal matrix cathodes, and the controlled porosity cathodes, etc. Comparing with the conventional B

type or M type cathodes, scandate cathodes are capable of delivering a greatly improved current density. However, scandate cathodes have yet been implemented as widely as the B type cathodes since there are still several unsolved issues associated with them.

In this section we will review these three types of representative thermionic cathodes, B type cathodes, M type cathodes and the scandate cathodes.

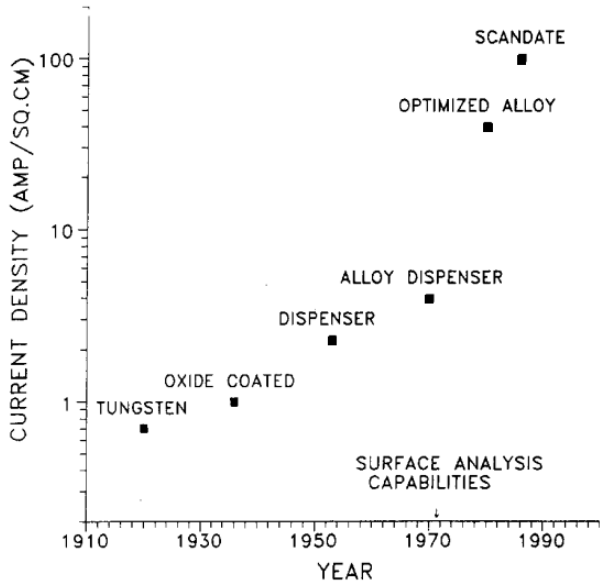

Figure 2.1 Historical perspectives of thermionic cathodes emission capabilities [1].

2.2 B type cathodes

2.2.1 Development and fabrication of B type cathodes

Barium dispenser cathode, usually called as B type cathode, originally termed Philips 'B' cathode which was first developed in about 1955. In history, the Philips 'B' cathode developed from the Philips 'A' cathode which comprises a porous tungsten body with impregnated by barium aluminate and was invited by Levi and Hughes in about 1952 [17]. The fundamental difference between the Philips 'B' and Philips 'A' dispenser cathodes is the impregnated oxides, more specifically, Philips 'B' cathodes use barium calcium

aluminate to replace the barium aluminate that was applied in the Philips 'A' cathodes [17]. The addition of calcium oxide into the impregnant materials is beneficial for mitigating the sublimation rate of Ba and therefore greatly enhances the emission properties. The impregnant of B type cathode is usually 5BaO: 3CaO: $2Al_2O_3$ which is sometimes simply referred as 5-3-2 (mole ratio). The 5-3-2 is the most common impregnant materials for cathodes fabrication while some other various impregnant had been applied, e.g., 6-1-2 and 4-1-1 oxides.

Tungsten powder is the raw materials for cathodes fabrication. Selecting tungsten powder with controlled characteristics, i.e., particle shape, size and distribution and purity of the powder is crucial for the cathodes production. The raw powder is first mixed and then isostatically pressed under a set pressure, 20 000psi for example [17,25]. The next step for the cathode fabrication is sintering. This procedure is carried out by infiltrating the pressed pellet with an inert plastic filler and gets it sintered at a specific temperature. The reason for the infiltration process prior the sintering is to maintain the open-pore structure. After that the next step is the impregnation which is performed by melting the impregnant at the top surface of the porous tungsten matrix in a hydrogen or inert atmosphere. After the completion of this step, the cathodes are then washed using the deionized water for removing the excess impregnant on cathodes surfaces.

2.2.2 Physical model for B type cathodes

As aforementioned B type cathodes are still the most widely used thermionic cathodes due to its current density and long life. B-type cathode has a work function of around 2 eV and an operation temperature of about 1400 K [26,27]. A lot of work has been done to illustrate the work mechanism of this type of cathodes [2,28–32]. In 1978,

Forman proposed a physical model for demonstrating the physical model of barium impregnated cathodes [2]. In the literatures [2,33,34] it is demonstrated that a coadsorbed barium and oxygen layer, rather than barium oxide, on tungsten surface forms a dipole on the emitting surface, leading to the copious electron emission of B type cathodes. The model hypothesized that there is an adsorbed monolayer (or partial monolayer) of barium and oxygen on the surface of a cathode during its life.

The schematic diagram in Fig. 2.2 describes the model of barium impregnated cathodes at different times during its life including early life, middle life and end life [2]. In addition it is thought that only barium continuously migrate to cathode surface from the pores in the matrix. There is no need to bring oxygen from the body to the surface since they assume that oxygen is ample throughout the cathode's life and is always present on the cathode's surface. As Fig. 2.2 displayed in the early life of one cathode, the barium arrival rate to the surface is high enough to maintain monolayer coverage as barium is being generated in pores close to the surface and, moreover, the migrate path is short. As the working hours of the cathode increases, the pores near the surface are depleted. As a result, the arrival rate of barium to the surface is less than that needed to maintain a monolayer. At this time, a partial monolayer will result which is generally described as the time of middle life of cathode. If the work function brought by the partial monolayer is lower than what required to sustain the normal electron emission, the cathode is still working at this period. Eventually at the end of cathode life the arrival rate of barium to cathode surface becomes smaller and smaller, resulting the partial monolayer whose work function is too high to sustain cathode's electron emission. The emission will drop significantly and the cathode runs to the end of its life.

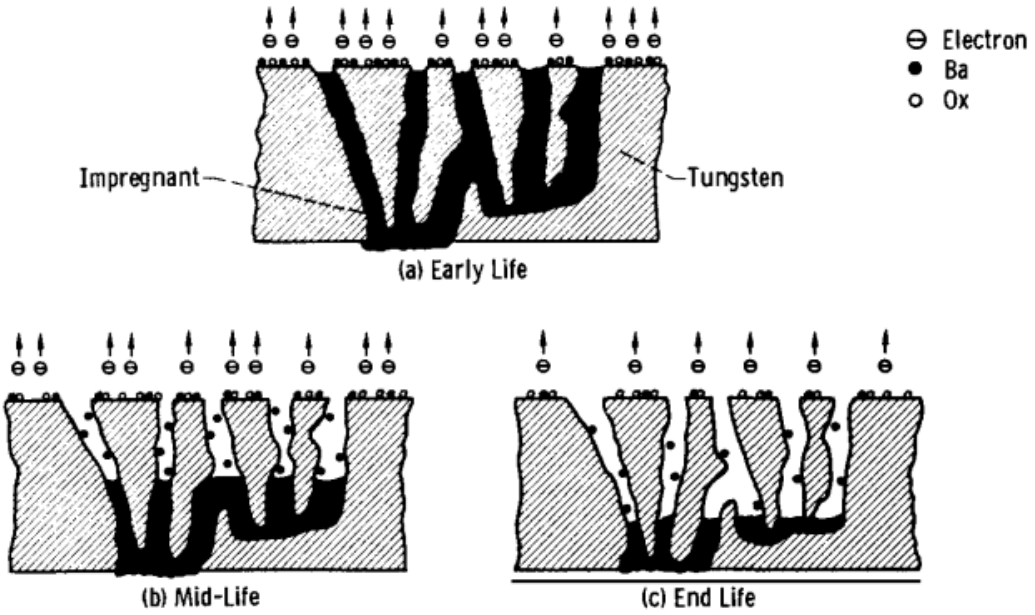

Figure 2.2 Model of impregnated tungsten cathode showing changes with time during life [2].

It should be noted that Ba is produced by the chemical reaction between the impregnant materials and tungsten at sites of pore walls. As an example, for B type cathodes with a 5-3-2 impregnant, the chemical reaction that occurred is [28]:

$$5BaO.3CaO.2Al_2O_3 + \tfrac{3}{4}\,W = 3/4\,Ca_2BaWO_6 + \tfrac{3}{4}\,Ca_2BaAl_2O_6 + 5/4\,BaAl_2O_4 + 9/4\,Ba \quad 2.1$$

2.3 M type cathodes

2.3.1 Development of M type cathodes

With the progress of thermionic cathodes research, in around 1964, scientists in Holland discovered that the emission capability was significantly enhanced by coating the B type cathode with a thin layer of refractory metals, i.e. osmium, iridium or rhenium, which was verified by the U.S. scientists later [17]. It was found that a substantial reduction

in work function of such cathodes (B type cathode coated with a very thin refractory metal layer) can be achieved and therefore the emission level was greatly improved. It is very interesting that the coating-metals, in fact, have a higher work function than that of tungsten but, nevertheless, the overall work function is lower than that of the B type cathode (a pure tungsten base alone). The reason for this phenomenon is that the overall work function of the emission surface constituting by a barium and oxygen layer on the coating is inversely proportional to the work function of the coating materials which serves as the substrate of the emission surface [5,35,36].

In spite of a superior emission level of these cathodes several drawbacks had been found for them later during the production and further research. For instance, during the preparation of the osmium coating, people usually adopt the technique of sputtering (or deposition) where tetroxide applied is very poisonous and consequently very difficult to work with. This problem was later overcome by sputtering an alloy film, e.g. osmium-ruthenium or osmium-iridium, to replace the original refractory single metal film [17]. These cathodes, basically a B type cathode with a coating of osmium-ruthenium or osmium-iridium alloy film is called the M type cathode. A broader conception for M type cathode is B type cathode with a coating of either a refractory single metal film (i.e. Os, Ru, Re) or an alloy film (e.g. Os-Ru, and Os-Ir). The sputtered alloy film of M type cathode is generally with the thickness of 200-500 nm.

2.3.2 Emission level and issues of M type cathodes

As indicated by [25] , the work function of M type cathode could reach approximately 1.8eV which means the cathodes could deliver the same emission as the B type cathode at 100 ˚C lower temperatures. According to the reference [37], the emission current density

of M type cathode is above 10 A/cm^2 during the close spaced diode (CSD) testing, and is above 32 A/cm^2 in pulsed mode during the electron gun testing. This is an impressive enhancement with emission capabilities for thermionic cathodes with respect to the conventional B type cathodes.

Despite the fact that M type cathodes possess a lower work function and therefore a better electron emission level than B type cathodes, there are several issues with them. As suggested by [38], M type cathodes are more easily to get poisoned by various gases though its emission could be recovered by aging them at a vacuum environment. Another problem has yet been solved for M type cathode is the necessity of long initial aging, so the thermal conduction near to the emitting layer may need to be promoted later, i.e. though improving the cathode processing etc.

2.3.3 Emission mechanism of M type cathodes

Thought M type cathodes have been investigated a lot while its emission mechanism has yet been fully understood through literature study [3,27,35,38–40]. As suggested by Hasker [3], there is an excess oxygen concentration which is about two times of the Ba-O concentration (based on Auger analysis, as shown in Fig. 2.3) for a normal activated M type cathode. In addition, for a degraded M type cathode the excess oxygen level is found to be much higher than that for a normal one. In the reference [27] it was implied by Shroff et al that the enhanced emission of M type cathodes was not obtained at the expense of high evaporation rate and, moreover, the improvement does not depend initially upon temperature. Yin et al [39] applied the technique of synchronous radiation photoelectron spectrum to study activated M type cathode and suggested that the spectrum of O exhibited various chemical states with showing three significantly different peaks (530.23 eV, 531.72

eV and 533.45 eV) which correspond to various oxides. In addition, they [39] claimed that the special oxides accelerate the decomposition and evaporation of the oxide layer on cathode surface, leading to produce much more low binding energy oxygen species (O^-) which has a stronger adsorption to Ba^+. As a result, the emission is enhanced as the Ba^+ is regarded as excess barium and is the source of electron emission.

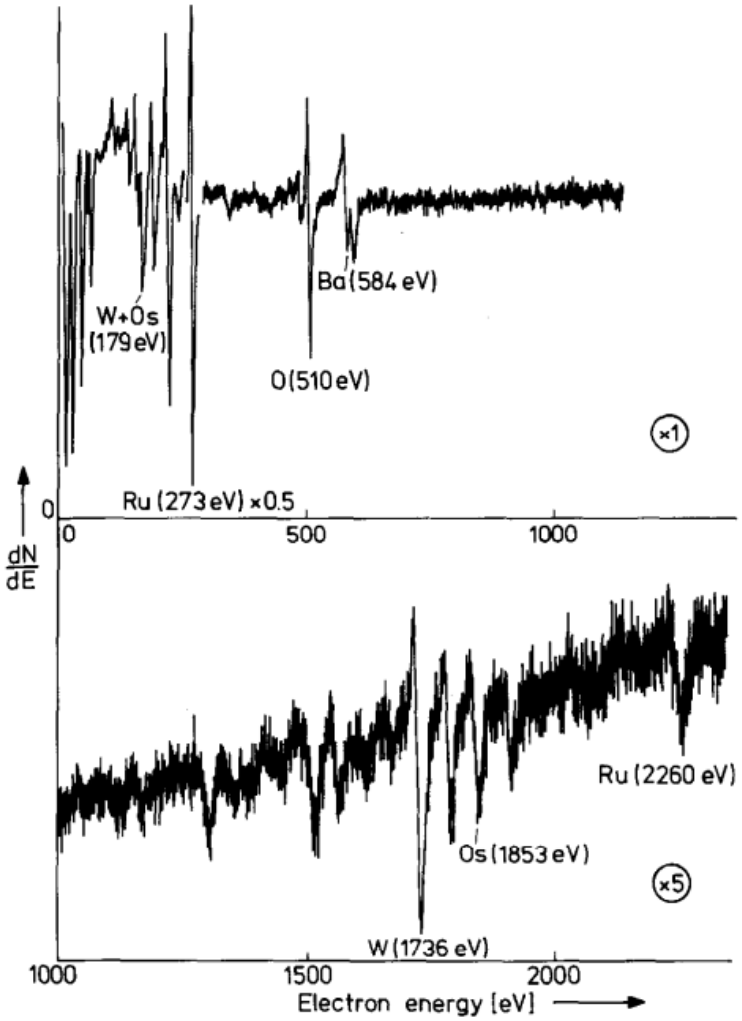

Figure 2.3 Auger spectrum of a normal Os-Ru coated M type cathode [3].

2.4 Various Scandate cathodes

2.4.1 Development of scandate cathodes

Scandate cathodes where scandia is added into the tungsten matrices have attracted significant attention since the late 1970s owing to their excellent electron emission and a lower operating temperature [6,41–50]. Matrices of scandate cathodes are commonly porous pure tungsten pellets while a small portion of scandate cathodes employ alloy matrices (e.g. Re_3W) as reported by the references [42,51,52]. The highest reported emission level of scandate cathode can reach $J_{10\%}$ of 400 A/cm^2 at 965 $^{\circ}C_b$ for a top layered scandate cathode as reported by Gartner et al [53], making it the most promising thermionic cathodes for substituting the conventional ones.

According to the patent of [54] the first reported scandate cathode was developed by Figner in 1967 and was fabricated by mixing the barium scandate ($3BaO.2Sc_2O_3$) with tungsten powder and then followed by a pressing process. It is noted that for this materials system applying impregnation is unfeasible due to the rather high melting temperature of the barium scandate [55]. Later with the change of using a mixture of BaO, CaO, Sc_2O_3 and Y_2O_3 as the materials for impregnation researchers succeed to fabricate some early versioned scandate cathodes. However, one primary drawback of these scandate cathodes is high-cost for the production since rear-earth metal oxides (Sc_2O_3 and Y_2O_3) are expensive [55]. Eventually the impregnant materials comprising BaO, CaO and Al_2O_3 have been widely adopted for the production of scandate cathodes. Using these impregnant materials is economic and, moreover, the temperature required for impregnation is not super high which makes it more readily for the scandate cathode preparation.

The development of scandate cathodes can be divided into two major periods from the perspective of their applications. The first period is between 1970 and 1990 which was motivated by high resolution cathode ray tubes (CRTs). This device requires an emission level of about 10 A/cm^2 (DC current densities) and an low operation temperature (lower than that of B-type cathodes) [5]. Unfortunately, scandate cathodes failed to be successfully used in CTRs as they were replaced by LEDs quickly [5]. The other period started from around 1999 and till to now. This period is stimulated by two primary factors: (1) Vacuum Electron Devices (VEDs) require higher and higher emission current density which cannot be obtained by conventional B type cathodes, the most widely used one, no even to say oxides cathodes, another matured technology; (2) the advent of fantastic surface analytical facilities, e.g. X-ray photoelectron spectroscopy (XPS) and Auger electron spectroscopy (AES), enables one to do more experimental (and theoretical) works to unveil the nature of the emitting surfaces and the emission mechanism. As a result, various types of scandate cathodes, including pressed scandate cathodes [56–59], top layer scandate cathodes [53,60,61] and impregnated scandate cathodes [4,62–64], have been developed and still under investigations. These three types of scandate cathodes will be discussed in more detail later below, special focus is given to the impregnated scandate cathode which is the same type of scandate cathodes investigated in this thesis.

2.4.2 Pressed scandate Cathode

Pressed scandate cathodes (or scandia doped tungsten pressed cathode) is prepared by pressing and sintering a mixture of tungsten powder, scandia and oxides (BaO, CaO and Al_2O_3). Different pressed scandate cathodes may involve dissimilar recipe for the pressed

scandate cathodes fabrication. Only a few articles can be found for pressed scandate cathode research since this kind of scandate cathode is usually serving as a comparison study for impregnated scandate cathodes.

In [65], the starting materials constitute of around 7 wt. % barium scandate and the rest fine grain sized tungsten powder. The mixture of tungsten powder and barium scandate was pressed first and then sintered at nearly 1570 ℃ in a hydrogen atmosphere for about 15 mins. After this process the cathode was smoothly polished and ultrasonically cleaned. The resultant pressed scandate cathode in [65] exhibited excellent emission properties after activation which has a current density of approximately 10 A/cm^2 at the temperature of 950 ℃. Cui et al [59] prepared scandia doped pressed cathode using scandia and barium calcium aluminate co-doped tungsten powder which ranched a current density of 31.5 A/cm^2 at 850 $℃_b$. As discussed in literature, enhanced emission properties of scandia doped pressed cathode is attributed to activated scandium oxide regions on the cathode surface [65] and formed Ba-Sc-O multilayer [59].

2.4.3 Top layer scandate Cathode

Comparing with other scandate cathodes, top layer scandate cathodes exhibited a longer life than pressed cathode and a better recovery capability after ion bombardment than the impregnated cathode [66].

Top layer scandate cathode comprises a porous pure tungsten pellet impregnated by barium-calcium-aluminates which is then coated with a scandium containing compound by sputtering or some other deposition technique. Thickness of the top layer ranges 100nm to 100μm. The scandium containing coating is various in term of chemical composition. In

the references [53,66–68] W+ScH_2 or W+Sc_2O_3 or W+$Sc_2W_3O_{12}$ were adopted to coating the impregnated tungsten pellets for producing the top layer scandate cathodes. While in the reference of [53] some other Sc-containing materials, W+Re_2Sc, $Re_{24}Sc_5$, were used as the coating. In addition the techniques for depositing the coating are various as well, two approaches-sputtering and the laser ablation deposition (LAD) are usually employed.

In the work of J. Hasker et al [60,69] it was suggested that generating a configuration of "Sc_2O_3 coverage on W" on the surface is critical for top layer scandate cathode as it aids to improve the emission homogeneity as well as ion-bombardment-resistance. Furthermore, it was claimed that, for top layer scandate cathodes, electron emission mainly generates from BaO globules on the W grains rather than Ba or Ba-O on bulk Sc_2O_3 [60].

Moreover, as aforementioned it was reported in the reference of [53] that a top layer (W/Re+Sc_2O_3) scandate cathode prepared by Laser Ablation Deposition (LAD) exhibited a greatly improved current density. More specifically the zero field emission which is defined as 10% deviation from space-charge law of this top layer scandate cathode could reach 400 A/cm^2 at 965 °C_b and 32 A/cm^2 at 760 °C_b [53].

2.5 Impregnated scandate cathodes

Impregnated scandate cathode (scandia doped tungsten impregnated cathode) has received a lot of research interests especially in the recent 2~3 decades owing to its high current density operating at a lower temperature and therefore a longer life time. The core part of an impregnated scandate cathode is a porous tungsten plug made from the powder metallurgy (P/M) which was subsequently impregnated by barium calcium aluminate. The impregnant material is various in composition, normally 411, 532 and 612 (mole ratio of

BaO, CaO and Al_2O_3) are frequently used. It should be noted all the scandate cathodes studied in this thesis are impregnated scandate cathodes which were prepared with using the impregnant of $6BaO\text{-}1CaO\text{-}2Al_2O_3$.

2.5.1 Fabrication of impregnated scandate cathodes

2.5.1.1 Liquid-solid (L-S) and liquid-liquid (L-L) doping techniques

In the fabrication process of impregnated scandate cathode, obtaining scandia doped tungsten precursor powder is the first step. Two techniques are usually employed which are liquid-solid (L-S) and liquid-liquid (L-L), respectively. As evidenced by literatures [9,70–72] by using these two doping methods, distribution uniformity of scandia has been improved significantly in comparison with the mechanical mixing. Moreover, the liquid-liquid technique is superior to liquid-solid method in terms of uniformity of scandia and emission performance as indicated by the references [73,74]. Since distribution of scandia is crucial to improve emission uniformity of impregnated scandate cathode, it is, therefore, of great important to elucidate preparation procedures and its theories of these two approaches as given in the following two paragraphs.

The L-S doping method is a single precipitation process. Scandia is first taken to from a scandium nitrate aqueous solution in which the tungsten oxide is subsequently added. After it dries the resultant scandia doped tungsten oxide is to be reduced in a hydrogen atmosphere and, eventually, the scandia doped tungsten powder is obtained [9,44,75,76]. As indicated by [4], the reduction process including two steps, firstly from $WO_{2.9}$ to WO_2 and then from WO_2 to W, as shown in Fig. 2.4. First, WO_2 nuclei formed in

the powder doped with aqueous solution of $Sc(NO_3)_3$ and then grew into large WO_2 crystals. Next, W seeds formed in WO_2 crystals during further reduction. And then the W vapor deposited on tungsten seeds would grow into large W crystals.

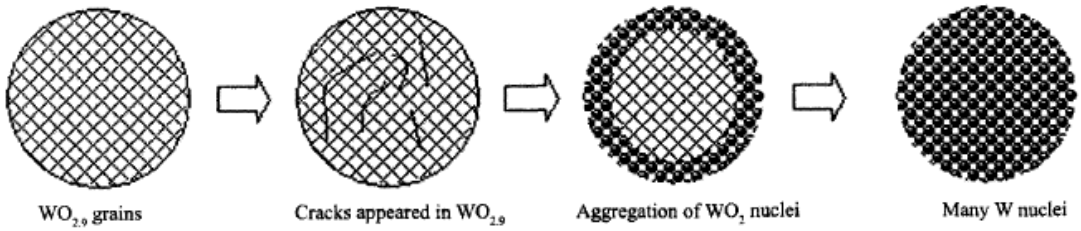

Figure 2.4 Reduction process from tungsten oxide to tungsten [4].

Unlike to the above described recipe for the L-S approach where tungsten oxide was used, it should be noted that L-S method adopted by Vancil applied metallic tungsten to replace the tungsten oxide [10,50]. As implied in the publication [10] the resultant L-S scandate cathode exhibited excellent emission capabilities including a low knee temperature and narrow transition range from space charge limited to temperature limited which means a more uniform electron emission.

In contrast to the L-S doping method, the L-L doping technique is essentially a co-precipitation process where both scandia and tungsten are precipitated from the solution during powder preparation. More specifically, scandium nitride and ammonium metatungstate are normally adopted as the starting materials which was first mixed in an aqueous solution to form a Sol and then converted to a Gel by baking. Then it is fired in air to remove organic impurities and followed by reduction in hydrogen atmosphere. Wang et al [9,70,73], carried out extensively research of impregnated scandate cathode developed with both L-S and L-L precursor powders. According to the relative investigation result, it has been demonstrated that emission properties of impregnated scandate cathode has been greatly enhance, moreover, L-L scandate cathode exhibited a better emission that the

counterparts. However one issue for L-L doping technique is that to some extent the particles size of the resultant powder is unpredictable as suggested by Vancil et al [10,77].

With regarding the distribution homogeneity of Sc_2O_3, it has been well recognized that L-L technique superiors to L-S method. One set of representative SEM micrographs showing Sc_2O_3 coverage on tungsten particles are presented in Fig. 2.5 [4] from which it can been seen that L-L powder (fig. 2.5 b) has a better homogeneously distributed Sc_2O_3 and a smaller particle sized comparing with the L-S powder (fig. 2.5 a).

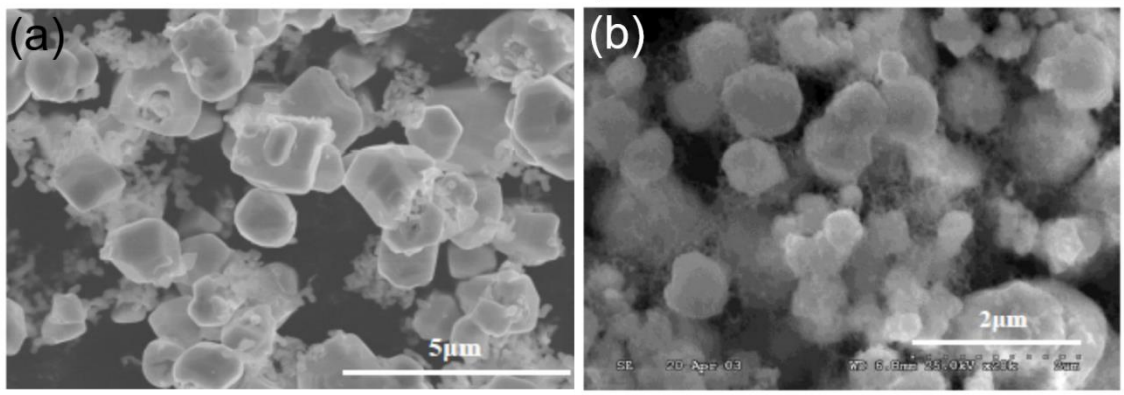

Figure 2.5 SEM images of scandia doped tungsten powders by L-S doping method (a), and by Sol-Gel doping technique (b) [4].

Most recently, Vancil [77] invented a two-stage-precipitation L-L technique. In the two-stage precipitation, the dissolved scandia solution and the dissolved tungsten solution are combined and placed in a warming oven. The initially precipitant appearing at the bottom of the container is called as the first precipitation. The first precipitant is then poured into another warm container to continue the evaporation, eventually we get the second precipitant. Both the 1st precipitant and the 2nd precipitant are fired in dry hydrogen atmosphere. As implied in [77], the oxygen concentration of 2nd precipitated powder is ~11% (a.t. %), which is much lower than that of the 1st precipitant (24-38 % in atomic

percent). This is a very promising improvement since we think a lower oxygen content is beneficial for the final performance of scandate cathodes.

2.5.1.2 Fabrication of scandate cathodes

With the obtained scandia doped tungsten precursor powder, it is usually being die-pressed (pressure varying from 140-1400 kPa) and sintered (a hydrogen atmosphere) to form a porous tungsten pellet first and followed by impregnation of barium calcium aluminate. During the impregnation process, molten barium calcium aluminates are closely contact with the tungsten pellet and then flow and diffuse into the pores. Upon the completion of impregnation, the cathode is then washed using deionized water for removing the surface residual impregnant. Prior to the emission testing in close spaced diode, impregnated scandate cathodes need to be activated under the temperature of approximately 1150 $°C_b$. It should be addressed that a lot of complex chemical reactions are presumably occurred during the impregnation process and activation period while these have not yet been fully understood.

It should be noted that the scandate cathodes studied in this work have been activated and some of them have been tested in CSD for several thousands of hours before the materials characterization. All the scandate cathodes were prepared by e beam where the emission testing performed.

2.5.2 Configuration of scandate cathodes

A schematic diagram of an impregnated scandate cathode is displayed in Fig. 2.6. The core component (body) of a scandate cathode is a porous tungsten pellet prepared through the P/M technique (component a in Fig. 2.6 a). The cylindrical tungsten pellet was

wrapped with a heater (coil-like) that raises temperature for electron emission (component b in Fig. 2.6 a). Both the tungsten plug and the heating material are held by a larger hallow cylinder made of molybdenum (component d in Fig. 2.6 a) and the inside space is occupied by a ceramic filler (component c in Fig. 2.6 a) . Two important functions of it are isolating the heating material and providing a conduction path to the tungsten insert. One of a real scandate cathode is also exhibited in Fig. 2.6 b.

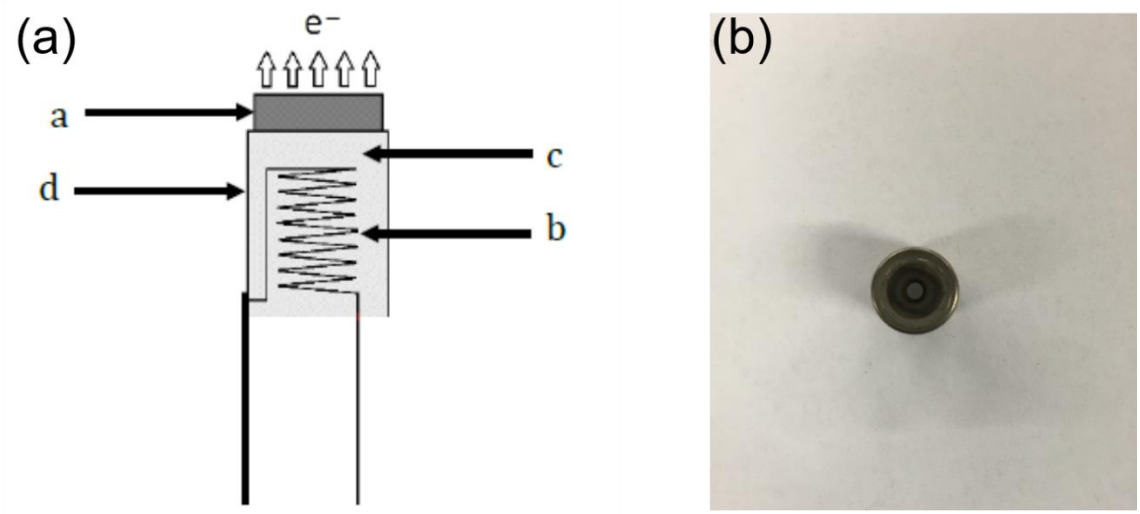

Figure 2.6 A schematic diagram of a dispenser cathode (a) [5], and an image of a real scandate cathode (b).

Figure 2.7 displays a cross section of the cathode body- tungsten matrix with impregnated by barium calcium aluminate- of a scandate cathode. As can be seen in Fig. 2.7 the impregnated oxides fill the pores among tungsten particles which enables the free Ba migrates (diffuses) from the body to the surface. Normally Ba is produced by the chemical reactions took place between the impregnated oxides and tungsten at the sites of pore walls, which is similar to the conventional B type cathodes. After Ba diffuses to cathode surface it will form a Ba-O dipole layer that can lower the work function from

original 4.6 eV (of tungsten) to approximately 2.1 eV (for B type cathodes). Note the work function of scandate cathode is 1.6-2 eV while the underlying reason remains unclear [8].

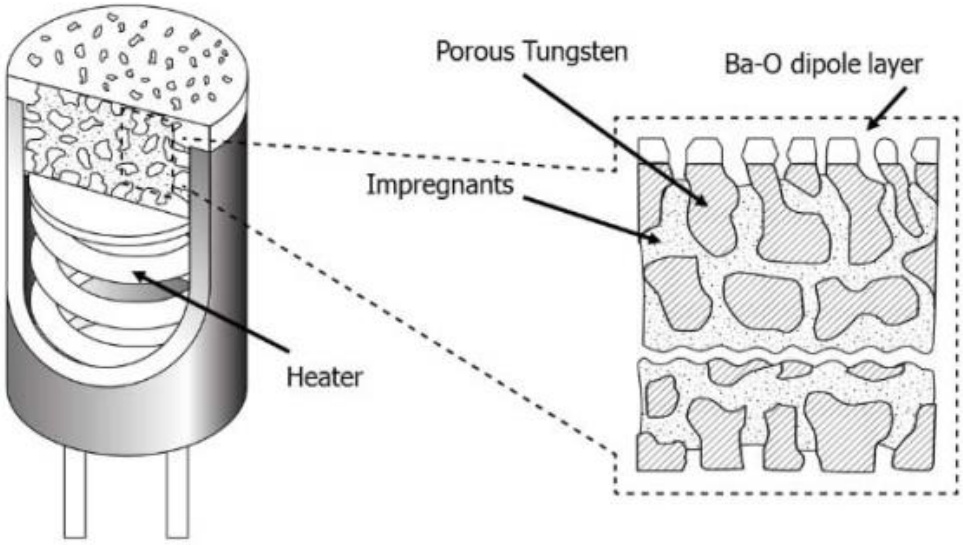

Figure 2.7 Typical Cross section of a scandate cathode [6].

2.6 Emission properties of scandate cathodes

According to the Richardson-Dash equation ($J=AT^2\exp(-\Phi/\kappa)$ where J is current density (A/cm^2), T is temperature (K), Φ is work function (eV), κ is Boltzmann constant, and A is the Richardson constant), current density is inversely related to work function of the emitting surface which means a lower work function is always desired for receiving a higher electron emission.

To evaluate emission performance of scandate cathodes, close spaced diode configuration is usually employed. In Wang et al [73], space charge limited current densities of over 30 A/cm^2 at 850 $°C_b$ has been routinely obtained. Moreover, an extremely long life time over 10000h under the condition of 950 $°C_b$ and 2 A/cm^2 has been achieved. More impressively, in Wang et al [44], a scandia doped impregnated cathode developed

with L-L precursor powder reached 52 A/cm^2 at 850 ℃$_b$. Wang and Liu et al [9,73,78] attribute the enhancement of emission capabilities of scandia doped impregnated cathode to a Ba-Sc-O multilayer of approximately 100 nm that covers tungsten grains. However, the emission model of the Ba-Sc-O thick layer (~100 nm) is still being suspected since no such surface layer was detected under transmission electron microscopy [79,80].

It is commonly accepted to the cathode community that scandia is added to cathode by doping it into tungsten powder for impregnated scandate cathodes. However, as studied in literature [81,82] scandia is added to the normal impregnant which is the barium calcium aluminate. In this "revised" impregnant as described therein the content of Sc_2O_3 is approximately 3% by weight percent. The cathode is manufactured by impregnating a porous tungsten matrix with a molten mixture which is a combination of Sc_2O_3 and the barium calcium aluminates. As a result, Sc_2O_3 is introduced to the cathode along with the normal impregnated material. Besides the difference in the composition of impregnant, the implementation of impregnation and activation processes of this kind of scandia doped impregnated cathode is similar to that of normal impregnated scandate cathodes. As indicated its current density could be reached to 5 A/cm^2 at 1000 ℃ and life is over 3000 hours [81].

2.7 Emission models for scandate cathodes

Unlike the B type cathodes where the Ba-O dipole is responsible for the lowered work function (from 4.6eV to 2.1eV) [2,31,32,83–88], nonetheless, the emission model of scandate cathodes has yet been fully understood. In the past decades, several models have been proposed for scandate cathodes, like the model of Ba-Sc-O monolayer [7,62,89], the

model of 100 nm Ba-Sc-O surface [9,24,73,78,90,91], and the semiconductor model [92] etc. Among them the models of Ba-Sc-O monolayer and 100nm-Ba-Sc-O surface layer are widely discussed and will reviewed in detailed in this section.

2.7.1 Model of Ba-Sc-O monolayer

The model of Ba-Sc-O monolayer was proposed and further verified by Sasaki [7,62] and Yamamoto [8,68] based on the research of scandate cathodes with a coating film that contains W-Sc_2O_3 or the compound of $Sc_2W_3O_{12}$. This model states that a Ba-Sc-O monolayer formed on cathode surface is responsible for the enhanced electron emission of scandate cathodes. A schematic diagram of the Ba-Sc-O model is displayed in Fig. 2.8 in which it was claimed that the monolayer sits on the top of the coated film [7].

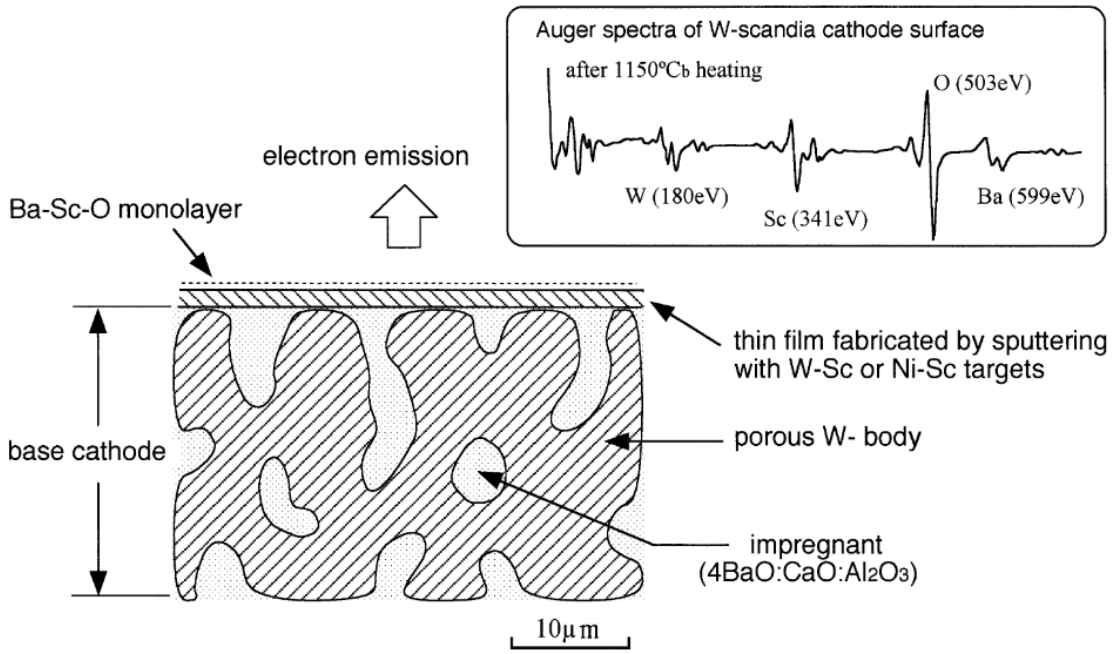

Figure 2.8 Schematic of the Ba-Sc-o monolayer model. The inset on upper-right corner shows a typical auger electron spectrum of the W-Sc_2O_3 containing film [7].

For the formation of the Ba-Sc-O monolayer, free Sc needs to be obtained first. Yamamoto et al demonstrate [8] that free Sc atoms are produced through the surface chemical reaction between the compounds of $Sc_2W_3O_{12}$ and Ba atoms supplied from cathode body to the surface.

$$Sc_2W_3O_{12} + 3Ba = 3BaWO_4 + 2Sc \qquad 2.2$$

In order make this chemical reaction possible Ba atoms need to diffuse from pores inside the tungsten matrix and reach the surface of the coated film. Then Ba atoms can react with the $Sc_2W_3O_{12}$ to generate metallic Sc. In addition, $Sc_2W_3O_{12}$ is also possible to be decomposed into Sc_2O_3 and WO_3 and the resultant WO_3 is possibly evaporated during the reaction. This change was validated by the auger electron spectroscopy analysis, as presented in Figure 2.9.

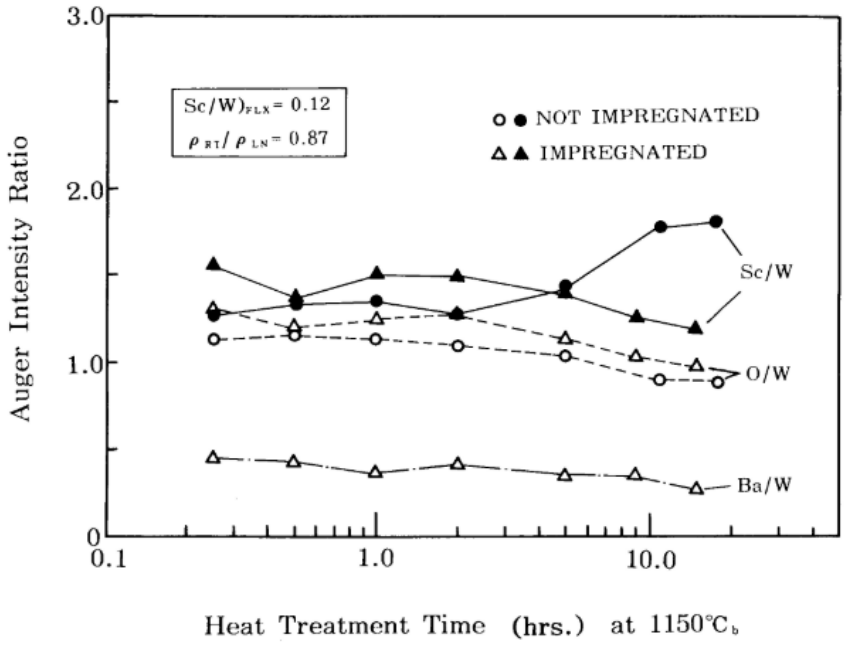

Figure 2.9 Change in surface atom concentration as a result of heat-treatment at 1150 $^{\circ}C_b$ evaluated by Auger electron spectroscopy. Auger intensity ration with respect to W is measured for a (W- $Sc_2W_3O_{12}$) coated cathode (impregnated) and a nonimpregnated cathode sample (not impregnated) [8].

As suggested by Muller [93] and Wang [20] a monolayer of Ba-Sc-O on W (100) can produce the lowest work function of 1.5-1.7 eV which is in agreement with Jacob's work [94]. Sasiki et al [7] indicated that it cannot produce a high electron emission if the surface layer contains too much scandia since the Ba-Sc-O monolayer on the scandia area may not generate a low work function. In another words it is the materials system of Ba-Sc-O monolayer on tungsten surface that can produce a low work function and therefore enhance the emission capabilities of scandate cathodes. Moreover the content of Sc_2O_3 the in the coating film as well as its thickness influence the final emission level of the scandate cathodes as illustrated by Fig. 2.10 [7].

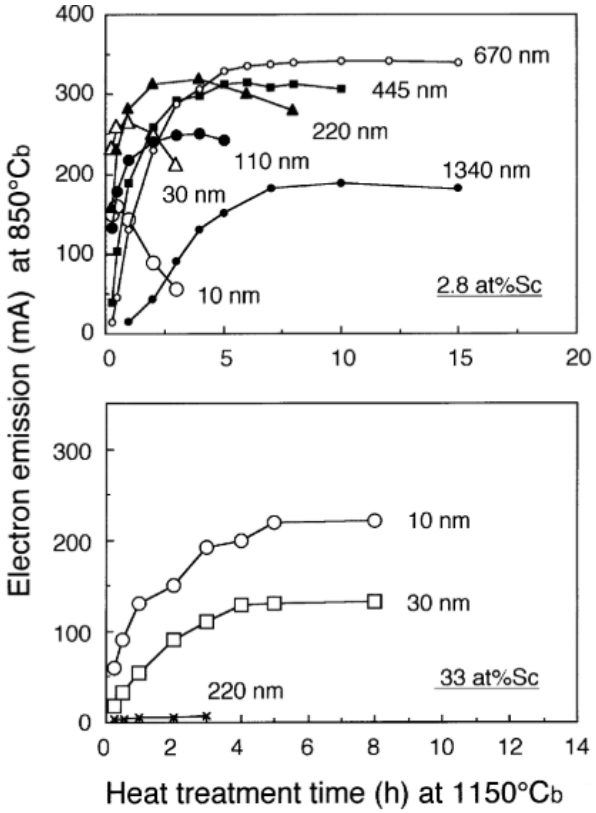

Figure 2.10 Change in electron emission of W-scandia cathodes by activation heating at 1150 ˚C_b. The cathode diameter is 1.23 mm and the distance of a cathode and an anode is 7mm [7].

2.7.2 Model of 100 nm Ba-Sc-O surface layer

The model of 100 nm Ba-Sc-O was evolved on the basis of the "semiconductor model" which was first proposed by Raju and Maloney [95]. The semiconductor model for scandate cathodes was looked as an extension from oxide cathodes [96]. According to Raju and Maloney [95] the thickness of the surface layer has to be 400-500 nm in order for the semiconductor model to be applicable. Later Wang's group proposed that it is a 100nm Ba-Sc-O surface layer that being responsible for the emission enhancement for scandate cathodes [4,9,24,41,75,97,98]. They conducted a mass of experiments on impregnated scandate cathodes and then derived this conclusion.

In this model it was claimed the ionic Sc produced by scandium oxide reacting with the impregnant and tungsten co-diffuses with Ba and O to the cathode surface and then forms the Ba-Sc-O surface layer after the activation process of scandate cathode. The thickness of the Ba-Sc-O surface layer was determined by the depth profile analysis using the auger electron spectroscopy, as indicated by the Fig. 2.11 [9]. In Fig. 2.11 the AES results showed that the content of all of Ba, Sc and O elements altered until to the depth of approximately 100 nm.

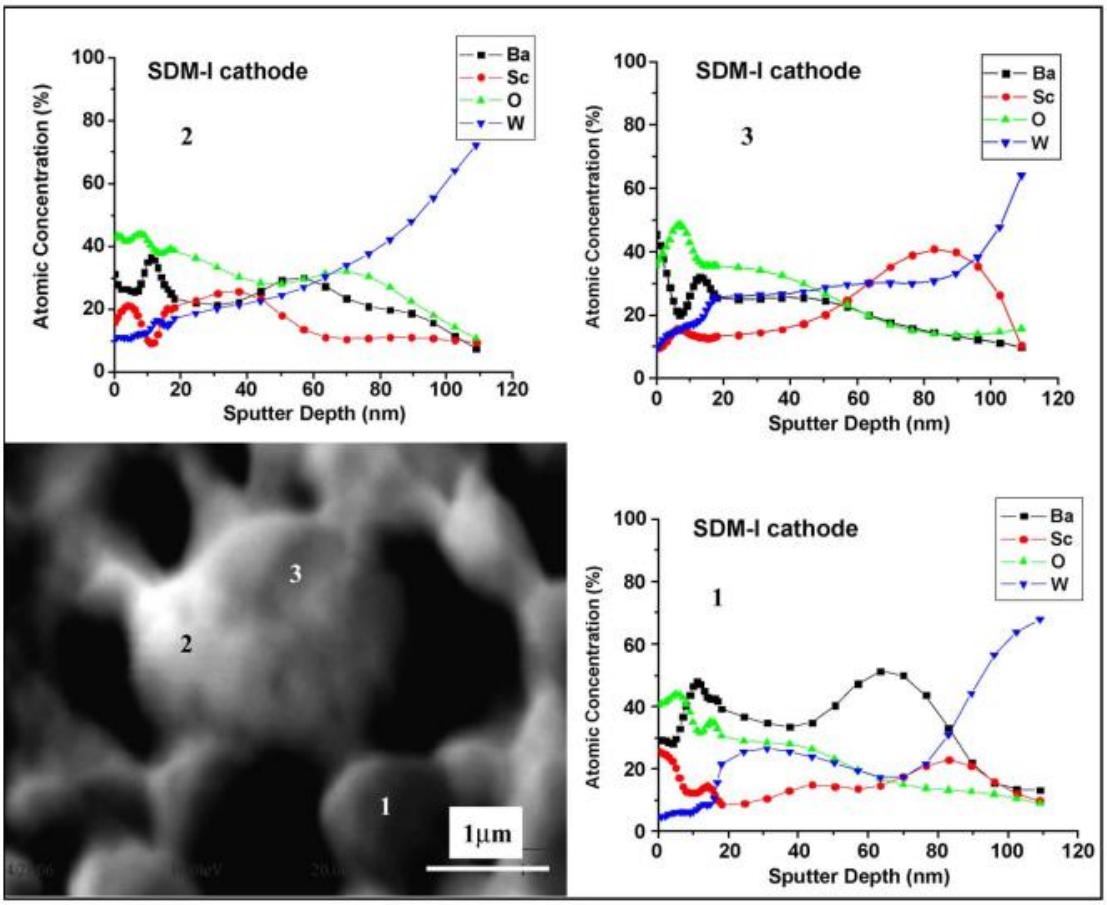

Figure 2.11 Surface elemental depth profiles of a scandate cathode developed by Wang's group [9].

Substantial work has been done by Wang's group to clarify the formation mechanism of the 100 nm Ba-Sc-O surface layer for scandate cathodes. One essential problem is that scandia must be reduced to be metallic (ionic) Sc otherwise it cannot migrate from the inside to the surface of a scandate cathode as the diffusion coefficient of scandia is too small to fulfill it [78]. Moreover the mechanism of producing free Sc in the cathode materials system remains unknown. The only chemical reactions generating free Sc that can be found in literatures is the equation 2 in which the compound of $Sc_2W_3O_{12}$ was involved, however, to author's knowledge this compound has never been found in

impregnated cathodes without a coating (like the coating of W-Sc_2O_3 or $Sc_2W_3O_{12}$ as studied by Sasaki [62]and Yamamoto [8,99,100]).

It is interesting to note that the migration of free Sc from the cathode body to its surface occurred simultaneously with the diffusion of Ba and O elements during the activation process (at the temperature of 1150 ˚C_b) of scandate cathodes, as suggested by Fig. 2.12 (a) [9]. In addition, the variation tendency of Ba and Sc elements on cathode's surface is similar as implied by Fig. 2.12 (b) [9]. Furthermore atomic concentration ratios of Ba:Sc:O is about (1.5-2):1:(2-3), as claimed by Wang [9,24].

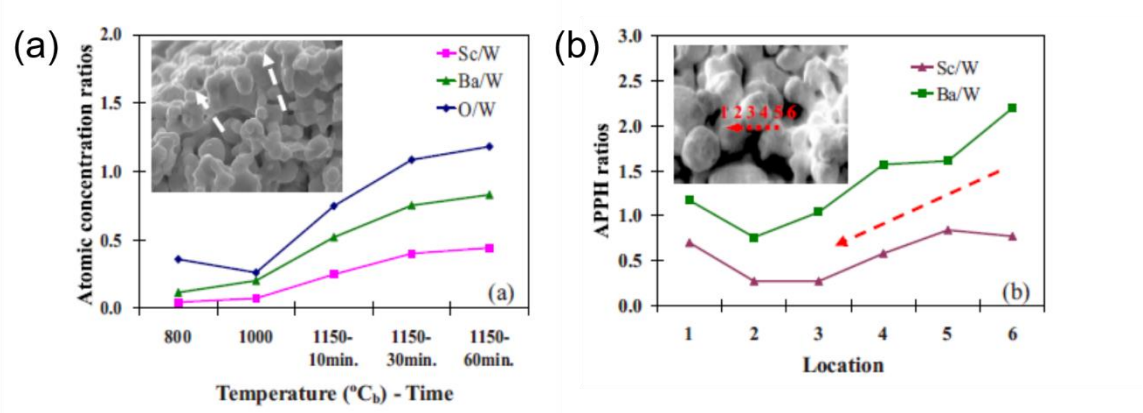

Figure 2.12 Diffusion of Sc, Ba and O during activation and surface migration of Ba, Sc along the surface. (a) Changes of AES atomic concentration ratios of Sc/W, Ba/W and O/W during activation. (b) Variation of Auger peak-to-peak height (APPH) ratios of Ba/W and Sc/W from pore to W grain [9].

However it should be noted that our recent research [14,50,101] does not support this model since no Ba-Sc-O surface layer on the order of 10-100 nm was discovered on scandate cathodes surfaces.

2.8 Unsolved issues for scandate cathodes

It should be recognized that scandate cathodes have yet been widely used and still have a long way to go before realizing a large-scale commercial production as there are

several issues have yet been solved which greatly limit their implementation. Currently the scandate cathodes are strongly needed to meet the requirements of VEDs. As described in the reference of [9], the ideal thermionic cathodes for VEDs should have: high space-charge-limited current densities in both pulsed and DC modes; excellent emission uniformity; a long lifetime and a reasonable operating temperature; a low evaporation rate of barium; reproducibility in fabrication and manufacturing.

To realize the application of scandate cathodes, several issues should be well resolved which include: indistinct emission model; inhomogeneous electron emission; unknown life; nature of the emission surface; vulnerability to arcs and ion backstreaming; lack of repeatability and etc.

In this work, attempts are made to study nanostructures, materials evolution and surface morphologies and the emission properties of scandate cathodes. We aim at building a relation between the materials features (surface phases, morphology and microstructure of cathode matrix) and the emission properties of scandate cathodes.

CHAPTER 3. MATERIALS AND METHODES

3.1 Fabrication of precursor powder and scandate cathodes

3.1.1 Preparation of liquid-solid (L-S) powder

In this study two types of scandate cathodes were characterized from the perspectives of emission evaluation and microstructures. One is the L-S scandate cathode which corresponds to scandate cathode prepared with liquid-solid (L-S) precursor powder.

The L-S precursor powder denotes the scandia doped tungsten powder was prepared using the liquid-solid approach which is a single precipitation process. Scandia (Sc_2O_3) first forms an aqueous nitrate solution, and then metallic tungsten (around 1μm in size) powder is added to that solution. During the precipitation process the scandium oxide particles attach to the tungsten particles rather than to themselves.

It should be noted that the distribution of scandia in the resultant scandia doped tungsten powder is decent but not as good as using the liquid-liquid method (which will be discussed in the next section) as indicated by Vancil et al where they found some scandia formed clumps with little attachment to the tungsten or some tungsten particles were not covered with sufficient scandia as the Fig. 3.1 shown below [10].

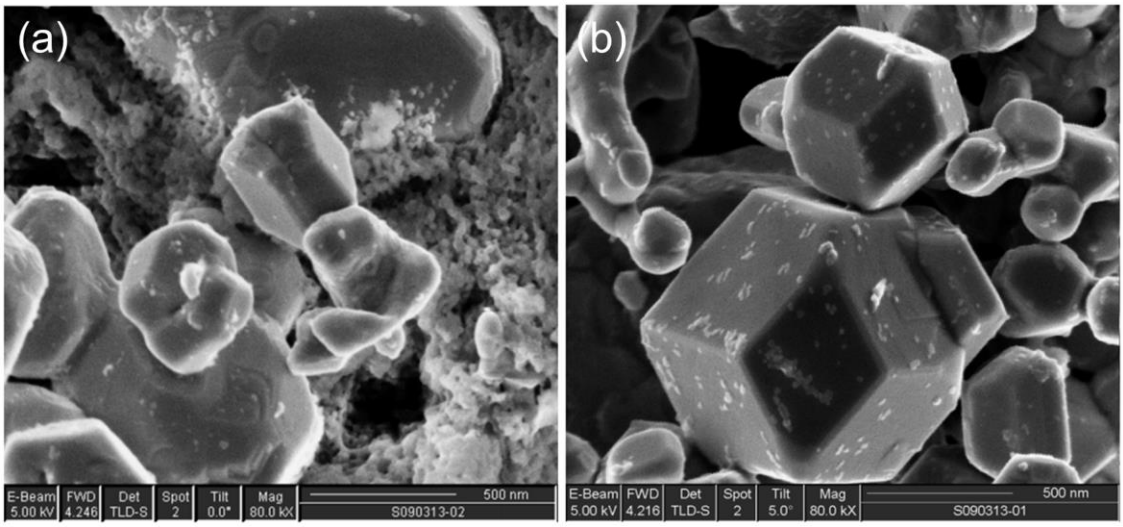

Figure 3.1 L-S precursor powder in which Sc_2O_3 fails to adhere well, forms Sc_2O_3 clumps (a) and tungsten particles with insufficient Sc_2O_3 (b) [10].

3.1.2 Preparation of liquid-liquid (L-L) powder

As an improvement, liquid-liquid (L-L) powder has a better uniformly distributed scandia in comparison with the L-S technology. In this process, we use the scandium nitride and ammonium metatungstate as the staring materials and get them mixed in aqueous solutions to form Sol and then transfer into Gel by baking. Then resultant product is calcined in air to remove the organics, e.g., C and N, and followed reduction in hydrogen atmosphere to get the scandia doped tungsten powder.

Since the raw materials are mixed in their aqueous solutions, therefore, the admixture is much more uniform. As indicated by Vancil et al the tungsten particle size made by the L-L approach is difficult to predict or control.

3.1.3 Scandate cathodes fabrication

The scandate cathodes studied in this work were fabricated by e beam inc., our collaborator in this project. Starting with the scandia doped tungsten powder, L-S powder

or L-L powder, it was die-pressed and sintered to make a porous tungsten pellet which serves as the matrix of the final scandate cathode. The tungsten pellet is usually with density at ~60% of the theoretical density of tungsten plus scandia. The tungsten pellet is then impregnated with barium calcium aluminate which is known as the impregnant materials. The mole ratio of $BaO\text{-}CaO\text{-}Al_2O_3$ is various and what we adopted is 6:1:2. Upon the completion of impregnation process excess impregnant materials was removed by washing with deionized water. After that the cathodes were activated and tested before the microstructural characterization.

3.2 Materials Characterization

3.2.1 SEM

Scanning electron microscopy (SEM) is probably the most extensively used facility for materials research with which morphological features of various samples ranging from metals, alloys to bio-samples can be studied. SEM utilizes a high energy electron beam to generate various signals including secondary electrons, backscattered electrons and characteristic X-rays on the surface of the source specimens.

Secondary electrons and backscattered electrons are commonly used for imaging samples. More specifically, secondary electrons are valuable for showing the morphology of materials while backscattered electrons are basically used for presenting elemental contrast of the samples. In addition the characteristic X-ray are produced for each element in the materials that is “excited” by the electron beam which is used for composition measurements with using the EDS detector.

In this work, all the scandate cathode samples or powder samples were analyzed using the FIB-SEM (Helios nanolab 660). For imaging most of the work was done under the immersion mode for acquiring a higher resolution.

3.2.2 EDS

Energy dispersive X-ray spectroscopy, could be called EDS, EDX, EDXS or XEDS, is an analytical technique for elemental analysis and composition measurements. The working theory is based on the fundamental principle that each element has a unique atomic structure allowing a unique set of peaks on its electromagnetic emission spectrum.

Usually three modes including point analysis, line scanning and mapping can be conducted with EDS for elemental and compositional analysis. The accuracy of the quantitatively composition measurements is affected by multiple factors, i.e., many elements have overlapped X-ray emission peaks which increase the inaccuracy for quantitative analysis. Another significant factor reducing the composition measurement precision is that the X-ray are emitted in all directions and not all of them can escape from the source sample. As a result, the accuracy is lowered for quantitative measurements.

In this work, EDS is widely utilized for elemental distribution analysis and composition quantitative measurements. For points analysis, at least 5 points were measured for getting the average composition. For line scanning and mapping, both true distribution and quantified distribution can be derived using the same source acquirement.

3.2.3 EBSD and TKD

EBSD, electron backscatter diffraction, has been a relatively matured characterization technology for materials research which allows crystallographic information to be obtained from a small volume of materials. EBSD detector is usually attached to a scanning electron microscopy (SEM) or FIB-SEM as what we utilized in this work. The technique of BSD provides versatility in mapping crystal orientation and studying textures in materials. EBSD maps are generated by moving a focused electron beam point by point across a grid of positions on the surface of samples as the schematic diagram for the EBSD observation shown in Fig. 3.2 [11]. At each point, some of the electron backscattered from the sample are collected by the detector to form an electron backscatter diffraction pattern.

The EBSD experiments in this work were performed using the FIB-SEM equipped with an Oxford EBSD detector. During the analysis, the cathode sample was put on a pre-tilted sample holder (tilted for 72°) without any process on the cathode surface in order to avoid any damage occurred to the sample.

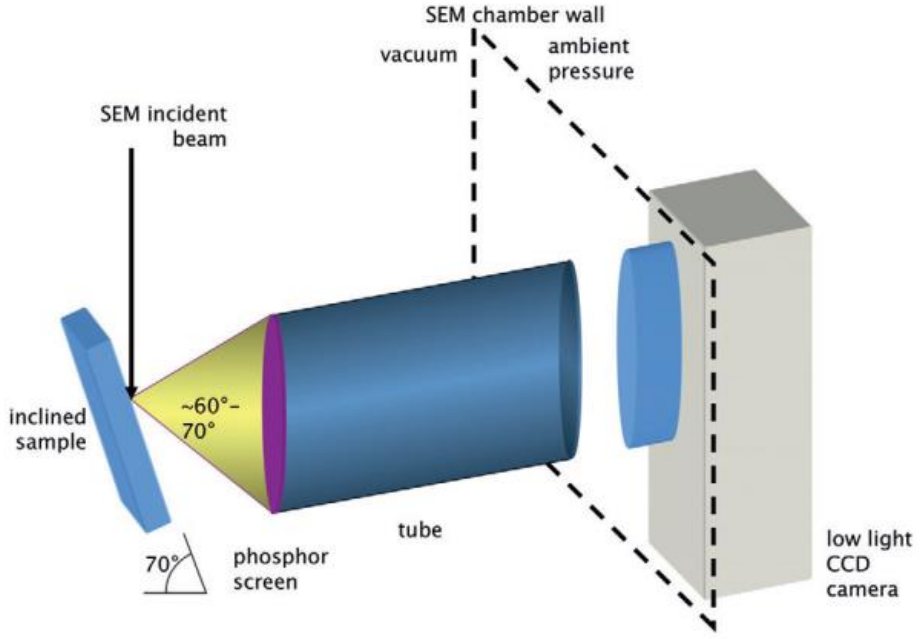

Figure 3.2 Schematic diagram for EBSD observation [11]

Transmission Kikuchi diffraction (TKD), also known as transmission electron backscatter diffraction (t-EBSD) has gained significant interest for the characterization of nanocrystalline materials and nanostructures. For the normal EBSD, the spatial resolution is approximately 20-50 nm for dense to light materials, and which becomes worse at the bottom for the tilted sample during the experiments. However the TKD has a significantly improved spatial resolution as the sample is electron transparent and mounted horizontally. As a result, the diffraction pattern originates from the bottom of the sample and a smaller volume of volume. As measured by Trimby [102], the measured resolution is as small as 2 nm. The experimental configuration for TKD analysis is presented in Fig. 3.3.

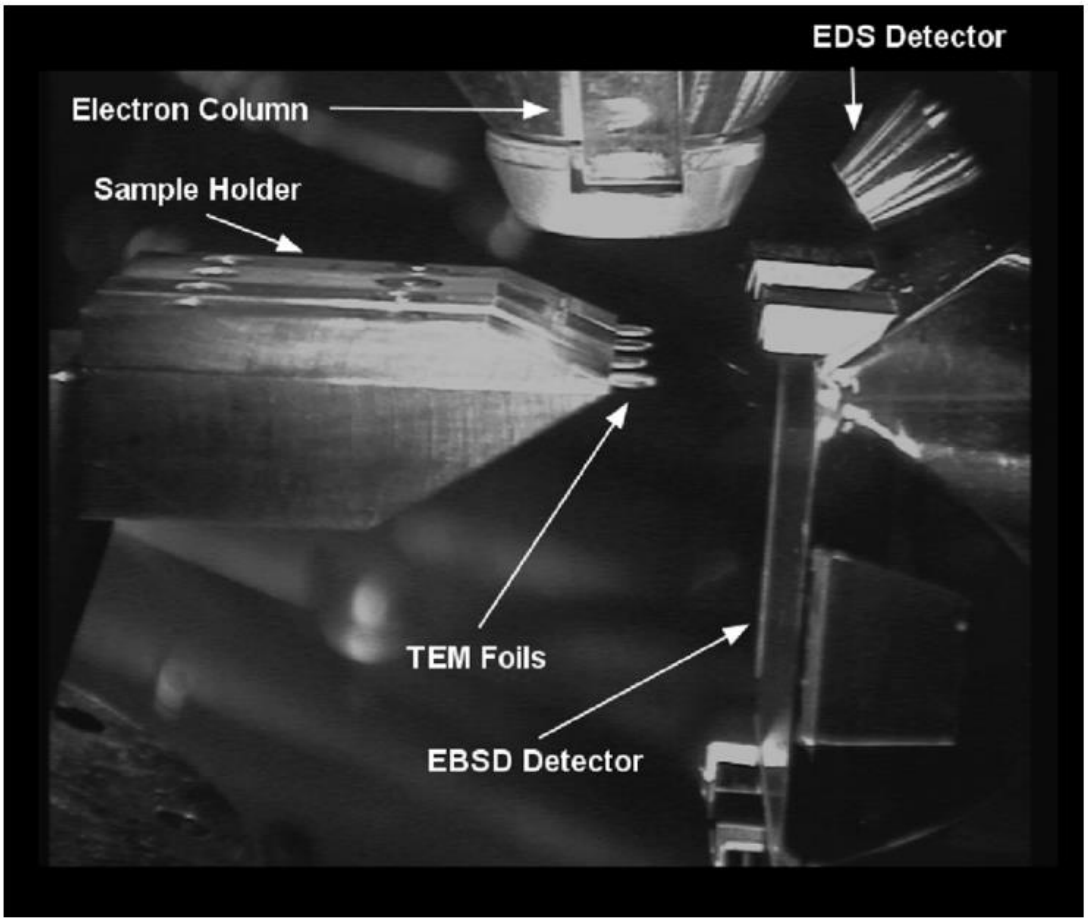

Figure 3.3. Set-up configuration of TKD in a SEM chamber [12].

3.2.4 XRD

X-ray diffraction (XRD) is analytical technique primarily used for phase identification of crystalline materials. The testing samples could bulk or powder for the XRD running. The principle of XRD is based on the Bragg's Law as presented by the equation 3.1

$$n\lambda = 2d \sin\theta \qquad 3.1$$

Here d is the spacing between diffracting planes, θ is the incident angle, n is any integer, and λ is the wavelength of the beam. This law correlates the wavelength of

electromagnetic radiation (normally it is Cu K_α) to the diffraction angle and therefore to the lattice spacing of a crystalline sample.

For the XRD analysis on scandate cathodes samples, the 2θ was set as 5-80° and the scan speed is 1°/min. All the XRD tests were carried out using the Bruker-AXS D8 DISCOVER Diffractometer. We usually did a Z-scan to find the right height of the sample prior to the locked coupled scan.

3.2.5 XPS

X-ray photoelectron spectroscopy (XPS) is an important surface characterization technique which analyzes the average surface chemistry of a sample up to a depth of approximately 10nm [31,50]. This technique enables one to study atomic concentrations and chemical states (like the valence states) of elements present at the sample surface. XPS has a very high elemental composition sensitivity which is up to 0.1%. In addition XPS can be used to analyze not only conductive samples also non-conductive specimens.

XPS uses a soft X-ray source (i.e., Al Kα) in vacuum as the source beam. Photoelectrons can be emitted form the core levels when X-ray photons hit and transfer energy to core-level electrons. In addition, the kinetic energy of emitted photoelectron depends on the incident X-ray and binding energy of the atomic orbital from which it originated. The energy and intensity of the emitted photoelectrons are then analyzed to determine the atomic concentration and identify the chemical state of elements appear on the sample surface.

In this work, all the XPS tests on scandate cathodes were conducted using the Thermo Scientific K-Alpha facility. It is noted that the C 1s peak at the binding energy of 284.6eV

was used for correcting the charge shift during deconvoluting peaks of high-resolution spectra and generating the quantified atomic concentrations.

3.2.6 TEM lamella preparation

TEM samples were prepared using the Dual-beam Focused Ion Beam (FIB, Helios nanolab 660). The procedures for making a TEM lamella can be divided to three main processes- lamella lift out, reattaching and thinning. Figure 3.4 displays the recipe for the TEM sample preparation using the FIB step by step.

First we deposit a protective layer, i.e., Pt, on the area of interest which is approximately 500 nm in thickness using the electron beam. After that a thicker protective layer (~1µm) is rapidly deposited under the ion beam as the Fig. 3.4 (a) showed. Next ion beam is used to remove the materials upper and below than the selected area as indicated by Fig. 3.4 (b) which is followed by a so called "J-cut" to cut through the stem of the lamella as presented in Fig. 3.4 (c). Afterwards we insert the needle and weld it to one corner of the lamella (see Fig. 3.4 d) and then cut the other side quickly to release the lamella and make it ready to be lift out with attaching to the needle.

The next step is reattaching. We first insert the needle to the edge of the copper grid where the lamella is to be welded, as seen in Fig. 3.4 e, and then welding the lamella to it by depositing some welding Pt (Fig. 3.4 f). Then using the ion beam to mill the connecting area between the needle and the lamella.

The final process for the sample preparation is thinning it to a electron transparent thickness. We start the thinking process with a tilting angle of 53.2 to make sure the lamella was thinned gradually from the bottom area as presented in Fig. 3.4 (g). We could use a relative larger voltage and beam current, i.e., 30kV and 0.4nA, to expediate the thinning

process till the thickness is approximately several hundreds of nanometers (see Fig. 3.4 g). Then it is advised to use a lower voltage and beam current, for instance 15 kV and 80pA, to reduce the milling rate in case the lamella crashes. At the final period of thinning it is suggested that we could use a very small voltage and current, i.e., 5kv and 30pA, to smooth both sides of the lamella before it is transferred to TEM chamber for examination, as exhibited in Fig. 3.4 (h).

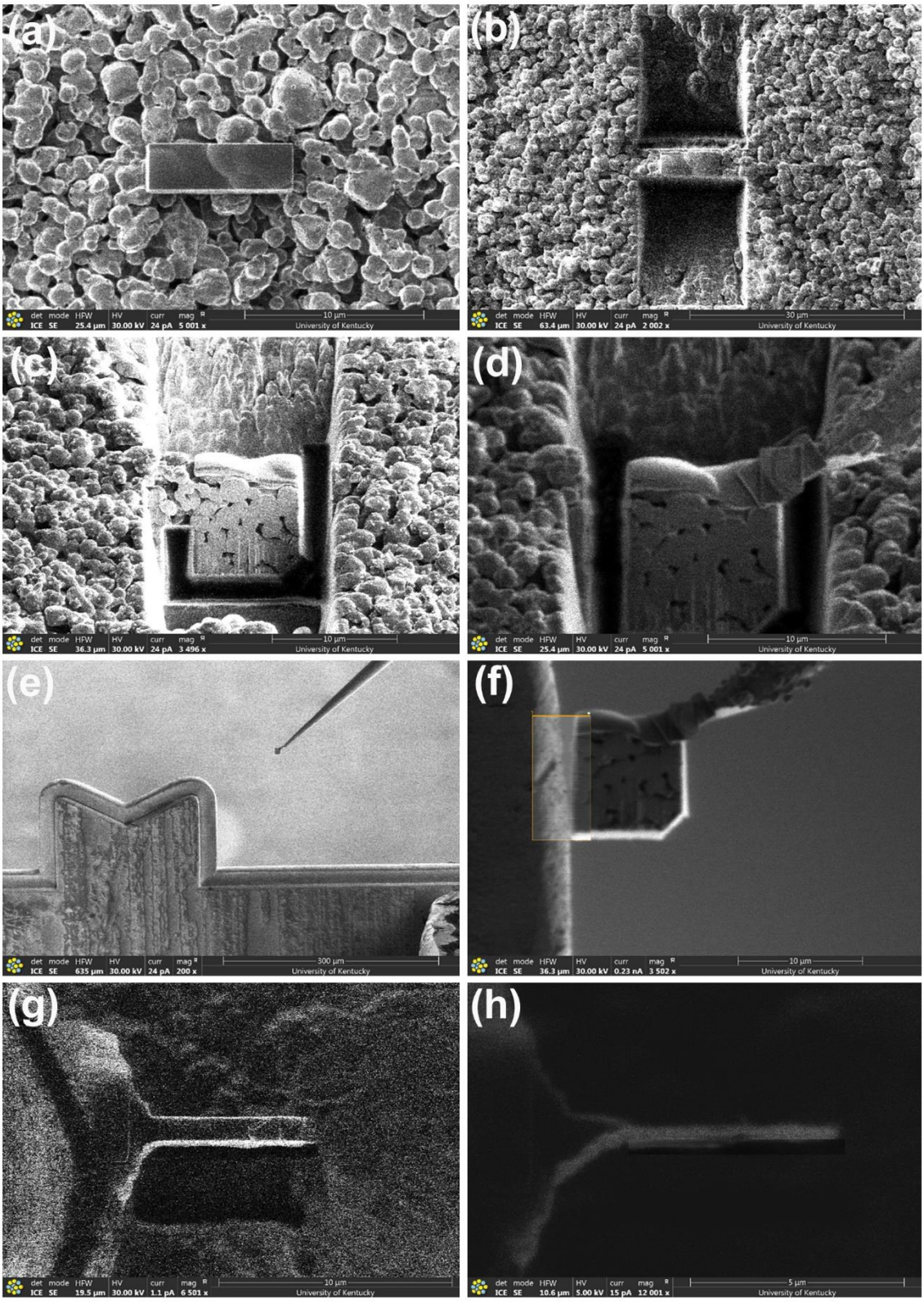

Figure 3.4 Procedures of TEM sample preparation using a FIB.

3.2.7 (S)TEM

Transmission electron microscopy (TEM) is a comprehensive characterization technique which has an extraordinary capability to study crystal structure, phase identification, elemental analysis of materials down to atomic levels. TEM can be used to imaging, generate diffraction pattern and work under the scanning transmission electron microscopy (STEM) mode.

TEM imaging normally includes the bright field (BF), the dark field (DF) modes and the high resolution TEM (HRTEM). For the BF mode, an aperture is placed in the back focal plane of the objective lens which allows only the direct beam to pass. In this case mass-thickness contrast and diffraction contrast contribute to the image formation, implying that thick areas or areas in which heavy atoms are enriched or crystalline areas are to generate a dark contrast. In the DF imaging mode, the direct beam is blocked by the aperture. Instead one or more diffracted beams are allowed to pass the objective aperture. A lot of useful information is presented considering that the diffracted beams strongly interact with the sample. Therefore the DF mode is apt to observe the micro defect in materials, e.g., dislocations, stacking faults etc. HRTEM is known as the lattice imaging. To obtain lattice images, a large objective aperture is selected which allows many beams including the direct beam and diffracted beams to pass. The image is formed by the interference of the diffracted beams with the direct beam which is also called as the phase contrast.

Selected area electron diffraction (SAED or SAD) is another crucial function of TEM which can be applied for crystal structure study for materials. In SAED, an aperture is typically located in the first image plane below the sample which is used to define the area

from which the diffraction pattern is to be recorded from the source sample. SAED diffraction pattern can provide evidence for identifying crystalline materials (single crystalline or polycrystalline materials) or amorphous materials.

Scanning transmission electron microscopy (STEM) mode is also frequently utilized for TEM observation. In STEM, a highly focused electron probe is scanned across the sample and various signal can be collected for analysis. The transmitted electrons at a high scattering angle can form high resolution images, reveling the atomic number contrast (Z contrast) of the materials. The X-ray generated can be collect using an EDS detector for composition measurements. Electron's energy loss can be detected to analyze the compositional and electronic properties of materials which is known as the technique of electron energy loss spectroscopy (EELS).

In this study, three TEM facilities, JEOL 2010F, Thermo fisher (FEI) Talos F200X and JEOL JEM-F200, were used to carry out the investigations. The results are primarily presented in chapters 4, 5 and 6.

3.2.8 3D reconstruction

3D reconstruction is performed using the FIB-SEM for reveling the internal nanoparticles inside the tungsten gains constituting the body of scandate cathodes. One significant advantage of the technique of 3D reconstruction over 2D characterization is illustrating the geometry of nanoparticles or precipitations in 3 dimensional which provides a more accurate result in both qualitative and quantitative manners.

In this work, we use the FIB to reconstruct a tungsten grain with the size of around 500 nm and with the shape of near-sphere to unveil the internal nanosized Sc/Sc_2O_3

particles. Details of performing the experiment and the corresponding results are presented in chapter 5.

3.2.9 Emission testing

The electron emission properties were tested and evaluated at the e beam inc., where the scandate cathodes were produced. Four diodes were installed in one glass envelope which was subsequently pumped and baked at 400º C for four days. At the end of this period, the tubes are pinched off and the barium getters flashed. The test temperature was 50ºC above the knee, and the cathodes were pulsed at approx. 5% duty.

It should be noted that the diode testers employ a guard aperture which closely fits around the cathode, as seen in Fig. 3.5. This guarantees that the field reaching the cathode is uniform across the cathode. It is our understanding that workers at BJUT did not employ a guard in their diode tests. Consequently, the field was non-uniform and this may have contributed to the rounded activity knees reported by them. Also, emission from the sides of the cathodes is possible, which raises the detected emission above that coming from the flat surface of the cathode. This would account for some of the discrepancy between their knee temperatures and ours.

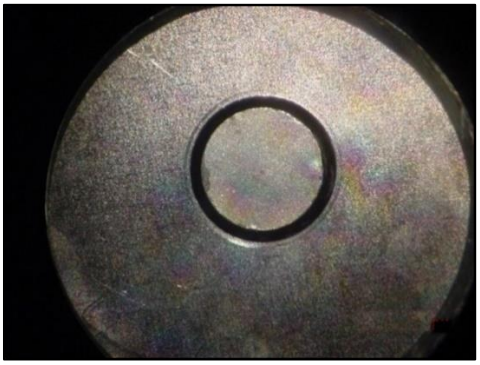

Figure 3.5 Cathode with a guard ring.

In addition, to record the brightness temperature during the tests we normally view the top surface of the cathode, which is tungsten, but very rough tungsten at that. It is noted that tungsten brightness temperature is about 30-40º C higher than the molybdenum brightness temperature when the true temperature is approximately 1100º C, e.g., 1020º C_b(Mo) and 1057º C_b(W) are corresponding to 1100º C (true).

3.2.10 Wulff analysis on crystal shapes

Surface morphologies of tungsten particles constituting the body of scandate cathodes were studied using the Wulff analysis. The software of Wulff maker was used to generate the equilibrium tungsten crystal shape with preset crystal planed and given surface energies. The detailed theory for Wulff construction can be found in the reference of [103].

CHAPTER 4. SCANDATE CATHODE SURFACE CHARACTERIZATION: EMISSION TESTING, ELEMENTAL ANALYSIS AND MORPHOLOGICAL EVALUATION

4.1 Introduction

Substantial and growing research interest in scandate cathodes (where scandium oxide is added to the tungsten pellet in the cathode) can be traced to the late 1970's [55], due to reports of significantly higher emission current density at lower working temperatures, as compared with conventional dispenser cathodes [6,24,51,63,73,74] . The superior properties of scandate cathodes would facilitate the generation of electron beams that better meet the requirements of high-power vacuum electron devices (VEDs), including traveling wave tubes and high-power microwave devices that are extensively applied in military, civilian and medical systems. However, there are several issues with scandate cathodes, including: non-uniform electron emission, low reproducibility, and uncertainty as to how scandium influences the emission mechanism [10,18,24,104–106]. As a result, scandate cathodes have not been widely utilized as dispenser cathodes in actual devices.

Despite having a long history of research and development, as well as several different models that were proposed to explain the emission behavior of scandate cathodes, there is still not a consensus view that accurately and succinctly describes this behavior. Through careful study [58,70,73,74,77,104,105,107], researchers have found that uneven electron emission from scandate cathodes could be attributed to the non-uniformity of scandium or scandium oxide (scandia) at the surface. Specifically, the adoption of doping methods for fabricating the starting powders, e.g., liquid-liquid (L-L) and liquid-solid (L-S) procedures, has helped improve the scandium or scandia distribution at the cathode surface, and has increased electron emission current density. The uniformity of electron

emission resulting from new doping procedures stands in stark contrast to results from previous doping techniques, e.g., where mechanical mixing was used. Reproducibility in the manufacturing of well emitting scandate cathodes is still an obstacle to implementation of such cathodes [70,75], and this is likely because the specific factors that lead to an overall lowered work function have yet to be understood at a fundamental level.

Emission current density from scandate cathodes far exceeds that of B-type cathodes, and this is largely attributed to the presence of scandia [9,28,73,104,108]. However, the role that scandia plays in enhancing electron emission has not yet been elucidated. Possible roles for scandia include regulation of surface oxygen concentration [60] or stabilization of a well-defined oxide structure that has a low work function [109]. Also, for scandate cathodes, it is known that tungsten is essential for the electron emission process, but it is unclear to what extent the structure, surface morphology and composition of tungsten grains influence the overall lowered work function and improved emission behavior. Several models have been proposed over the years to explain the enhanced emission behavior of scandate cathodes including the Ba-Sc-O monolayer model [8,62], the semiconductor model [92,93] and the thermal-field mechanism [110]. Apart from them, Wang et al. [9,24,63,73,78] claim that a semiconductor layer consisting of a Ba-Sc-O film, with thickness of ~100 nm, is responsible for the enhanced electron emission from scandate cathodes. This model was first introduced by Raju and Maloney [95], and was supported by Gartner et al. [108]. More recently, an article published by Lai et al. suggested that the thickness of the surface layer was 1-2 nm [42]. In order to develop new or improved models, it would help to more fully understand the material(s), including composition as well as phase, that are present in functional scandate cathodes.

This paper presents the results of a systematic investigation of multiple scandate cathodes that exhibited good emission characteristics (e.g. low knee temperature and nearly flat curve in the space-charge limited regime) during close-spaced diode testing, along with characterization of surface morphology and composition using multiple complementary techniques. Experimentally, several interesting features were observed at and near the cathode surfaces, and these were found to be characteristic of the scandate cathodes that performed well in this study. Noteworthy and distinctive features – facets and ledges – are discussed in detail. In addition, we combine theory with experiment to verify the equilibrium shape of tungsten particles using Wulff construction [103]. Moreover, barium/barium oxide particles appear to have formed on the surface of tungsten grains, which is consistent with calculations of metallic barium fully covering the available tungsten surface area at cathode operating temperature. The work reported here involved characterization of surface structure and composition to facilitate a deeper understanding of the materials that enable the emission behavior of scandate cathodes.

4.2 Material and Methods

The scandate cathodes tested and characterized in this study were fabricated by e beam, inc. All cathodes were fabricated with scandia-doped tungsten powder, which had been prepared using the L-S method, as reported previously by one of the authors [10]. This doping approach involved the addition of scandia (Sc_2O_3) to an aqueous nitrate solution, followed by the addition of metallic tungsten (W) powder to that solution. This yielded scandia-doped W powder, where nanoscale Sc_2O_3 particles were distributed over the surfaces of micron-scale W particles and, in certain cases, inside polycrystalline W

agglomerates. Afterwards, doped W powder for each cathode was pressed and sintered into a porous W pellet, 2 mm in diameter and 1 mm in thickness. The W pellet was then impregnated with a 6:1:2 barium-calcium-aluminate ($6BaO\text{-}1CaO\text{-}2Al_2O_3$), followed by washing with deionized water to remove residual impregnant from the cathode surface. Three pellets were fabricated at separate times (i.e., not batch processed) and were each incorporated in a close-spaced diode (CSD) cathode test assembly. Afterwards, each cathode was activated and then emission tested at e beam, inc. Cathode #1 was tested for over 3,000 hours, while cathodes #2 and #3 were each tested for ~10,000 hours. After CSD testing, the cathode pellets were removed for characterization, and they were exposed to oxygen in the ambient environment upon removal from the test assembly.

Scanning electron microscopy (SEM) images were acquired with a dual-beam FEI Helios NanoLab 660 field emission microscope, using immersion mode. X-ray energy dispersive spectroscopy (EDS) analysis was also performed inside the Helios, which is equipped with an Oxford X-max EDS detector (80 mm^2 size). EDS mapping was acquired over extended periods to maximize x-ray counts from the cathode, using drift correction to maintain sample position. Investigation of surface chemical compounds and structures was performed using x-ray diffraction (XRD, Bruker-AXIS D8 Diffractometer) and transmission electron microscopy (TEM, JEOL 2010F). A lift-out lamella sample for TEM examination was prepared using the focused ion beam (FIB) capabilities of the dual-beam FEI Helios NanoLab 660. Analysis of the near-surface (~10 nm) region of the cathodes was performed using x-ray photoelectron spectroscopy (XPS, Thermo K-Alpha), which provided information on surface composition and chemical state.

To complement the SEM characterization of cathode surfaces and W particle morphology, simulation of W crystal shape was performed using the Wulffmaker software suite, which has been widely used for constructing Wulff shapes of particles [103].

4.3 Results and Discussion

4.3.1 Emission Testing

Scandate cathodes were subjected to CSD testing in a standard planar diode test geometry. The cathodes were assembled in test vehicles and were sealed in glass tubes that were pumped and baked at 400°C for four days. After this, the tubes were pinched off and the barium getters were flashed. Emission testing was performed at a temperature 50ºC above the knee temperature, and cathodes were pulsed at approximately 5% duty. Emission current as a function of W brightness temperature is plotted in Fig. 4.1. The knee temperature is defined as the intersection between lines extrapolated from the temperature limited (TL) and space charge limited (SCL) regimes. For the three cathodes tested here, the knee temperature ranged from 820 to 837 °C_b. These are significantly (>100 °C_b) lower than that of a typical M-type cathode [10]. It is noted that the knee temperatures of these scandate cathodes are 50 to 70 °C_b higher than those reported for the scandate cathodes prepared by Wang et al [24]using the L-L doping method. This may arise from the different materials used for temperature measurement in each study: Wang et al. based their temperature measurements on Mo brightness, while the W brightness scale was used to measure temperature in the current study (the relevant W temperature is ~37˚C higher than the Mo temperature, accounting for differences in metal emissivity). The difference also results from use of a guard aperture for the cathodes in the current study, whereas cathodes

measured by Wang et al. did not include a guard aperture (which causes an additional 41˚C discrepancy in temperature). Moreover, the cathodes studied here exhibited sharp knee temperatures, which represent the overall transition from TL emission to SCL emission. A thermionic cathode with a sharp transition enables it to reach an optimum emission level more effectively than a cathode with a gradual transition, and thereby makes such a cathode well suited for use in a traveling wave tube or similar device [10]. It should be noted that, over time, knee points for all dispenser cathodes typically migrate to a higher temperature, due to diminished supply of Ba to the cathode surface [10].

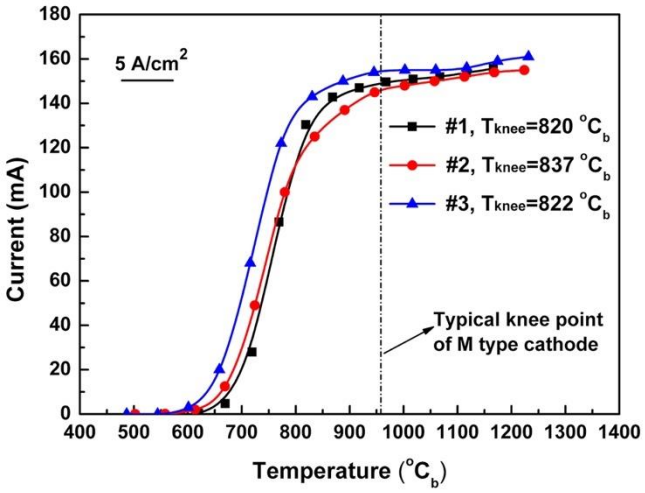

Figure 4.1 CSD test results for three cathodes investigated here. Emission current as a function of cathode (W pellet) brightness temperature (°C_b). The knee temperatures were 820 °C_b, 837 °C_b and 822 °C_b.

4.3.2 Characterization of Cathode Surface Morphology

The three scandate cathodes subjected to CSD testing (Fig. 4.1) displayed consistent emission behavior, in terms of knee temperatures as well as TL and SCL slopes. Moreover, after CSD testing, the surfaces of these cathodes exhibited a consistent set of characteristic surface features, which are described in detail in this section. While observations for a

particular scandate cathode (specimen #1) are presented here, the surface features are fully consistent with those of cathodes #2 and #3, as well as other cathodes evaluated separately after successful CSD testing. These features appear to be representative of cathodes that exhibit good emission behavior.

The high-resolution images in Fig. 4.2 represent the typical surface morphology of the scandate cathodes in this study. Macroscopically, as seen in Figs. 4.2a and 4.2b, the scandate cathode surface appears relatively flat and smooth, with several visible cracks. Figs. 4.2c and 4.2d are a corresponding pair of secondary electron (SE) and backscattered electron (BSE) images, respectively, which show that the pores and tungsten particles were uniformly distributed and the pores were free of debris. Another set of SE and BSE images at higher magnification is presented in Figs. 4.2e and 4.2f, where the tungsten particles were seen to exhibit an equiaxed shape with facets and ledges decorated with nanoparticles of materials with lower atomic number (darker particles in BSE mode, Fig. 4.2f), with particles consistently exhibiting one of two gray levels in the images. These nanoparticles, labeled A and B in Fig. 4.2f, are on the order of 100 nm in size and exhibit distinct contrast with the underlying W. It is noted that in many cases, particles of type A and B are located adjacent to one another. An additional type of nanoparticle was also typically observed on W surfaces, and can be recognized as the smallest bright dots in Fig. 4.2e. These smaller nanoparticles, denoted as type C, are on the order of 10 nm in size and were initially presumed to be barium/barium oxide, based on literature reports [52,111]. It appears that the distribution of these particles (type C) varies from facet to facet, and is discussed in more detail below. As reported in the literature [112], particles similar to type C (with comparable size and distribution) have been observed elsewhere, but were identified as Ba-

Sc-oxide based on Auger electron spectroscopy (AES) results. In that study, it is possible that the Sc signal originated from larger Sc_2O_3 particles located in the vicinity of the 10 nm nanoparticles, as suggested by the results provided there. For all three types of nanoparticle observed on cathode surfaces in the current study, a detailed discussion of their composition is presented in the next section.

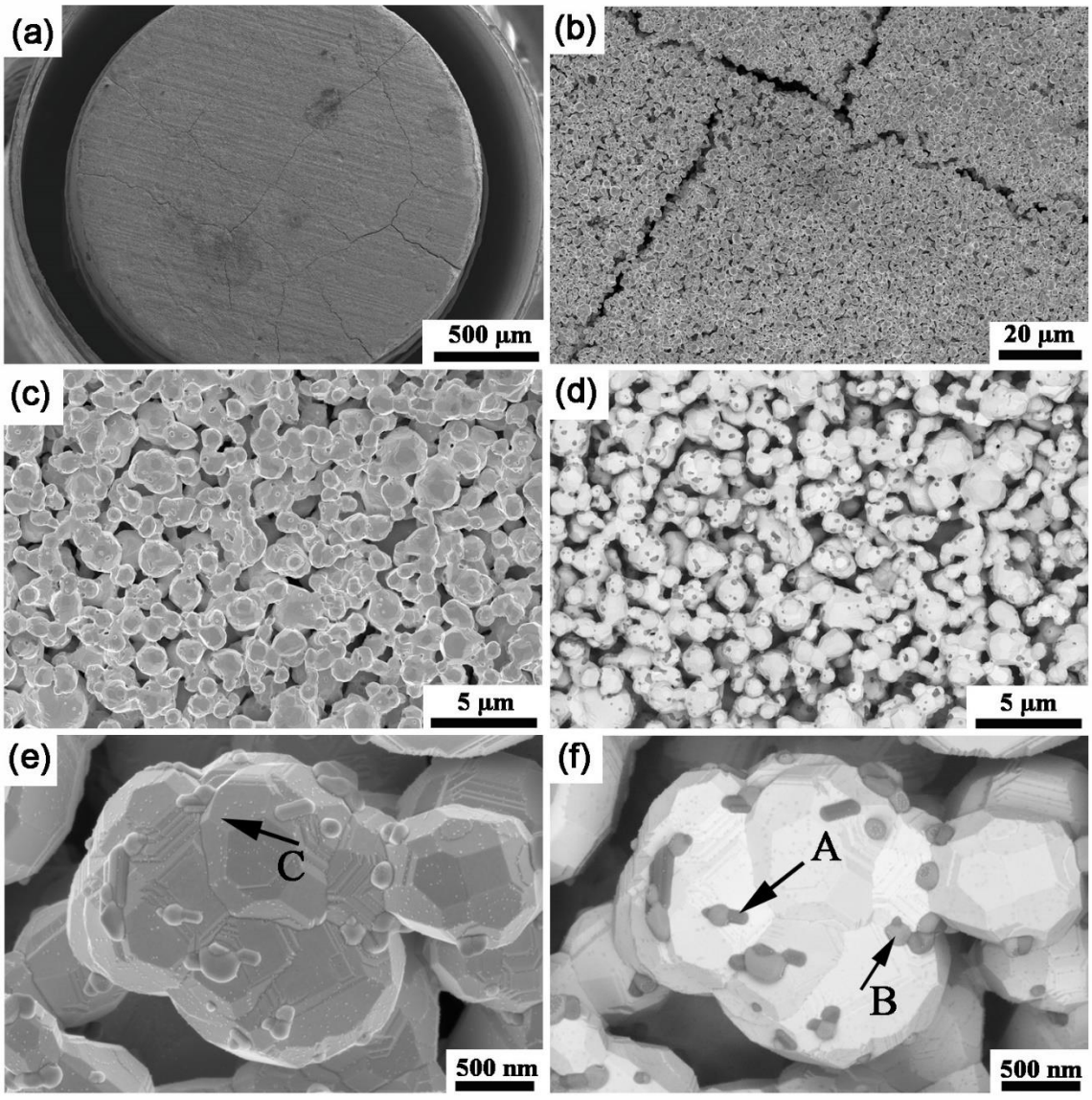

Figure 4.2 SEM micrographs acquired on a typical surface region of a scandate cathode. (a) and (b) Low-magnification images showing a flat surface with visible cracks. (c) Secondary electron (SE) micrograph and (d) corresponding backscattered electron (BSE)

micrograph. (e) SE and (f) BSE image pair at higher magnification, showing faceted and equiaxed W particles, with nanoparticles decorating the facets.

Tungsten particle size distribution was quantified and is presented in Fig. 4.3. For this step, 540 particles were measured and analyzed with ImageJ software. This analysis yielded an average tungsten particle size of 1.17 μm and a standard deviation of 0.45 μm. This is similar to the particle size distribution reported by another group's study of a separate scandate cathode [105]. Comparing these measurements to those of the precursor powder material (scandia-doped tungsten), which had an average size of ~0.5 μm, it appears that the tungsten particles grew significantly during the high-temperature stages of processing or testing [44]. It is noted that the average size of tungsten particles exceeds the range (100 to 500 nm), where the kinetics of W diffusion are sufficiently fast to achieve (near) equilibrium crystal shapes, as suggested by Jacobs et al. [94]. It is noted that most W particles have a size ≥1 μm, as seen in the size distribution plot. Moreover, a portion of the grain population exhibits size ≥2 μm, which may be due to agglomeration of particles during pressing, sintering and growth during thermal processing. The effect of tungsten particle size on cathode performance is not clear. However, a uniform size distribution of tungsten particles is advantageous for generating a homogeneous microstructure in the scandate cathodes, which in turn should be favorable for diffusion of active substances from the porous body of the cathode to its surface, as well as for achieving uniform emission [58,70,73,74,113].

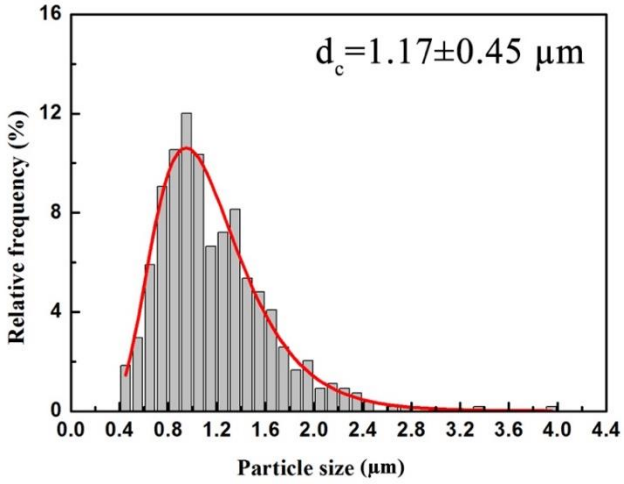

Figure 4.3 Size distribution of W particles, as measured on scandate cathode surfaces. The average size of W particles (d_c) was 1.17 μm, as fitted by a lognormal function.

Two noteworthy features of the scandate cathode surface morphology are the facets and ledges that exist on W surfaces. The various facets of W particles observed here can be matched with high precision to a calculated equilibrium tungsten crystal shape utilizing Wulffmaker [103], as depicted in Fig. 4.4. Details of the fundamental theories used to calculate equilibrium crystal shapes have been introduced and described elsewhere by the software developers [103]. By specifying the crystal symmetry, orientation of surface planes, and relative surface energy for each plane, the resultant particle shape can be calculated and displayed by Wulffmaker. The equilibrium shape (Fig. 4.4a) that matches W grains observed in this study was calculated to have surface energies for {100}, {110} and {112} planes in the ratio of 1:1.08:1.02. Note that these relative surface energies were identified via systematic variation, and deviations as small as 0.01 result in Wulff shapes with facets that do not match experimental observations (e.g. when relative dimensions of facets are compared). The surface of this Wulff shape includes 6 {100} planes, 12 {110} planes and 24 {112} planes. The {112} facets correspond to a heptagon (with two short

sides), the {100} planes to a square, and the {110} planes to a rhombus. The Wulff shape in Fig. 4.4a has been rotated to show that it matches the experimental result in Fig. 4.4b, corroborating the calculated equilibrium shape for W grains on the scandate cathode surface and the anisotropic surface energy that depends on facet orientation. Figs. 4.4c and 4.4d display views of two additional W particles with different orientations, and these have also been matched to the same Wulff shape, after appropriate rotation, as shown in the insets. Further examples can be seen in Figs. 4.5 and 4.6, which also exhibit agreement between the calculated Wulff shape and experimentally observed W particles.

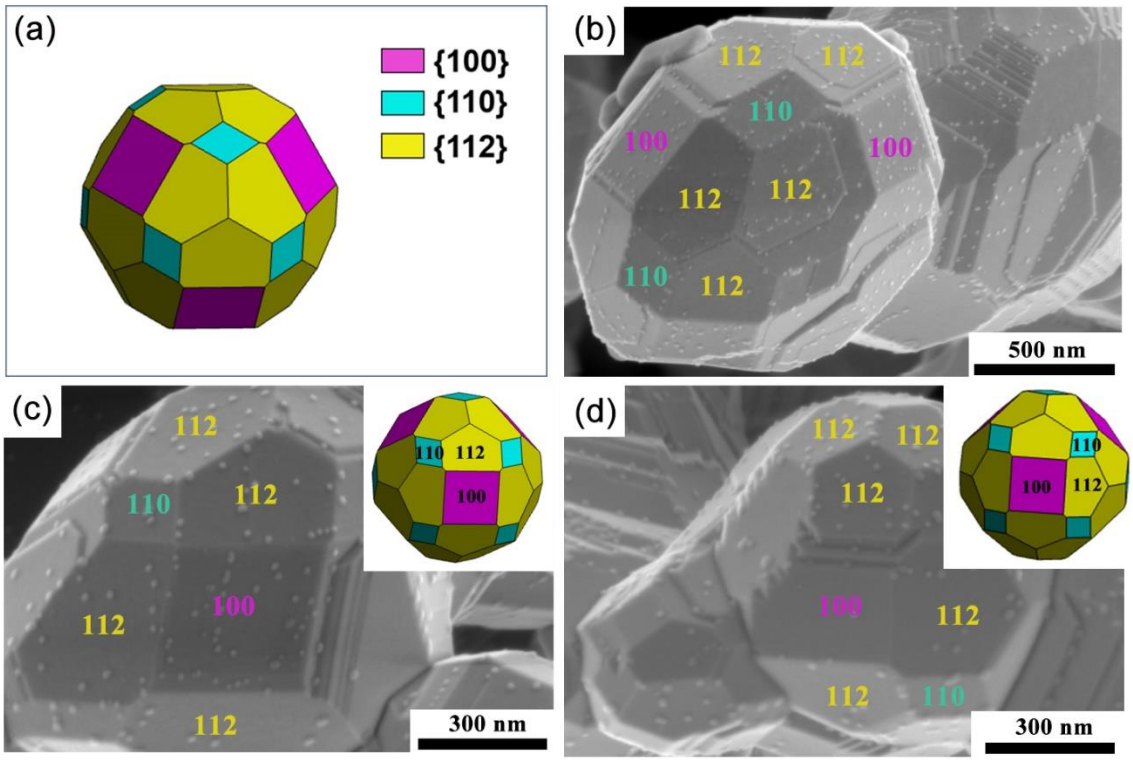

Figure 4.4 Wulff construction of ideal W crystal shape utilizing Wulffmaker. (a) Calculated crystal shape for W that matches experimentally observed grains. (b) SEM image of W particle in the same orientation as the Wulff shape in (a), showing agreement between experiment and calculation. (c) and (d) Two additional W particles with different orientation, both of which match the same calculated Wulff shape when rotated appropriately (inset).

The total emission current for a cathode will scale with the area of the emitting surface, and it is reasonable to expect that different surface facets may have different work functions [94,114], thereby resulting in dissimilar levels of electron emission from each facet type. This would also be reflected in the Richardson-Dushman equation [6], via the Richardson constant *A*, which is a fitting parameter for a given emitting surface. As discussed in reference [115] it was shown that the value of the parameter A can range from 125 to 15 for {112}, {100} and {110} crystal planes in tungsten. To better relate the surface faceting to electron emission from W grains that have the calculated Wulff shape described above, the relative proportions of each facet type were determined. Using the Wulffmaker software, the total surface area for each facet orientation was computed and the results are shown in Table 1. It is seen that {112} facets dominate the total surface area, representing over two-thirds of the surface for this ideal crystal shape. Given the excellent CSD test performance of the scandate cathodes studied here, as well as research findings from other groups showing that electron emission differs appreciably with W facet orientation [94,116,117], it is inferred that {112} facets are likely the most favorable for enhanced electron emission. Similar computational work has been reported in a recent paper [114], where it was shown that the experimentally observed (near) equilibrium W crystal shape was governed by the Ba-O adsorbate ($Ba_{0.5}O/W_{(100)}$, $Ba_{0.25}O/W_{(110)}$ and $Ba_{0.5}O/W_{(112)}$) and the presence of an oxygen-poor environment with a chemical potential (μ_0) between -8.5 and -8.0 eV/at. This agrees qualitatively with the findings reported by Jacobs et al. [94], which demonstrates that both low-index and high-index surfaces for various Ba_xO_y ($x/y<1$) compositions may exhibit low surface energy and low work function.

Table 4.1

Computed values of relative surface energy and proportion of total surface area for each facet type, based on the ideal crystal shape from the Wulff analysis (see Fig. 4a). Normalized surface energy is reported with respect to the surface energy of a {100} facet.

Facet type (orientation)	Normalized surface energy from Wulff construction	Number of facets on surface of ideal W crystal shape	Fraction of total surface area (%)
{100}	1	6	20.8
{110}	1.08	12	10.3
{112}	1.02	24	68.9

To fully characterize the surfaces of scandate cathodes, the smallest nanoparticles (average size 10-20 nm) were carefully studied. As discussed above, these particles may consist of Ba or BaO, based on reports in the literature [52,111]. As illustrated in Fig. 4.5, high-resolution SEM images were used to determine the size of the Ba/BaO nanoparticles, as well as their density on a given surface. Fig. 4.5a presents a representative micrograph of a W particle, showing the Ba/BaO nanoparticles that decorate the various facets. The areal density of nanoparticles appears to depend on the orientation of the W facet. As before, the inset in Fig. 4.5a shows the corresponding simulated Wulff shape with facets. For the W particle shown in Fig. 4.5a, the average number of Ba/BaO nanoparticles is as follows: 82 on {100} facets, 15 on {110} facets, and 43 on {112} facets. These data are plotted in Fig. 5b and reflect the large variations in number of nanoparticles on each facet type. It is noted that the relative sizes of facets measured for the W particle of Fig. 4.5a do not exactly match the relative sizes of facets in the ideal Wulff shape, since the microfaceted region between large facets was not counted as part of the measured facet area. Therefore, the number density of particles was also calculated on an areal basis.

In order to obtain measurements that are more broadly representative of the nanoparticle distributions over scandate cathode surfaces, 15 W grains were imaged at high magnification. These micrographs included a total of 18 {100} facets, 33 {110} facets and 59 {112} facets, each imaged in an orientation near plan-view (i.e., along a direction normal to the facet). These allowed quantitative evaluation of the Ba/BaO nanoparticles, including areal density (number of particles per square micron) and average size of Ba/BaO nanoparticles, with both values measured separately for each of the {100}, {110} and {112} facet types. The results are presented in Figs. 4.5c and 4.5d. The Ba/BaO nanoparticles on each facet were measured using ImageJ software. The areal density of Ba/BaO nanoparticles on {100}, {110} and {112} facets was found to be 360, 91.1 and 190 particles per μm^2, respectively, with corresponding average size of 13.7, 17.1 and 14.7 nm. Nanoparticle size does not appear to vary significantly with facet orientation, considering the measurement error as represented by standard deviation. However, it is noted that Ba/BaO nanoparticles are more densely distributed on {100} and {112} facets, relative to {110} facets. One possible reason for this variation in Ba/BaO areal density may be the presence of atomic-height steps on surface facets, with different densities of these steps on each facet type. Such steps could serve as preferential nucleation sites for the formation of Ba/BaO nanoparticles. If {100} and {112} facets exhibit more atomic-height steps than {110} facets, this could explain the different areal densities of nanoparticles measured here. Using SEM, it is challenging to resolve these steps, which should have a height of only one or several atomic layers. However, it was observed that Ba/BaO nanoparticles on some facets were distributed along a line, e.g., as shown by the black arrow in Fig. 5a. This suggests the presence of a surface defect, such as an atomic-height step, acting as a

preferential nucleation site. Some of these surface defects are long, as indicated by the linear distribution of Ba/BaO nanoparticles across an entire facet (black arrow in Fig. 5a), while others are relatively short and correspond only to a small number of Ba/BaO nanoparticles.

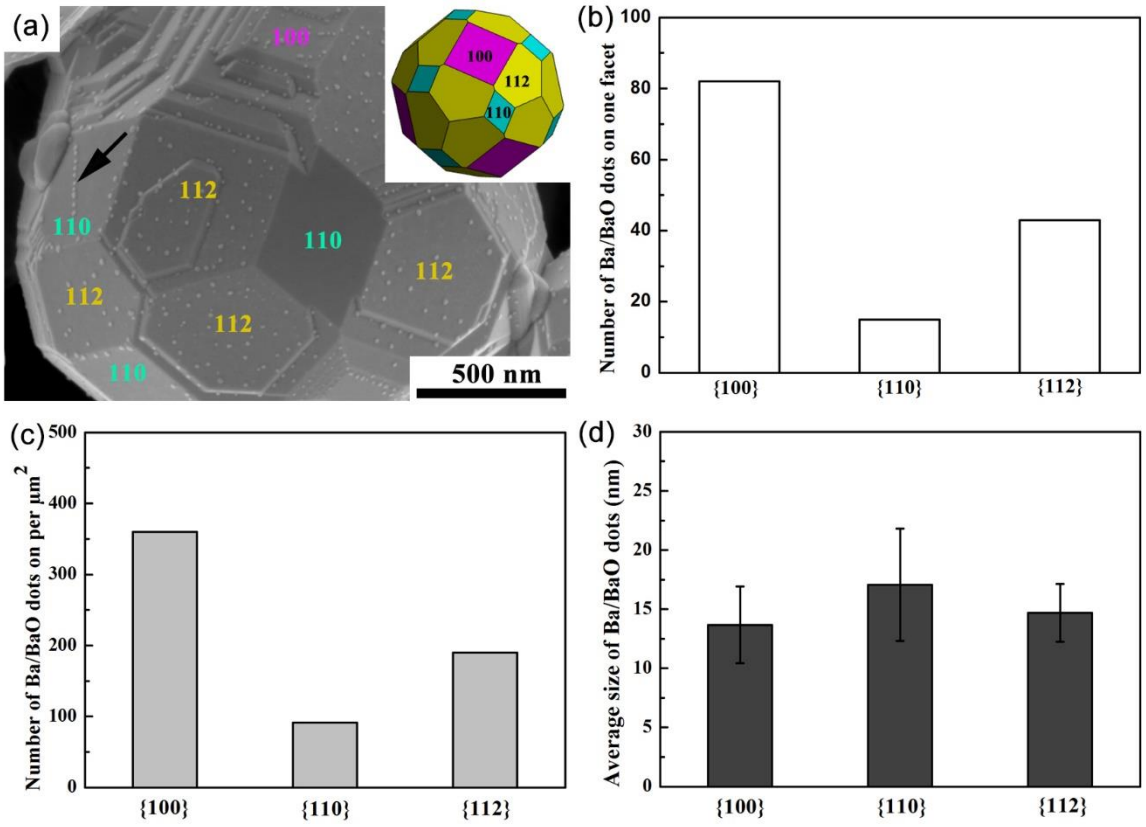

Figure 4.5 Quantitative characterization of Ba/BaO nanoparticles on various facets of W particles. (a) Typical SEM micrograph of faceted W, with calculated crystal shape (inset). (b) Average number of Ba/BaO nanoparticles on each facet type, for the W particle in image (a). Based on measurements of 15 tungsten particles, (c) areal density of Ba/BaO nanoparticles and (d) average size of Ba/BaO nanoparticles, for each facet type.

Another noteworthy morphological feature of these scandate cathode surfaces is the presence of microfaceting between neighboring facets. The tungsten grains exhibit {100}, {110} and {112} facet types, but as can be seen by careful examination of the Wulff shape, there are only three distinct combinations of neighboring facet types, consistent with

observations in this study. As shown in the SEM micrographs of Fig. 4.6, microfaceting was observed: near the intersection of {100} and {112} facets (Fig. 4.6a); between {110} and {112} facets (Fig. 4.6b); and near the intersection of {112} facets with other {112} facets (Fig. 4.6c). Typical examples of microfacets appearing between {100}/{112} facets, {110}/{112} facets and {112}/{112} facets are indicated by black arrows in Figs. 4.6a, 4.6b and 4.6c (with each inset showing a Wulff shape corresponding to the W particle). In order to quantify the relative degree of microfaceting at each type of intersection, 21 micrographs were analyzed, with a summary of these results presented in Fig. 6d. Note that for counting each type of facet pair, the standard deviation was used to represent the error. Here it is observed that the normalized number of microfacets at each intersection varies slightly according to the type of facet pair, with {100}/{112} facet pairs exhibiting the greatest number of steps and {110}/{112} facet pairs exhibiting the lowest number of steps. The faceted W surface morphology and the presence of microfacets indicate that W grains are evolving toward the equilibrium crystal shape.

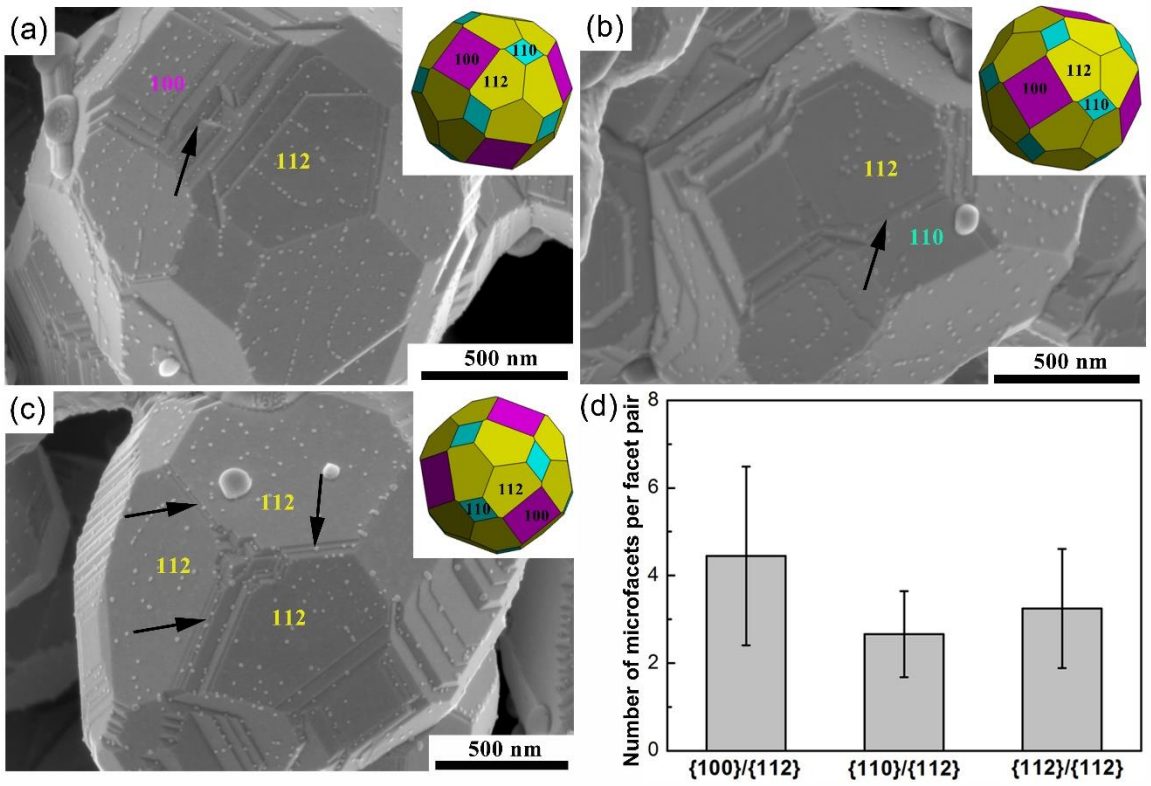

Figure 4.6 SEM micrographs for measurement of steps within microfaceted regions between adjacent facet pairs. Representative examples of these microfacets are shown for (a) {100}/{112} facets, (b) {110}/{112} facets, and (c) {112}/{112} facets. 21 W particles were observed, and the number of steps within each microfaceted region was counted, with average normalized results presented in the bar chart of (d).

4.3.3 Chemical Analysis

In addition to the Ba/BaO nanoparticles on the surface facets of tungsten particles, there appear to exist two other types of oxide particles, as seen in Fig. 4.7. These different oxide particles are often located adjacent to one another, as indicated for example by the black arrows in Fig. 4.7b. Each particle type appears with a different gray level in this BSE image, due to differences in average atomic number of the constituent elements. Particle A represents the darker of the two types, and therefore type A particles should have a lower average atomic number than type B. EDS spot analysis was performed in conjunction with

BSE imaging to identify the composition and location of these particles. At least five EDS spot analyses were performed for each particle, delivering consistent results. Using EDS, the composition measured for particle A was 2.2 at.% Sc, 22.2 at.% O, and 75.6 at.% W. The high W content is most likely due to the underlying W particle, since EDS sampling depth is on the order of 1 µm and is therefore much larger than the particle size of 100 nm. Importantly, no Ba or Al signal appears in the EDS analysis. Thus, particle type A appears to consist of Sc and O only, and is assumed to be scandium oxide, Sc_2O_3. EDS spot analysis of particle B revealed a composition of 2.0 at.% Ba, 4.2 at.% Al, 32.6 at.% O, and 61.2 at.% W. Sc was not detected here. Assuming that the W signal is due to the underlying W grain, particle type B appears to consist of Ba, Al and O. Noting that Ba and Al exist in an elemental ratio of 1:2, particle type B is interpreted to be the chemically [118,119] and thermally (900-1250 °C) [120] stable oxide $BaAl_2O_4$. Note that the peaks corresponding to Cr, Fe and S in both spectra may arise from the stainless steel chamber walls of the SEM where EDS analysis was performed. As such, these elements were excluded from the quantification of nanoparticle composition.

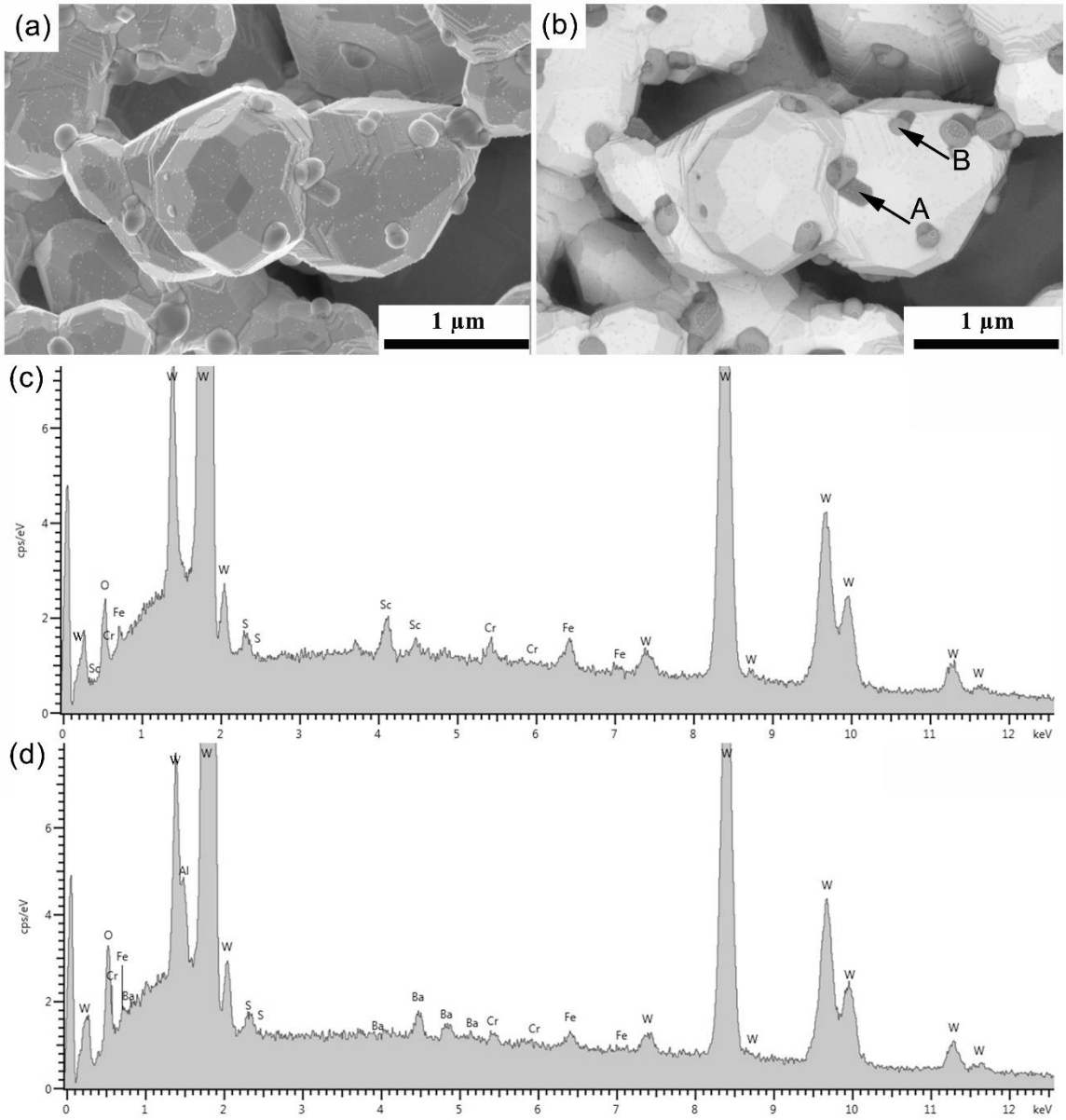

Figure 4.7 SEM images and EDS spectra of the two types of larger (~100 nm) oxide nanoparticles that exist on the tungsten surfaces of scandate cathodes. (a) Image acquired in SE mode for a typical surface area, and (b) the corresponding BSE image of the same area. EDS spectra for the different oxide particles, indicated by black arrows as (c) particle A and (d) particle B.

In addition to EDS analysis at specific points, a broader surface area was scanned using EDS to generate an elemental map, as shown in Fig. 4.8. Particles of type A and B are included in this region, and are visible in the SEM image. In the composite elemental

map, oxide particles on the cathode surface are visible primarily as yellow particles (oxygen is colored yellow here). Noting the correlation between relatively high concentrations of Ba, Al and O in their respective elemental maps, it is clear that most of the oxide particles are of type B ($BaAl_2O_4$). There are also particles of type A (Sc_2O_3), decorating the surfaces of the W grains. These are visible in both the Sc map and the composite map (Sc is colored green here), and are also reflected in the O map. It is noted that, in most cases, Sc_2O_3 particles are accompanied by $BaAl_2O_4$ particles immediately adjacent to them.

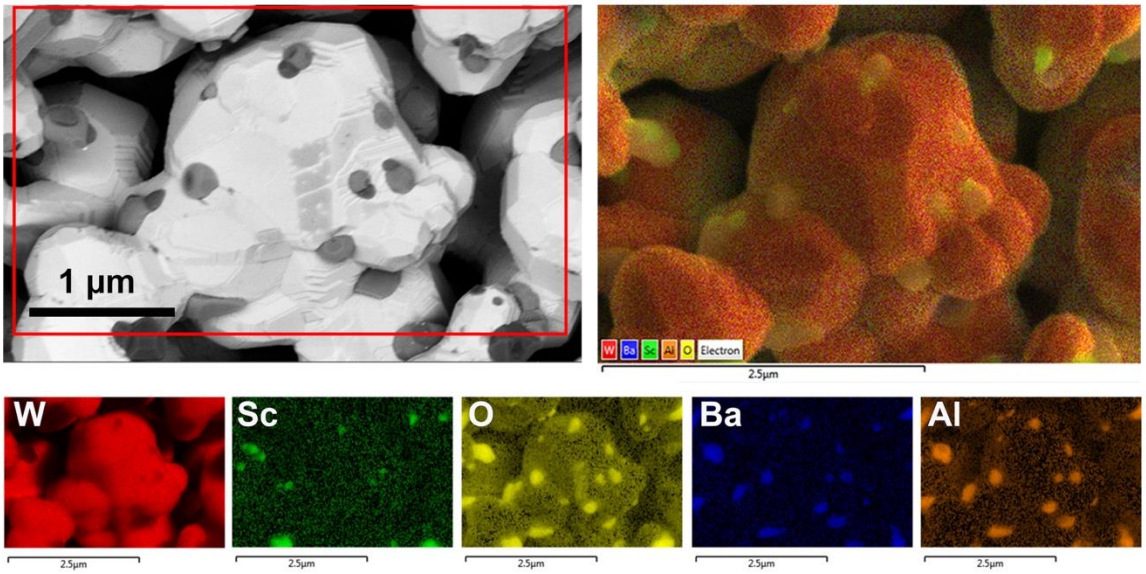

Figure 4.8 EDS elemental map of a typical scandate cathode surface area. An SEM micrograph (BSE imaging mode) is shown at upper left, and a composite map showing the distribution of all relevant elements is shown at upper right. Additionally, individual maps indicate the elemental distributions of W, Sc, O, Ba and Al.

4.3.4 Quantifying the Amount of Ba on W Surfaces

Impregnation of a porous tungsten pellet with barium-calcium-aluminate is an important step in the processing and fabrication of cathodes. It is generally accepted that

Ba at the surface is continually replenished from the porous body of the cathode during operation at high temperature, in order to maintain an emissive cathode surface [2,9,78]. While there is some disagreement as to whether Ba exists as an adsorbed monolayer, partial monolayer, or as multiple layers, it is generally assumed that a sub-monolayer of Ba completely coats the available W surface atoms [78]. As described above, it was observed here that nanoscale particles (~10 nm in size) decorate the surfaces of W grains. These are thought to be Ba (or BaO) nanoparticles. To evaluate each possibility, the amount of Ba (or BaO) was quantitatively estimated in relation to the number and volume of these nanoparticles observed on W facets.

We hypothesize that the (partial) monolayer of Ba on the high-temperature activated cathode surface forms discrete nanoparticle islands that decorate the surfaces of W particles after cooling. A schematic of these two states is presented in Fig. 4.9. During cathode operation, Ba atoms are assumed to be distributed uniformly over the W facets, as some fraction (or multiple) of a monolayer. It is noted that the cathode activation and service temperatures are well above the melting point of Ba. When a cathode is switched off and cools to room temperature, the Ba may form islands via nucleation and growth at step edges on the facets, resulting in the observed hemispheres that decorate W surfaces. When exposed to air, after removal from the vacuum tube and prior to insertion into the electron microscope, these Ba islands should oxidize and become BaO.

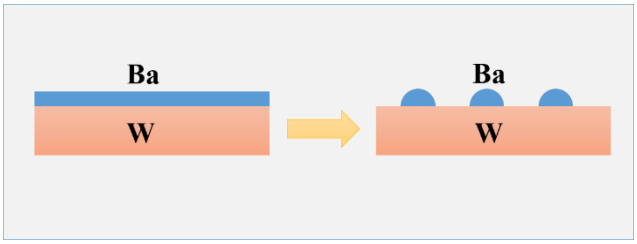

Figure 4.9 Schematic of the proposed transformation model, illustrating the reorganization of Ba adatoms on the W facets of a scandate cathode. During cooling, the surface layer of Ba atoms transforms into discrete nanoparticles that decorate the W facets. These nanoparticles would subsequently oxidize upon exposure to air.

The areal density (number of nanoparticles per area) and the size of Ba/BaO nanoparticles were measured directly from SEM micrographs, and these data were included in the plots presented earlier in Fig. 4.5. Although it is believed that these nanoparticles contain Ba, it is not known whether they are metallic Ba or oxidized BaO (the latter option is more likely, but both possibilities are considered here for completeness).

In order to determine how much adsorbed Ba (excluding oxygen, e.g., in the case of BaO nanoparticles) exists on the W surfaces, the number of Ba atoms per unit surface area (nm^2), n, has been calculated as:

$$n = \frac{10^{-6} N * \frac{2}{3}\pi(\frac{d}{2})^3}{a^3} * N_{Ba} \qquad 4.1$$

where N is the areal density of Ba/BaO nanoparticles (number per μm^2), and d is the corresponding measured average diameter of the nanoparticles. Since it is not yet known whether these nanoparticles are metallic Ba, or perhaps BaO, the calculation of n was performed separately for each case. Ba and BaO are different materials, each with a distinct lattice parameter a and different number of Ba atoms per unit cell (N_{Ba}). Metallic (elemental) Ba has the body-centered cubic crystal structure, with two Ba atoms in the unit cell and lattice parameter of 502.8 pm. BaO has the rock salt structure, with four Ba atoms in the

unit cell and lattice parameter of 561.5 pm. In order to simplify the calculations involving Eq. 1, it was assumed that the Ba/BaO nanoparticles are hemispherical. This assumption is consistent with high-magnification SEM observations, such as the images in Figs. 4.6a and 4.6c, which reveal nanoparticles with hemispherical profile on the sides of W grains.

An important aspect of Eq. 1 is that it allows the conversion of measured quantities (*N* and *d*), which together can represent the volume of nanoparticle material per unit surface area of W, into the number of Ba atoms per unit surface area of W, for each possible phase (Ba or BaO). Along with measured values of *N* and *d*, the results for *n* are listed in Table 2. For each W facet plane orientation, the area of the corresponding plane from the W unit cell was calculated. This value, along with the value of *n* for the corresponding facet and material phase, allows the calculation of the number of W unit cells associated with each Ba adatom in the surface layer (assuming equal distribution of Ba across W surfaces at cathode operating temperature). It is seen from Table 2 that approximately two to four W unit cells would be associated with each Ba adatom. This implies that the Ba adatoms, assuming they exist in the metallic (non-oxidized) state at cathode operating temperature, could form a monolayer or sub-monolayer on the cathode surface. This is consistent with accepted notions of the emitting surface for B-type cathodes, as well as certain studies of scandate cathodes [8].

Table 4.2

Measured and calculated values related to the amount of Ba on the surface of W. The existence of metallic Ba or oxidized BaO was considered, including calculation of the corresponding surface density of Ba adatoms in each case. This also allowed the determination of how many W unit cells are associated with one Ba adatom, for each combination of W facet orientation and Ba/BaO material phase.

		N	*d*	*n*		
Material Phase	Tungsten Facet Plane	Areal density of Ba/BaO nanoparticles per μm^2	Average diameter of Ba/BaO nanoparticles (nm)	Number of Ba atoms per nm^2	Surface area of W unit cell in facet plane ($*10^{-2}$ nm^2)	Number of W unit cells needed to hold one Ba adatom
Ba	{100}	360	13.7±3.2	3.80	10.0	2.63
	{110}	91.1	17.1±4.8	1.87	14.2	3.77
	{112}	190	14.7±2.4	2.47	12.2	3.33
BaO	{100}	360	13.7±3.2	5.45	10.0	1.83
	{110}	91.1	17.1±4.8	2.68	14.2	2.63
	{112}	190	14.7±2.4	3.55	12.2	2.30

The calculated values in the last column of Table 2 were also compared to theoretical values of the Ba adatom distribution that would be expected for each W facet. Fig. 4.10 depicts the theoretical coverage of Ba on W, accounting for the size of the Ba adatom with respect to the W surface sites available on each facet. It is noted that the particular location of each Ba atom over the atomic arrangement of W surface atoms represents one of several possibilities for each facet. While it is possible that the Ba adatom may sit at a slightly different position, the number of W unit cells required to accommodate one Ba atom will be the same on a given facet. It can be seen from Fig. 4.10 that four unit cells of the W surface are needed to hold two Ba adatoms, and this applies to all three W facet orientations

considered here. Therefore, half of one monolayer (0.5 ML) of Ba adatoms on the cathode surface at operating temperature would imply a ratio of two W unit cells for each Ba atom, which agrees very well with the values in the last column of Table 2, calculated for the case of BaO nanoparticles. Note that the {100} and {112} facets represent 90% of the surface area for the Wulff shape described earlier (see Table 1). These facets also account for ~85% of the Ba/BaO nanoparticles measured per unit surface area (see Fig. 4.6c). Therefore, the calculated values of Ba coverage for these facets are more reliable, and together they corroborate the ratio of two W unit cells for each Ba adatom. Given the propensity of Ba to oxidize, one would expect the nanoparticles to be BaO (rather than metallic Ba) after exposure to air. Therefore, the observations and calculations presented here strongly suggest that the ~10 nm nanoparticles on W facets are BaO, and that the cathode surface is nominally covered with 0.5 ML of Ba adatoms during high-temperature operation.

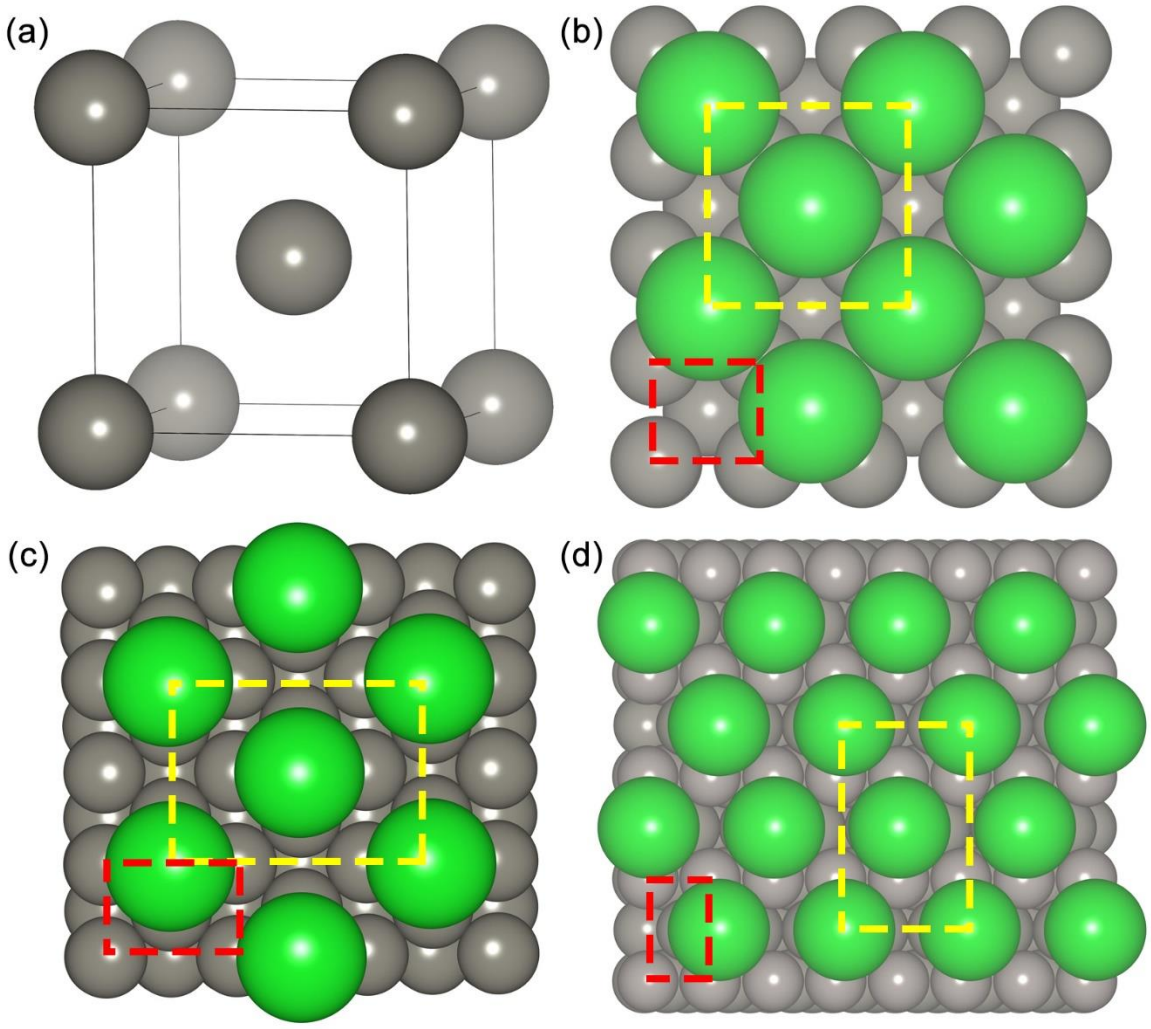

Figure 4.10 Theoretical positions of Ba adatoms on {100}, {110} and {112} W surface facets. (a) Unit cell of W. The relevant surface structures are shown for each facet: (b) the {100} surface plane; (c) the {110} surface plane; (d) the {112} surface plane. Red rectangles indicate unit cells on the W surface for {100}, {110}and {112} orientations, while yellow rectangles represent unit cells for adsorbed Ba (two Ba atoms lie within each of these unit cells). In all cases, four W unit cells are required to accommodate two Ba atoms, for complete coverage of Ba atoms on the W surface.

4.3.5 XRD, XPS and TEM Analysis

XRD scans were performed to determine the phases present on the surface of scandate cathodes as presented in Fig. 4.11. Three peaks were detected for the body-centered cubic (BCC) W phase, and all diffraction peaks were shifted to slightly higher 2θ

values versus expected peak positions. Specifically, the (110), (200) and (112) peaks were shifted higher by 0.055˚, 0.064˚ and 0.068˚, respectively, suggesting that the lattice parameter of W in the cathode may be smaller than expected for pure (elemental) W.

As mentioned above, the W grains at the surface of the cathode were decorated with Sc_2O_3 and $BaAl_2O_4$ nanoparticles (both on the order of 100 nm diameter), as well as BaO nanoparticles ~10 nm in diameter. Given the low overall volume fraction of these nanoparticles and their small size, it is possible that the diffracted x-ray intensity from these compounds is sufficiently small that the W signal dominated the XRD scans. Moreover, these XRD scans support the comments made above regarding the lack of a semiconductor layer on the surface of W particles, since the presence of a ~100 nm thick oxide layer should result in the appearance of corresponding peak(s) in the XRD scan.

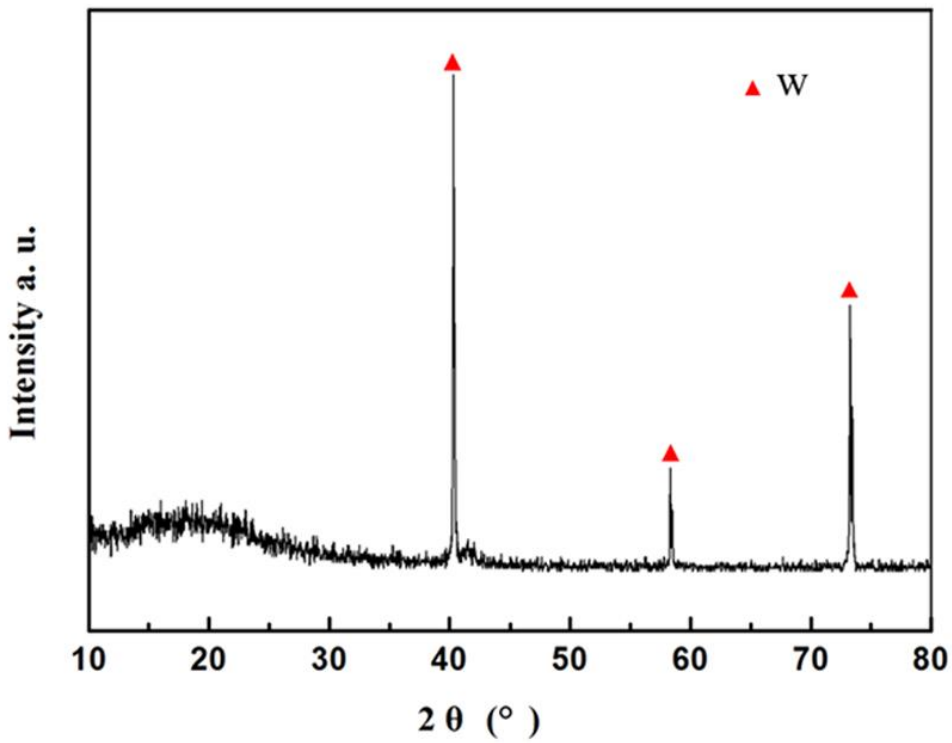

Figure 4.11 XRD scan of the scandate cathode. The peaks detected here were all attributed to the BCC tungsten phase; no oxide peaks were observed.

XPS measurements of the surface of scandate cathode #1 detected Ba 3d, Al 2p, O 1s, Sc 2p, Ca 2p and W 4f peaks, as depicted in Fig. 4.12. In order to calibrate the energy scale for the spectra, the C 1s peak at 284.6 eV was used as a reference for charge correction. As seen in Fig. 4.12a, the spectrum around Ba 3d can be divided into three sets of doublet peaks, with each set corresponding to a particular local bonding environment for Ba. The doublet peaks with binding energies of 795.4 eV (Ba 3d3/2) and 779.6 eV (Ba 3d5/2) are assigned to BaO, and these are attributed to the ~10 nm BaO surface nanoparticles, based on the discussion above. The other two sets of doublet peaks at 794.9 eV, 794.2 eV (Ba 3d3/2) and 780.2 eV, 779.5 eV (Ba 3d5/2) are attributed to the two Ba^{2+} sites in $BaAl_2O_4$ [121,122]. In Fig. 4.12b, the Al 2p region of the spectrum exhibits a single peak at 73.4 eV, which may be characteristic of Al species in AlO_4 tetrahedra [122,123]. As seen in Fig. 4.12c, the 1s spectrum of O is fitted with 3 peaks in which the binding energy at 531.4 eV can be ascribed to O species in $BaAl_2O_4$, while the peak at 529.7 eV may arise from the O species in surface hydroxyl groups from H_2O molecules adsorbed on $BaAl_2O_4$ [122]. Additionally, the peak at 530.2 eV in the O 1s spectrum may be associated with BaO or Sc_2O_3. The presence of Sc_2O_3 surface particles on W grains is consistent with the measured Sc 2p spectrum, which exhibits doublet peaks at 405.8 eV and 401.5 eV, as displayed in Fig. 4.12d and as expected for Sc_2O_3. The Ca 2p spectrum is presented in Fig. 4.12e, although it appears that the amount of Ca is below the detection limit of XPS, implying negligible Ca on the cathode surface. For the W 4f region of the spectrum, as shown in Fig. 4.12f, it is noted that the doublet peaks with binding energies of 36.1 eV and 34.0 eV may arise from WO_2, while the peaks at 32.0 eV and 29.9 eV are observed at lower energy values than expected for metallic W [42].

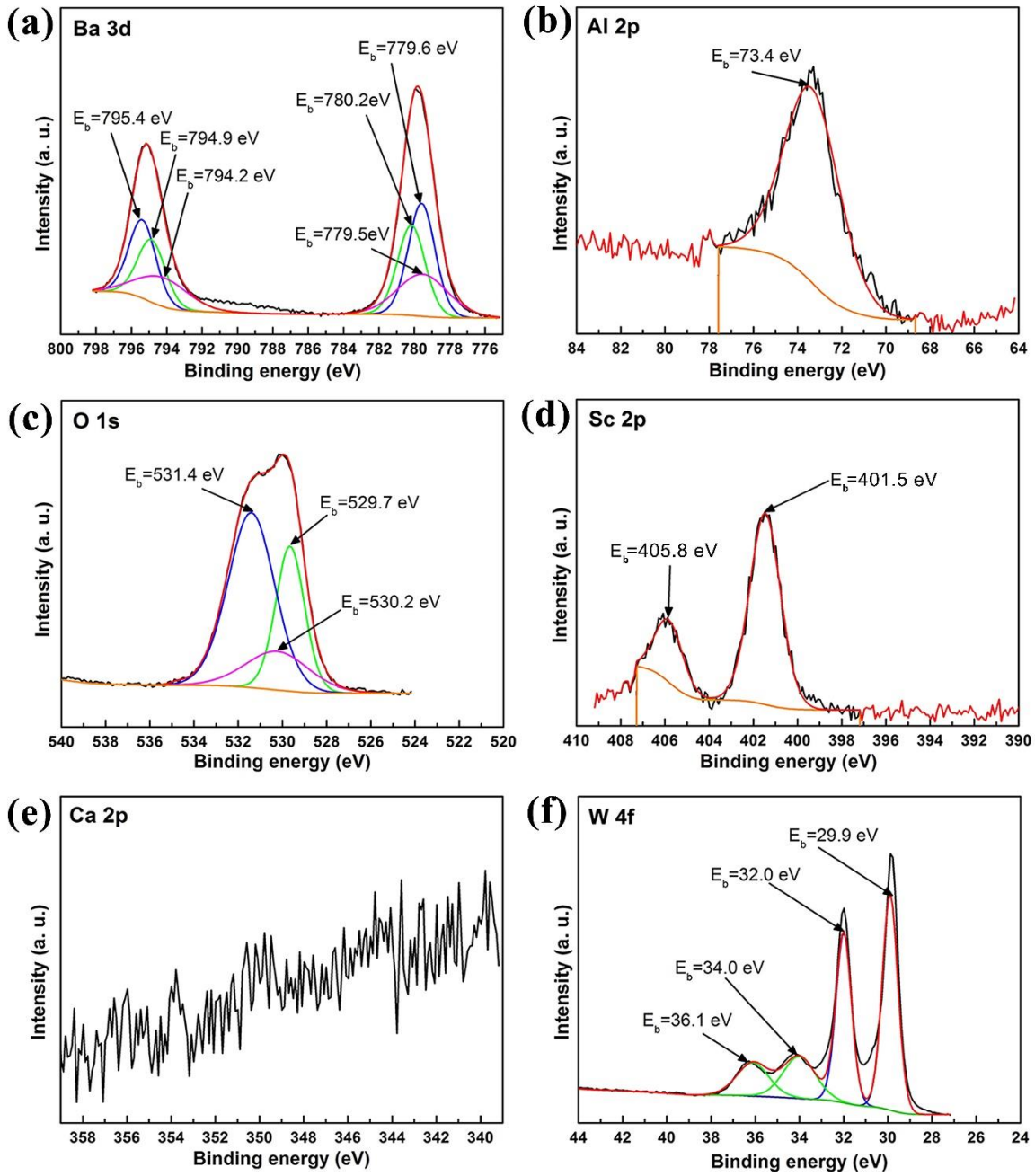

Figure 4.12 XPS spectra for relevant elements expected to exist on the scandate cathode surface. (a) Ba 3d, (b) Al 2p, (c) O1s, (d) Sc 2p, (e) Ca 2p and (f) W 4f.

In order to further investigate the possible existence of a semiconductor oxide layer on the surface of W grains, a lift-out lamella was prepared using FIB techniques and was examined using scanning transmission electron microscopy (STEM), as shown in Fig. 4.13. Figs. 4.13a and 4.13b are conventional bright-field (BF) TEM images of W grains located

near a cathode surface. Flat facets on the W grain surface are visible in the higher-magnification image of Fig. 4.13b, and are indicated by white arrows; note the fairly uniform grayscale level in the W grain, from the center to the surfaces, suggesting that a single phase exists throughout. Note that platinum is typically deposited prior to FIB milling, to prevent surface damage during lamella preparation. Two layers of Pt were deposited with the aid of the electron beam and the ion beam, and are denoted Pt-e (~500 nm thick) and Pt-i (~1 μm thick), as indicated in Fig. 4.13a. Selected-area electron diffraction (SAED) was performed near the surface of the W grain, at location B (marked in Fig. 4.13b), and the diffraction pattern is shown in the inset. This pattern corresponds to the BCC crystal structure and therefore indicates that the near-surface region is simply composed of W, the same material phase that exists at the center of the grain. These observations are also consistent with the Wulff construction discussed above, which was based on W with the BCC structure. Fig. 4.13c presents a high-angle annular dark field (HAADF) image recorded in STEM mode, which exhibits contrast based on differences in atomic number. In this image, the brightness level in the W grain is constant from the center to the surfaces, indicating that the same material phase (BCC W) exists throughout, with no apparent semiconductor oxide layer detected near the surface. Note that the thin white layer on the lower edges of the central W grains (indicated by the blue arrow in Fig. 4.13b) is redeposited W from the FIB milling process, i.e., it is an artifact of TEM specimen preparation. W redeposition is typical during FIB milling; note that the upper edges of the central W grains do not exhibit a similar W layer, since those surfaces had been protected with the Pt coating prior to FIB milling. In Fig. 4.13d, microfacets were observed on the

W grain, adjacent to a larger facet and near a grain boundary. The width of each microfacet ranges from 10 to 20 nm, and each is aligned along one of two facet directions.

This lamella included one oxide particle (~250 nm diameter) attached to the central W grain, marked as location A in Figs. 4.13b and 4.13c. EDS point analysis of this particle indicated a composition of 17.5 at.% Ba, 31.9 at.% Al, and 50.6 at.% O. Similar to the results discussed above (section 3-C), it is seen that Ba and Al exist in an elemental ratio of approximately 1:2. Moreover, no W signal was detected from this particle. The electron probe in the TEM offers significantly higher spatial resolution for EDS measurement, when compared with EDS in the SEM, and there was no W situated above or below the oxide particle in this TEM sample. This allowed an isolated measurement of particle composition. Again, consistent with results discussed previously in section 3-C, this oxide particle is interpreted to be the thermally stable oxide $BaAl_2O_4$.

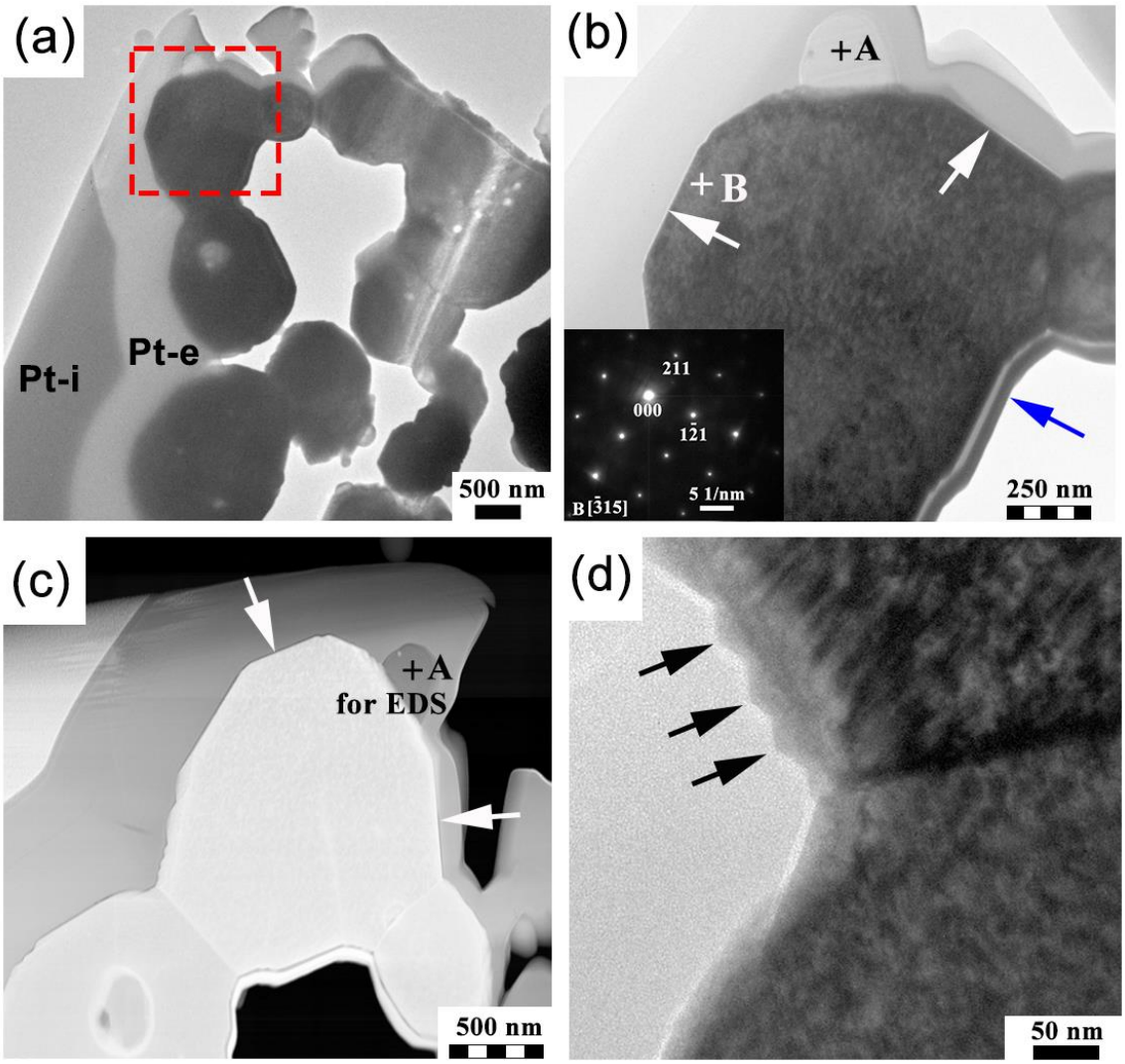

Figure 4.13 TEM observations of a lift-out lamella from a scandate cathode. (a) Low-magnification bright-field image. (b) Higher-magnification image of W particle denoted by red dashed rectangle in (a). Facets are indicated by arrows. Two Pt layers were deposited on the W surface, denoted as Pt-e and Pt-i, to protect the cathode surface during FIB milling. The inset in (b) is a selected-area electron diffraction pattern of the W grain, at location B, indicating the presence of BCC W. (c) High-angle annular dark field STEM image showing atomic number contrast, with uniform brightness up to the surface of the W grain. (d) Bright-field TEM image reveals microfacets on the W surface. No Ba-Sc-O surface oxide layer was observed here. The layer seen at the lower edges of the central W grains (blue arrow in image (b), also visible in image (c)) is redeposited W from FIB milling, and is only observed on surfaces that were not protected by Pt.

4.3.6 Characteristics of Scandate Cathodes and Possible Role of Scandium

Several scandate cathodes that exhibited promising results during close-spaced diode testing were characterized in this study. The tungsten grains on the cathode surfaces were faceted, corresponding to a (near) equilibrium state, and these facets were decorated with $BaAl_2O_4$, Sc_2O_3 and BaO nanoparticles. In addition, the W facets were identified as having the following crystal planes: {100}, {110} and {112}, with {112} facets dominating the surface area. In light of the work conducted by Jacobs et al. [94], it is believed that these faceted tungsten grains should be covered with Ba_xO_y ($x<y$) adsorbates. Moreover, computational work by Zhou [114] suggests that an oxygen-poor environment is necessary for the formation of the faceted tungsten crystal shape observed here. As such, it is possible that the role of Sc in producing well-emitting scandate cathodes is tuning the partial pressure of oxygen in order to establish an oxygen-poor atmosphere around the cathode surface, since the affinity of Sc for O is higher than the affinity of Ba for O [60,124].

4.4 Conclusions

The morphology and surface phases were studied in detail for scandate cathodes that had exhibited good performance during close-spaced diode testing. Cathode surfaces were methodically characterized using SEM, EDS, XRD, and (S)TEM techniques. Several conclusions are drawn, based on the results and discussion above.

(1) Scandate cathode surfaces consist of equiaxed, micron-scale tungsten particles that exhibit a high degree of surface faceting.

(2) Three different types of nanoscale oxide particles decorate the W surfaces after cooldown from testing and exposure to air: $BaAl_2O_4$ (~100 nm length scale), Sc_2O_3

(~100 nm length scale), and BaO (~10 nm length scale). A high number of the finest nanoparticles (BaO) decorate the W facets.

(3) Wulff analysis of the observed equilibrium W crystal shape indicated that the surface facets correspond to {100}, {110} and {112} crystallographic planes. According to this Wulff analysis, the normalized surface energies for these facets are 1.00, 1.08 and 1.02, respectively. The {112} facets dominate the surface area of W grains, and each {100} or {110} facet is surrounded by four {112} facets.

(4) Microfacets exist between neighboring facets, specifically where {100}/{112}, {110}/{112} and {112}/{112} facets meet. The presence of microfacets and the faceted morphology of W grains indicate that these particles are approaching their equilibrium shape during high temperature cathode operation.

(5) The finest nanoparticles (~10 nm length scale) that decorate the W surfaces are believed to be BaO, and are attributed to metallic Ba that coats the surface at operating temperature, and forms hemispheres during cooling of the cathode. This Ba then oxidizes upon exposure to air, when the cathode is removed from the vacuum envelope. Calculations based on size and density of these nanoparticles is consistent with the presence of 0.5 (+0.05/-0.12) ML of Ba adatoms, completely covering the W surfaces during cathode operation.

(6) Despite using multiple characterization techniques to search for a distinct surface phase or coating on the W grains (which has been proposed in multiple models for electron emission from scandate cathodes), no evidence was found for the existence of a Ba-Sc-O semiconducting oxide layer in the top 10 to 100 nm of the near-surface regions of W.

The results of this study provide an overview of the materials and morphology that exist at the surface of scandate cathodes that performed well in CSD testing. Understanding the materials landscape provides insight into the desired physical attributes of scandate cathodes that may inform independent efforts to optimize these devices.

CHAPTER 5. NEAR-SURFACE MATERIAL PHASES AND MICROSTRUCTURE OF SCANDATE CATHODES

5.1 Introduction

Scandia-doped tungsten thermionic cathodes (referred to as scandate cathodes) are promising candidates for application in vacuum electron devices, owing to their reported enhancement of electron emission, delivering higher current densities at lower temperatures [6,10,24,52,94,125,126] than conventional dispenser cathodes, i.e., oxide cathodes [25,96,127,128], B-type cathodes [2,129–131], and M-type cathodes [37,132,133]. Consequently, scandate cathode technology has received significant attention over recent decades. Various scandate cathodes have been developed, including impregnated [18,70,74], pressed [58,65], and top-layered types [53,60,134]. Of these, scandate cathodes fabricated from starting powders of micron-scale tungsten (W) and nanoscale scandia (Sc_2O_3) are reported to exhibit the most promising emission characteristics and have been widely investigated. This scandate cathode variant is a powder metallurgy (P/M) porous tungsten plug fabricated with nanosized scandia-doped tungsten powder and impregnated with barium calcium aluminate (in a specific molar ratio) prior to activation at the proper temperature. In order to enable commercialization and application of scandate cathodes, however, several issues must first be addressed, including emission uniformity, poor reproducibility, and an incomplete understanding of the mechanisms that govern emission [2,8,9,65,78,109,128,135].

These persistent issues are due, at least to some extent, to knowledge gaps in the relationships between processing, microstructure, composition, and emission properties of scandate cathodes. Unlike simple materials, e.g., a binary alloy or binary oxide system,

impregnated scandate cathodes contain various multi-element compounds, scandia-doped W powder mixes, and impregnate materials. In addition, numerous complex reactions occur during the fabrication steps, principally during impregnation and activation processes [65,135]. These issues lead to exceptional difficulty in understanding exactly which phases are present at key locations in scandate cathodes, and which phases are most important to electron emission at service temperature. Apart from the complexity of the cathode microstructure itself, inherent limits to characterization techniques have hindered scandate cathode studies, even though the first scandate cathode was produced in 1967 [55]. Fortunately, instrumentation for materials research, especially electron microscopy, has recently undergone rapid and substantial development, facilitating more advanced investigations of scandate cathodes and an improved understanding of their relevant nanoscale features.

Recent studies by the current authors [6,50] indicate that the surfaces of scandate cathodes that emit well also exhibit highly faceted W grains decorated with nanoscale Sc_2O_3, $BaAl_2O_4$ and Ba/BaO particles. Importantly, even though a ~100 nm thick surface layer containing Ba-Sc-O has been invoked in certain emission models [9,78], no such surface layer or region was detected at or near the cathode surfaces in this study. During the advanced characterization experiments described here, primary focus was on nanoscale structure and composition within the near-surface regions, to better understand the cathode features thought to be involved in thermionic electron emission. This work has yielded new insights into the structure and composition of phases that are revealed in cross-section specimens from scandate cathode surface regions, and which provide a basis for modeling improved emission performance.

5.2 Materials and Methods

The scandate cathodes characterized in this paper were prepared with W precursor powder mixed with nanoscale scandia, and this powder mixture had been prepared using the liquid-solid (L-S) technique. Detailed procedures of the L-S approach can be found in an earlier paper by one of the authors [10]. Multiple scandate cathodes were provided by e beam inc., where emission testing was also performed. Fabrication included the following steps: for each cathode, the W-scandia powder mixture was pressed into a pellet ~2 mm diameter and ~1 mm tall; then the pellet was sintered and subsequently impregnated with barium calcium aluminate ($6BaO\text{-}1CaO\text{-}2Al_2O_3$); afterwards, the sample was washed with deionized water to remove residual impregnate material; finally, the cathodes were activated by heating at 1150 $^{\circ}C_b$ for 1 hour. Prior to microstructural characterization, two cathodes (designated cathode #1 and cathode #2) were emission tested in a close-spaced diode (CSD) configuration. These scandate cathodes exhibited excellent emission capabilities as indicated by knee temperatures of 820 $^{\circ}C_b$ and 837 $^{\circ}C_b$ (brightness temperature, with respect to W) at the end of extensive emission testing: 3,024 and 9,840 hours, respectively.

Morphological characterization and location-specific chemical analysis of scandate cathode surfaces was performed in a dual-beam focused ion beam and scanning electron microscope (FIB-SEM, FEI Helios NanoLab 660) equipped with an x-ray energy dispersive spectrometer (EDS; Oxford X-Max 80 mm^2 detector). Two lift-out lamellae were extracted from cathode #1 using the FIB and were examined in a transmission electron microscope (TEM; FEI Talos F200X and JEOL JEM-F200 microscopes were used in this study). Along with scanning transmission electron microscope (STEM) imaging for

structural characterization and scanning nanobeam electron diffraction for crystal structure determination, high-resolution elemental mapping was performed on the TEM cross-section lamella using the Super-X EDS system (which includes 4 confocal EDS detectors that simultaneously collect x-rays from the same sample location) in the FEI Talos F200X TEM. Serial sectioning for 3D reconstruction was performed on cathode #2 using the Auto Slice and View technique on the FIB-SEM. Back scattered electron (BSE) micrographs were collected in automated mode by the FIB-SEM, and these were subsequently used for 3D reconstruction of the W crystal shape using Avizo visualization software.

5.3 Results

5.3.1 Surface morphology of scandate cathodes

Images of the surfaces of two scandate cathodes are presented in Fig. 5.1. It is seen in Figs. 5.1(a) and 5.1(c) that the W particle size is ~1 μm and the pores are open, i.e., not obstructed by impregnate material. Two types of particles, each with size on the order of 100 nm, are distributed across the surfaces of W grains: Sc_2O_3 and $BaAl_2O_4$, as determined from EDS point analysis of composition. Complementary and more detailed analysis is also discussed in a related article [50]. Additionally, a critical observation, apparent in Figs. 5.1(b) and 5.1(d), is the highly faceted surface morphology of W grains in both cathodes. Based on Wulff analysis and as discussed in a separate publication [50], these facets correspond to the {100}, {110} and {112} crystallographic planes of W.

The nanoscale particles with diameter on the order of 10 nm, which decorate W facets in a fine dispersion, are assumed to be either Ba or BaO, based on results reported in the literature [50,136]. It appears, however, that numerous Ba/BaO particles were distributed over the W surfaces for cathode #1, while relatively fewer particles were observed on the

surface of cathode #2, as shown in Figs. 5.1(b) and 5.1(d). As discussed in a previous paper [50], these Ba/BaO particles may result from transformation of a metallic Ba monolayer that exists at high temperature but is unstable during cooling after testing; this transformation may occur during cathode cooling after operation, creating the nanoscale particles observed here, and these particles would likely oxidize upon exposure to oxygen. Considering the emission test times, it may be reasonable to observe relatively lower areal density of Ba/BaO particles on the W facets of cathode #2, which had undergone emission testing for 9,840 hours. This is more than three times the duration of testing for cathode #1, which could have resulted in lower (sub-monolayer) Ba coverage on the W surfaces of cathode #2 due to Ba loss during operation, leading to lower density of the Ba/BaO particles.

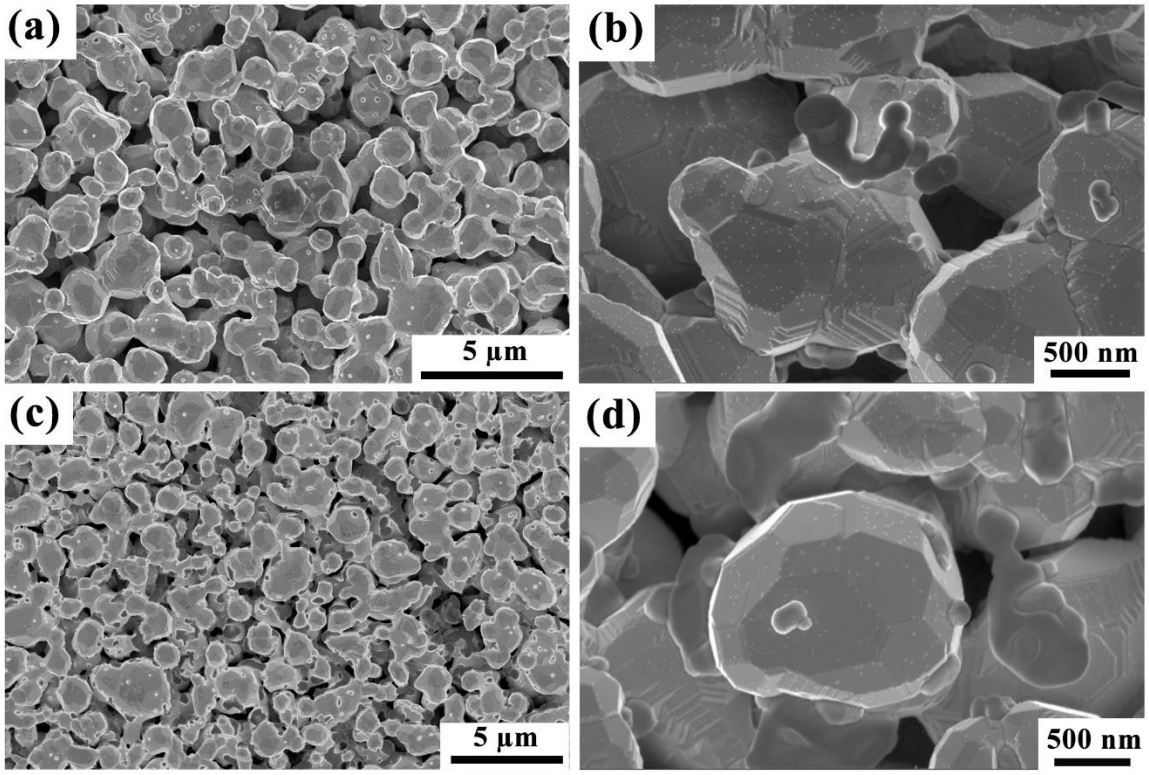

Figure 5.1 Surface morphology of two scandate cathodes. (a) and (b) are low- and high-magnification SEM images of the surface of cathode #1. (c) and (d) are low- and high-magnification SEM micrographs of cathode #2. All micrographs were obtained in secondary electron imaging mode.

5.3.2 Elemental analysis of phases in cross-section samples

High-resolution elemental mapping was performed on a TEM lamella extracted from cathode #1, using the multi-spectrometer EDS system of the FEI Talos F200X TEM. These results are presented in Fig. 5.2, where the images and elemental maps show a cross-section of the cathode that was created during preparation of the TEM lamella. This specimen therefore reveals the structure and composition of the near-surface cathode region, including what is inside the W particles as well as what is on their surfaces and in the pores. The high-angle annular dark field (HAADF) image in Fig. 5.2(a) shows the equiaxed shape of W particles, with flat edges corresponding to different surface facets of a given particle. Pt was deposited on the top cathode surface for protection during subsequent ion milling,

as indicated by the white arrow in this image. Fig. 5.2(b) displays a composite map of composition across the lamella, with different colors corresponding to the major elements of interest, and Figs. 5.2(c)-5.2(h) display elemental maps for W, Sc, Ga, Ba, Al and O, respectively. Comparing Figs. 5.2(d) and 5.2(h), specifically the area marked by the white arrow, it is seen that some compounds attached to the edges of tungsten particles show consistent Sc and O signals during EDS mapping, while certain other Sc-containing compounds located inside tungsten particles (e.g. the row of 4 particles inside the W grain, below the white arrow in Figs. 5.2(d) and 5.2(h)) do not exhibit a noticeable corresponding O signal. In addition to the Sc-containing particles, it was observed in the cross-section maps of Figs. 5.2(f)-5.2(h) that other particles exhibit highly correlated signals of Ba, Al and O. These particles are interpreted to have a mixed Ba-Al oxide phase. The majority of these Ba-Al oxides exhibit only Ba, Al and O signals, e.g., as indicated by the black arrows in Fig. 5.2(a). However, several of the Ba-Al oxides also exhibit simultaneous Sc and O signals. In these cases, the Sc-O appears to be entrapped within the Ba-Al oxides, as indicated by red arrows in Fig. 5.2(b), as well as Figs. 5.2(d), 5.2(f) and 5.2(g). Note that the Sc-O particles are distinct from the Ba-Al oxide particles. In addition, a number of Ba-Al oxide particles are observed to be immediately adjacent to other particles that show Sc and O signals, as marked by white arrows in Fig. 5.2(b), as well as Figs. 5.2(d), 5.2(f) and 5.2 (g). It is noted that a shell of W encases some of the particles seen in the cross-section lift-out specimen, for instance as indicated by the yellow arrow in Fig. 5.2(c), but this is attributed to redeposition of sputtered W from the ion-milling process during fabrication of the TEM lamella. This is also consistent with the Ga map in Fig. 5.2(e), since Ga is present in the redeposited layers.

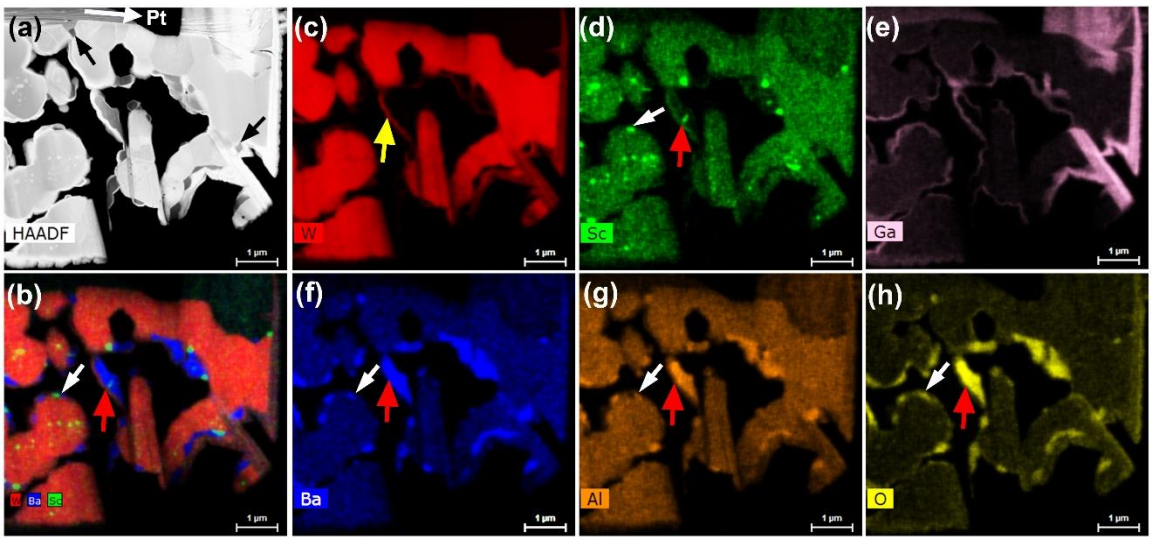

Figure 5.2 EDS elemental mapping of a cross-section TEM lamella from scandate cathode #1. (a) Low-magnification HAADF image of the electron-transparent sample region; (b) composite elemental map showing the distribution of W (red), Ba (blue) and Sc (green) in the TEM lamella; (c)-(h) elemental distribution maps for W, Sc, Ga, Ba, Al and O.

The composition of a Ba-Al oxide particle near the cathode surface (visible as a dark particle at the upper left of Fig. 5.2(b)), was investigated using EDS coupled with EELS. The results are presented in Fig. 5.3. The HAADF image in Fig. 5.3(a) shows the Ba-Al oxide particle located between three W particles and a Pt cap layer (from the FIB lift-out process). EDS measurement of composition was taken from the region marked by the blue box in Fig. 5.3(a), and indicated the following composition: Ba (12.2 at.%), Al (20.7 at.%), O (63.4 at.%), W (0.5 at.%), and C (3.2 at.%). No Sc signal was detected here, i.e. no measurable peak was seen at 4.09 keV on the EDS spectrum acquired in the region outlined by the green box that encompasses the oxide particle. This measured composition provides a reasonable match to the compound $BaAl_2O_4$, albeit with excess O. Moreover, as shown in Fig. 5.3(b), a selected area electron diffraction pattern was obtained from the oxide particle, and it matched the known hexagonal crystal structure of $BaAl_2O_4$. Indexing of this diffraction pattern indicated that it corresponds to a [100] zone axis orientation, and it

matches the theoretical pattern expected for $BaAl_2O_4$ in this orientation. A separate EDS measurement from a neighboring grain, in the region marked by the yellow box of Fig. 3(a), yielded a composition of W (78.5 at.%), Ba (0.1 at.%), Al (0.8 at.%), O (7.3 at.%) and C (13.3 at.%), confirming that the neighboring grain is W. The measured oxygen content of ~7 at.% and carbon content of ~13 at.% in the W area are assumed to arise from surface contamination, which is typical in such samples; it is noted that this would imply the EDS measurement in the blue box region more closely matches the expected stoichiometric composition of $BaAl_2O_4$. Figs. 5.3(c)-3(f) present the elemental maps acquired by EELS in the region outlined by the green box in Fig. 5.3(a). These maps indicate highly correlated signals of O, Al and Ba (but with an absence of W), in agreement with the EDS analysis.

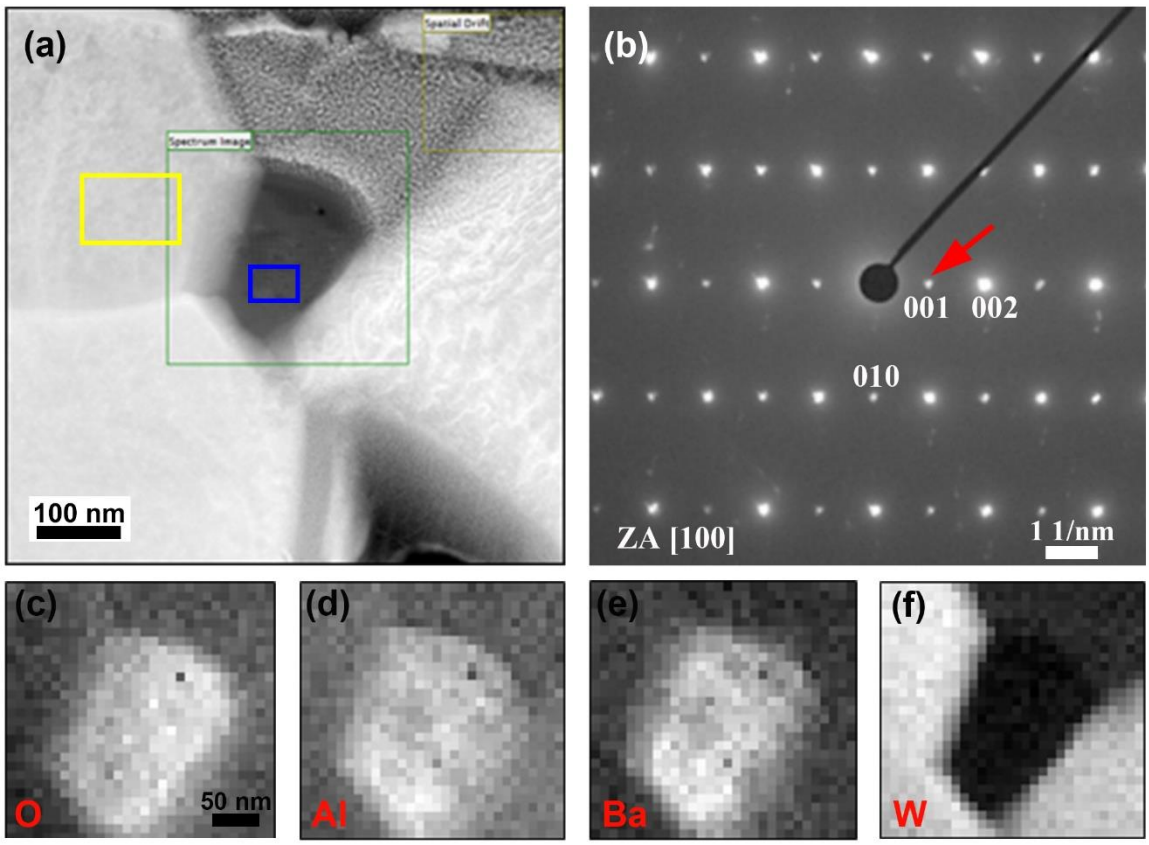

Figure 5.3 Structural and elemental analysis of a Ba-Al-O particle at the cathode surface. (a) HAADF image, with green square showing the area for EELS mapping, as well as blue and yellow boxes showing sites for EDS analysis of the Ba-Al-O particle and neighboring W grain, respectively; (b) selected area diffraction pattern acquired from the Ba-Al-O particle; (c)-(f) EELS elemental maps of O, Al, Ba and W; these four maps share the same scale bar.

To explore the relationship between Ba-Al oxide and embedded Sc-oxide, the region denoted by red arrows in Fig. 5.2 was studied in more detail and these results are presented in Fig. 5.4. The HAADF images, where Fig. 5.4(b) corresponds to the red box in Fig. 5.4(a), shows the morphology of the Ba-Al oxide region, where it is seen that Sc-oxide is surrounded by Ba-Al oxide. Figs. 5.4(c)-5.4(h) are composite and elemental EDS maps showing the distribution of W, Ba, Al, O and Sc. It is noted that the Sc signal is distinct and confined to one particle, as seen in Fig. 5.4(h). EDS measurement of composition in the region outlined by the red box in Fig. 5.4(h) indicates the following: Ba (12.6 at.%), Al

(20.5 at.%), O (56.3 at.%), Sc (10 at.%), W (0.5 at.%), and Ga (0.2 at.%). This suggests that the measured area includes both $BaAl_2O_4$ and Sc_2O_3, which likely exist as distinct but overlapping oxide particles.

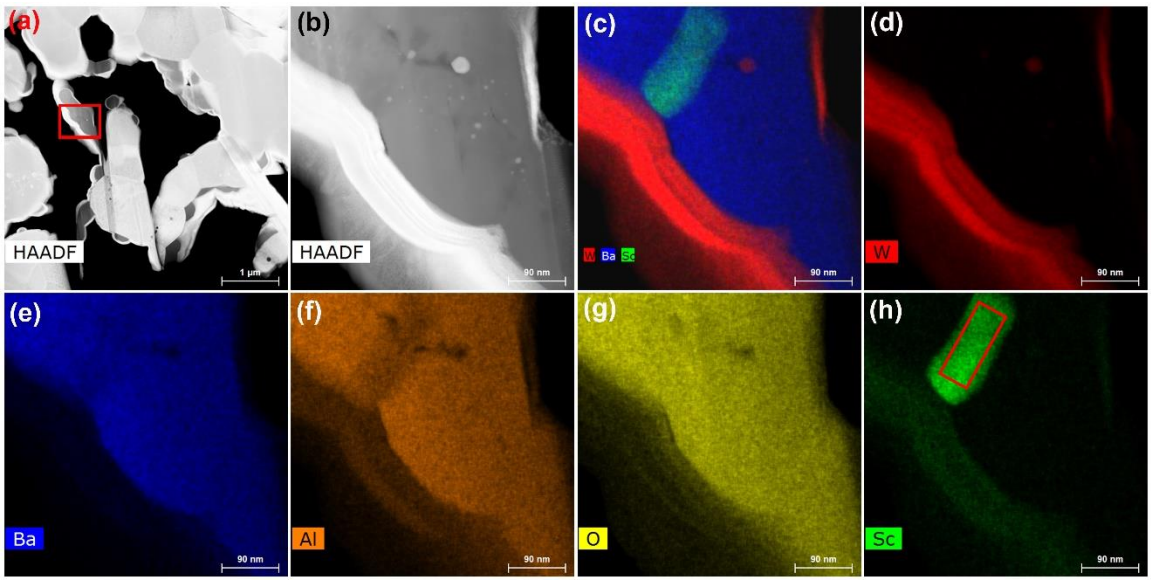

Figure 5.4 EDS elemental analysis of a Ba-Al oxide particle that also exhibits an encased Sc signal. (a) Low-magnification HAADF image of near-surface region of the cathode sample; (b) high- magnification HAADF image showing the area scanned for EDS mapping, which corresponds to the red box in image (a); (c) composite elemental map showing distributions of W, Ba and Sc; (d)-(h) individual elemental maps of W, Ba, Al, O and Sc, where the red box in (h) outlines the region of EDS quantitative measurement.

In order to further investigate the relation between $BaAl_2O_4$ and Sc_2O_3, including possible physical mixing or chemical interactions between the oxides, a small W particle with attached oxides was selected for detailed visualization via a 3D EDS tomogram; this region is indicated by the red box in Fig. 5.5(a). It is noted that this experiment was conducted with a separate TEM lamella than the one imaged in Figs. 5.1-5.4, but both lamellae were cut from cathode #1. The higher magnification image in Fig. 5.5(b) shows a $BaAl_2O_4$ particle atop the larger W particle. 2D slices from the 3D EDS tomogram are presented in Figs. 5.5(c)-5.5(e), showing progressively more elements in each EDS map.

This figure sequence conveys the relative distribution of Ba, Sc and W, and confirms that Sc is distinct from both the W particle and the $BaAl_2O_4$ particle that encases it, i.e. Sc does not appear to be physically or chemically mixed with W or $BaAl_2O_4$. Supplementary Movie 1 shows the 3D tomogram in imaging mode and in EDS mapping mode, and also rotated about the vertical axis, is available in the online Supplemental Files. The EDS composite elemental mapping in this 3D tomography movie corroborates the observations described above and, along with the observations portrayed in Figs. 5.1-5.4, indicates that Sc exists in distinct Sc_2O_3 oxide particles that decorate the surfaces of W grains.

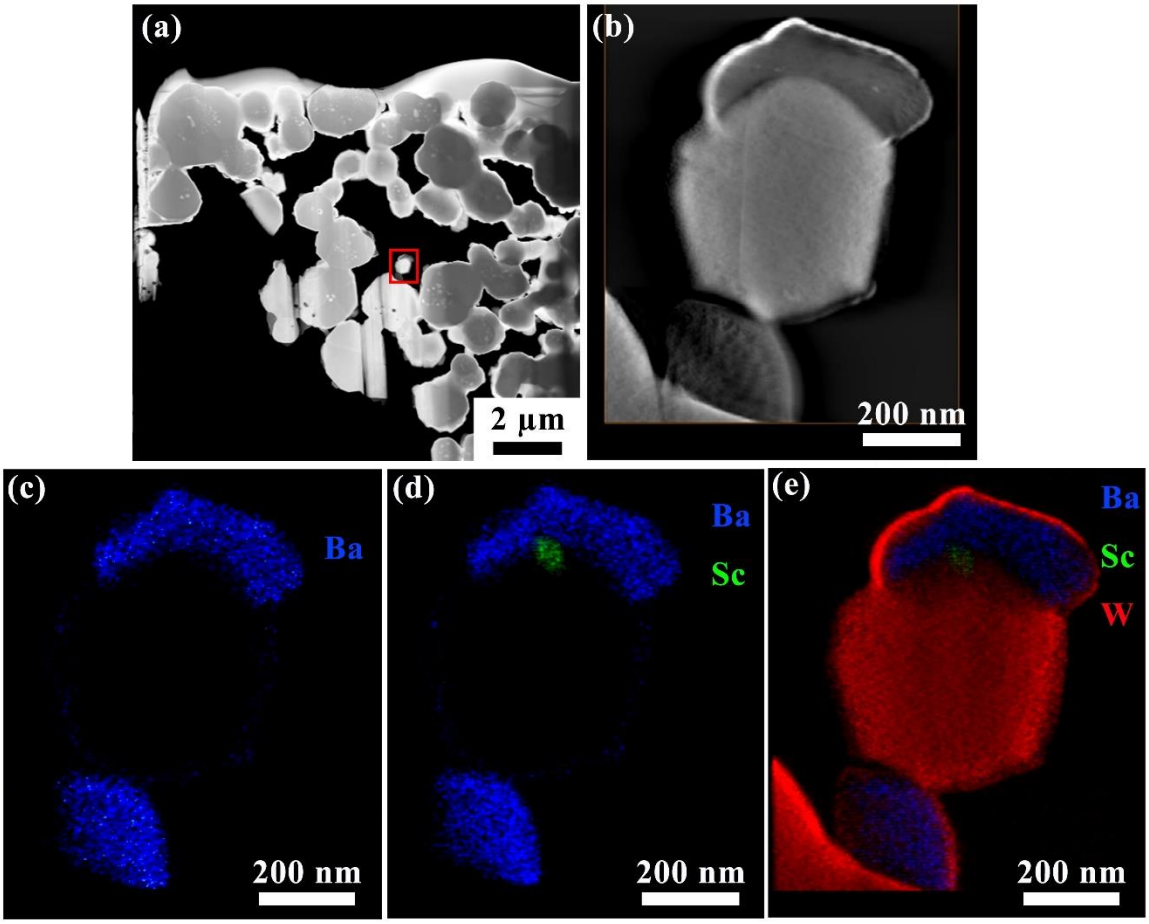

Figure 5.5 (a) HAADF image of near-surface cathode region where structure and elemental distribution were investigated by tomography. (b)-(e) HAADF image and EDS elemental maps, shown as 2D slices from the 3D tomogram, of a Ba-Al oxide particle that encases a smaller Sc-containing particle and sits on a W grain. Sc is distinct from both the W particle and the Ba-Al oxide.

The Ba-Al oxide particle marked by the leftmost white arrow of Fig. 5.2 was characterized at high-magnification, since it was adjacent to a Sc-oxide particle and offered an opportune location for more detailed study of these distinct but adjacent oxides. Fig. 5.6 presents high spatial resolution images and elemental maps of these particles; as seen by comparison of Figs. 5.2(a) and 5.6(a), the TEM lamella has been imaged from the opposite orientation in Fig. 5.6, i.e. the features are reversed left-to-right. The HAADF image of Fig. 5.6(b), corresponding to the red box in Fig. 5.6(a), shows a wide darker gray region that indicates lower average atomic number and therefore suggests the presence of oxide particle(s). The elemental maps of Figs. 5.6(c)-5.6(g) agree with other observations of distinct $BaAl_2O_4$ and Sc_2O_3 particles and, moreover, they show a sharp boundary between Sc and Al. These high spatial resolution EDS maps also revealed a Ca signal, albeit a weak one. Ca may be expected to exist in the tested cathode, as it is intentionally added as part of the impregnate mix during cathode fabrication; however, Ca is not typically detected at significant levels during EDS analysis. However, when it is detected in the near-surface region of an activated and tested scandate cathode, the Ca signal is usually coupled with a Sc signal, as is the case in Fig. 5.6. This may be due to the presence of a mixed Sc-Ca-oxide at certain locations, or remnant CaO (from the impregnate material) situated above/below the Sc_2O_3; however, the low number of such observed particles precludes a definitive statement at this point.

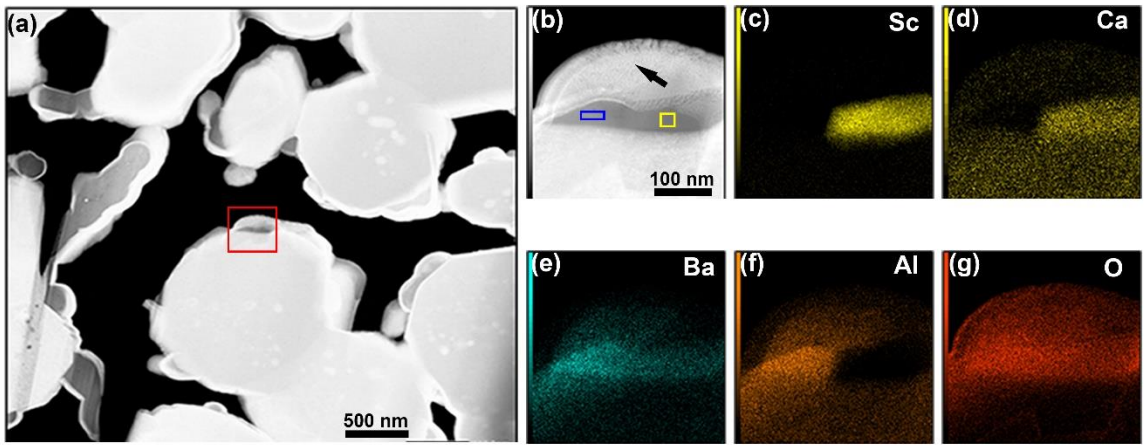

Figure 5.6 High spatial resolution EDS elemental mapping of Ba-Al oxide and adjacent Sc-containing particle. (a) Low-magnification HAADF image; (b) high-magnification HAADF image of area mapped by EDS, corresponding to red box in image (a), blue and yellow boxes denote locations of EDS point analysis; (c)-(g) elemental maps of Sc, Ca, Ba, Al and O. (b)-(g) share the same scale bar.

Quantitative EDS analysis was performed on the Ba-containing and Sc-containing oxide particles in Fig. 5.6, in the regions marked by blue and yellow boxes in Fig. 5.6(b), respectively. These results are presented in Table 1. The region marked by the blue box had a composition (at.%) of Ba(9.3), Al(18.4), O(67.3), W(0.7), C(4.3), which is similar to the result for the oxide particle shown in Fig. 5.3. This region is therefore interpreted to be $BaAl_2O_4$, which agrees with the EDS elemental maps in Fig. 5.6. The region marked by the yellow box had a composition (at.%) of Sc(29.8), Ca(5.2), Ba(3.0), Al(0.2), O(60.7), W(1.1). Again, this agrees with observations described above, except for the presence of Ca. Given the additional presence of a low but not insignificant amount of Ba in the yellow box region, it is proposed that these signals may arise from remnant amounts of CaO and BaO that were added in the impregnate mix. Therefore, the primary oxide particle in the yellow box region would be Sc_2O_3, along with low amounts of CaO and BaO.

Table 5.1 Quantified measurement of particle composition, obtained from EDS point analysis of the regions marked in Fig. 5.6.

EDS site	Measured composition (at.%)	Compound(s) present
Blue box	Ba(9.3), Al(18.4), O(67.3), W(0.7), C(4.3)	$BaAl_2O_4$
Yellow box	Sc(29.8), Ca(5.2), Ba(3.0), Al(0.2), O(60.7), W(1.1)	Sc_2O_3 + minor levels of impregnate materials (CaO and BaO)

In addition to the oxide particles that were observed at the surfaces and edges of W grains, the Sc-containing nanoparticles embedded in the interior regions of larger W particles were investigated using a combination of HAADF imaging and high spatial resolution EDS mapping, as shown in Fig. 5.7. The red box in Fig. 5.7(a) indicates the Sc particle of interest, with a corresponding magnified image in Fig. 5.7(b). The white spots dispersed throughout the Sc particle, as seen in the blue box of Fig. 5.7(b), appear to be spherical in shape, with a diameter in the range of 1-10 nm. The inset image and elemental map in Fig. 5.7(b) reveal that the nanoscale particles dispersed throughout the larger (~100 nm) Sc-containing particle are W. A possible explanation for this curious result is that W dissolves into (or co-precipitates with) Sc_2O_3 during the precipitation stage of the L-S powder fabrication process. This is discussed in more detail below.

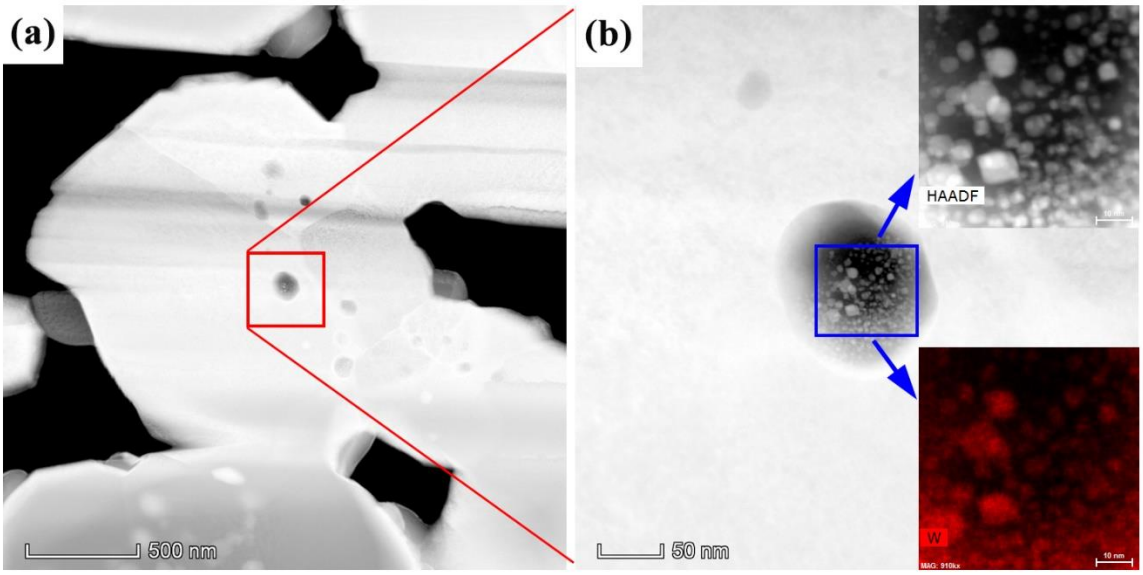

Figure 5.7 High spatial resolution characterization of a Sc-containing particle located in the interior region of a W grain. (a) Low-magnification HAADF image showing the near-surface region of the cathode; (b) zoomed HAADF micrograph corresponding to the red box in (a). Inset in (b) are a HAADF image and W elemental distribution map, revealing nanoscale W particles within the 100 nm Sc-containing particle.

5.3.3 Confirmation of crystal structure of W grains

α-W is the most common phase of tungsten, and it exists in the body centered cubic (BCC) crystal structure. The structure of the W particles that form the cathode body were studied in more detail here. It would be convenient if the structure of W in the cathode body were the same as ubiquitous α-W, but given the complex chemical reactions that take place during preparation and emission testing of a cathode, this may not be true, and therefore the crystal structure was characterized. Scanning nanobeam diffraction was performed on a TEM lamella extracted from cathode #1. In this diffraction experiment, the beam was shifted along a line-scan direction with a step size of 20 nm, from point A to point C in Fig. 5.8(a). Diffraction patterns at three points of interest are displayed in Figs. 5.8(b)-5.8(d), which correspond to sites A, B, and C, respectively. In all cases, the diffraction pattern corresponds to a typical BCC structure oriented along a <111> zone axis. The diffraction patterns obtained at sites B and C are identical. The indexed

diffraction pattern displayed in the lower right corner of Fig. 5.8(d) is representative of all locations characterized in this investigation, confirming that the W grains exist in the BCC crystal structure. In other words, the W matrix has not undergone significant changes due to activation or emission testing. Note that Supplementary Movie 2 portrays the scanning nanobeam diffraction experiment and includes the diffraction patterns recorded at each 20 nm step position.

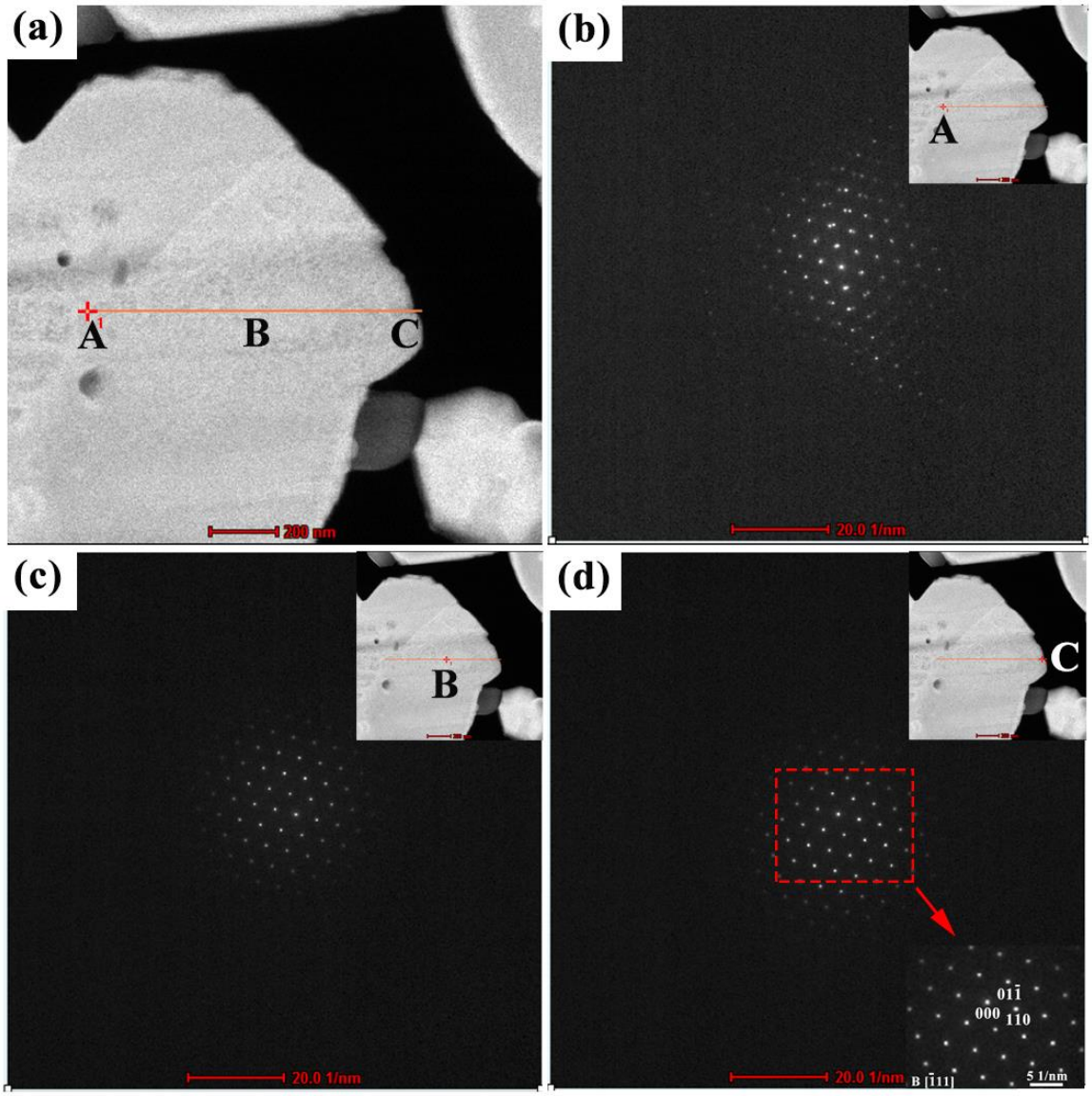

Figure 5.8 Crystal structure of the W matrix in scandate cathode #1, characterized using scanning nanobeam diffraction. It is demonstrated that the W matrix has the BCC structure, which is inferred from diffraction patterns obtained at locations ranging from the middle

of the W grain to its surface. The beam direction and zone axis for the grain orientation shown here are indexed as [-111].

5.3.4 3D tomographic reconstruction

Standard characterization techniques such as SEM, TEM and AFM typically reveal planar, projected or surface information, and therefore may not be ideal for revealing internal microstructure. As such, 3D reconstruction can provide insights into the microstructure of a complex 3D object that is not attainable with 2D characterization [137]. In the current study, a 3D tomogram was constructed for the first time on a scandate cathode, by employing the dual-beam FIB-SEM microscope. This technique involves layer-by-layer milling/removal of thin slices of the sample, using the ion beam, with SEM images recorded after each slice. 10 nm thick slices were milled sequentially, culminating in 137 backscattered electron (BSE) images stitched together to form a 3D tomogram. A schematic of the serial sectioning technique is presented in Fig. 5.9. In order to perform FIB milling, the sample stage is tilted to 52° and the region of interest is situated at the eucentric height, which is where the sample region of interest will not change its vertical position during tilting (it is also where the ion beam and the electron beam converge). Prior to slicing, the sample was coated with a layer of Pt to protect the underlying region of interest. The x-y plane is perpendicular to the ion beam, and the x-z plane (parallel to the ion beam) is imaged after each slice. The red lines in Fig. 5.9 represent the serial sectioning that is performed at regular intervals along the y-axis of the sample.

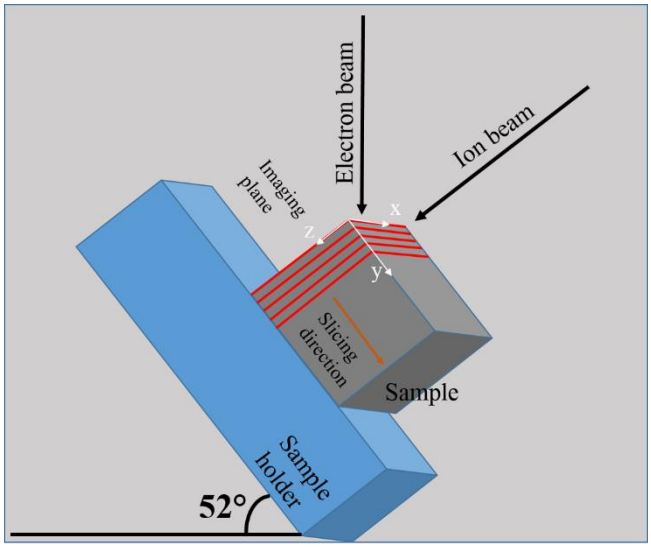

Figure 5.9 Schematic illustration of the sample, ion beam and electron beam for serial sectioning in the FIB-SEM, in order to perform 3D tomographic reconstruction.

The 3D reconstructed shape of a particular W particle was generated using Avizo software, and involved 137 BSE micrographs obtained after each step of automated serial sectioning. This W particle is shown in Fig. 5.10(a) and exhibits surface facets. A noise reduction filter was applied to each micrograph prior to reconstruction. Each image was aligned with respect to a fiducial mark, resulting in the reconstructed tomogram displayed in Fig. 5.10(b). The SEM image of the selected W particle in Fig. 5.10(a) and the 3D reconstruction of that particle in Fig. 5.10(b) agree well with each other, and the surface facets are consistent and clear in both figures. The linear surface steps in Fig. 5.10(b) result from the serial slicing process, specifically from slight misalignments between image positions after each slice, i.e. these surface steps are an artifact of reconstruction. Since BSE imaging was used to generate the tomogram, it was possible to optimize atomic number contrast for setting thresholds in the reconstruction. The metallic W regions exhibited consistent brightness levels, while the oxide particles were darker gray and clearly distinguishable from the main W particle. Leveraging this contrast, the (darker)

oxide particles were differentiated, and Fig. 5.10(c) reveals Sc/Sc_2O_3 particles trapped inside the larger W particle. As shown in Supplementary Movie 3, where the tomogram of Fig. 5.10(c) is rotated and viewed from multiple directions, the smaller oxide particles can be seen to lie inside the W particle. These observations are consistent with the results described earlier, namely that Sc/Sc_2O_3 particles are contained inside larger W grains.

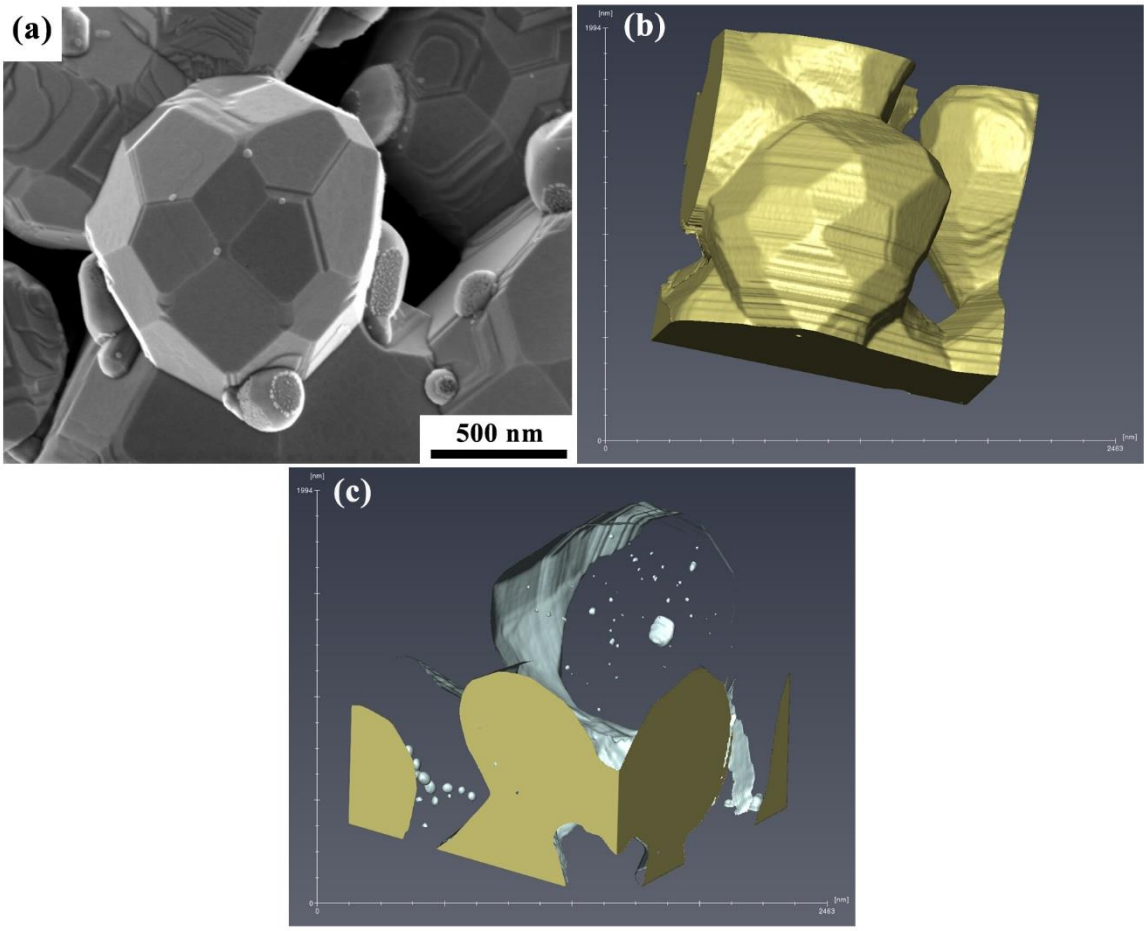

Figure 5.10 3D reconstruction of a W particle from scandate cathode #2, generated by FIB serial sectioning and imaging in the SEM. (a) Secondary electron SEM micrograph of the selected W particle, (b) reconstructed tomogram, and (c) spatial distribution of Sc/Sc_2O_3 inside the W particle. Note that the viewing direction of image (c) is rotated with respect to that of images (a) and (b).

To further investigate the source of the Sc_2O_3 particles that were observed inside the W grains of the cathode pellet, the starting materials were characterized. This included pure

W powder, as well as Sc_2O_3-doped W powder that had been processed from the same W powder using the L-S technique. Fig. 5.11 presents SEM micrographs of each powder set, showing particle morphology and distribution. As seen in Fig. 5.11(a), the W particles have clean, flat surface facets prior to the L-S processing step. However, after the L-S stage, W surfaces are decorated with Sc_2O_3 particles and W exhibits microfacets at the intersections of neighboring facets. These microfacets may result from etching of W. Additionally, there are numerous cavities that appear to have been etched into the W grains, following by backfilling of these cavities with Sc_2O_3 particles. An example of this is shown in the central region of Fig. 5.11(b). Thus, the L-S processing step allows Sc_2O_3 to penetrate the W grains, which later form seemingly regular, faceted W grains during high-temperature activation and emission testing stages. In this way, the Sc_2O_3 particles become trapped within W, resulting in the microstructural features that were described above.

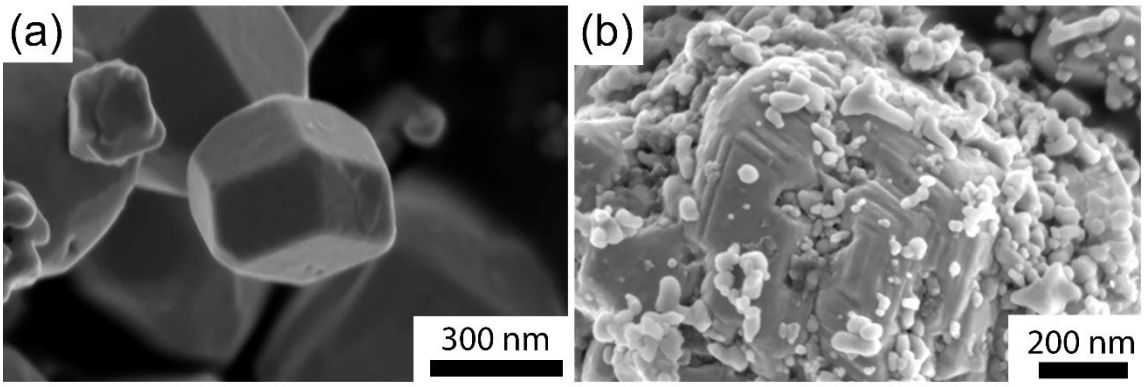

Figure 5.11 SEM micrographs of (a) tungsten powder and (b) scandia-doped tungsten powder. Both images were recorded in secondary electron imaging mode.

5.4 Discussion

Since the primary materials difference between scandate cathodes and conventional impregnated tungsten cathodes is the addition of scandia to the W matrix, it is reasonable to assume that scandia (or scandium) is responsible for the significant improvement in

thermionic emission and the low work function of scandate cathodes. However, the exact role of Sc/Sc_2O_3 in cathode processing and/or performance remains unclear. Uda *et al*. [61] suggested it is impossible for Sc_2O_3 to migrate from interior regions of the porous W matrix to the cathode surface during activation, due to the low diffusion coefficient (1.6×10^{-18} cm^2/s at 1370K). Therefore, in order for Sc to diffuse or migrate to the cathode surface within a reasonable timeframe, Sc_2O_3 would need to be transformed into metallic Sc, as proposed by Wang [44] and Liu [78]. However, the reaction(s) required to generate free Sc and the mechanism of Sc migration have not been experimentally verified, despite these research efforts. In this section, chemical reactions that may enable the creation of metallic Sc are discussed, as are Sc-containing compounds that may be relevant to the role of Sc in scandate cathodes.

Sc has a stronger affinity for O than does Ba, which means that Ba cannot reduce Sc_2O_3 to Sc directly [124]. In a cathode study by Yamamoto *et al*. [8], it was proposed that metallic Sc can be produced via a chemical reaction between $Sc_2W_3O_{12}$ and Ba, as described in equation 1, which was based on their work on (W-Sc_2O_3)-coated [67] and (W-$Sc_2W_3O_{12}$)-coated impregnated cathodes [8].

$$Sc_2W_3O_{12} + 3Ba = 3BaWO_4 + 2Sc \quad 5.1$$

In that reaction scenario, metallic Ba was created by impregnate materials reacting with W at pore walls, similar to the case for regular impregnated tungsten cathodes. Multi-step chemical reactions that generate Ba were described by Jones [130] as:

$$5BaO + 2Al_2O_3 = 3/2\ Ba_3Al_2O_6 + ½\ BaAl_2O_4 \quad 5.2$$

$$2Ba_3Al_2O_6(s) + W(s) = BaWO_4(s) + 2BaAl_2O_4(s) + 3Ba(g) \quad 5.3$$

According to these reactions, the production of free metallic Ba is accompanied by generation of the compound $BaAl_2O_4$. As demonstrated by Rittner [28], this compound can be regarded as an inert material, i.e. it is thermally stable and does not participate in thermionic electron emission from the cathode surface. Since reactions (2) and (3) take place at W pore walls, i.e. the surfaces of W grains, it is reasonable to observe $BaAl_2O_4$ particles at W surfaces and junctions in cathode cross-section samples, as was shown for example in Fig. 5.3.

As described by Yamamoto [8], the compound $Sc_2W_3O_{12}$, which can result from oxidation during heat treatment of W-Sc_2O_3, is the most likely source of metallic Sc and would be produced according to reaction (1) above. However, $Sc_2W_3O_{12}$ is not observed in the cathode samples described in the current paper, and this may be due to complete reaction of the compound $Sc_2W_3O_{12}$. By virtue of their nanoscale size and uniform distribution across W surfaces, the Sc_2O_3 nanoparticles fabricated during L-S processing in the current study may react more readily with W, and thereby enhance the formation of $Sc_2W_3O_{12}$. If these mixed-oxide particles are also sufficiently small and uniformly distributed over W pore walls, this would facilitate the creation of free metallic Sc throughout the porous network.

Additionally, according to Slooten [138], the rate of Sc supply is significant only in the initial hours of cathode operation. After this transient stage, the generation of metallic Sc decreases to an undetectable level due to the formation of stable compounds such as $Ba_3Sc_4O_9$ or Ba_2ScAlO_5, which inhibit electron emission. However, these phases were not observed during the characterization work in the current study. Future efforts will include a more detailed study of Sc-containing compounds in scandate cathodes.

The exact role of Sc in scandate cathode processing and performance remains elusive, although there is now an improved understanding of the various phases in the near-surface regions of scandate cathodes. Other studies in the scientific literature ascribe the enhanced emission capability and low work function of scandate cathodes to a Ba-Sc-O monolayer [60,93] or a relatively thick (~100 nm) Ba-Sc-O layer [9,24,78] that covers W grains at the cathode surface. However, as was described in a recent paper from the current authors' group [50,101], no Ba-Sc-O layer with thickness on the order of 10-100 nm was observed, despite using several pertinent and complementary techniques in the characterization of multiple scandate cathodes that had yielded good emission test results. Finally, as suggested by Hasker [60] and Zhou [101], one possible function of Sc is to regulate the chemical potential of oxygen on the emitting surface of a scandate cathode, since the affinity of O for Sc is greater than it is for Ba.

5.5 Conclusions

Multiple scandate cathodes were prepared using the liquid-solid fabrication method and were subjected to CSD emission testing. Subsequently, they were characterized using multiple advanced microscopy techniques, including (S)TEM imaging, high spatial resolution EDS mapping, EELS analysis, scanning nanobeam diffraction, and 3D reconstruction/tomography. The experimental observations and discussion above are summarized with these concluding remarks:

(1) There are fewer Ba/BaO dots on the surface of cathode #2 than on cathode #1, which may be due to the longer emission testing time for cathode #2. Ba/BaO may be consumed to a greater degree if the cathode is subjected to longer emission testing, resulting in fewer Ba/BaO dots on the cathode surface.

(2) The majority of particles that are attached to the surfaces and edges of W grains are $BaAl_2O_4$, as revealed during characterization of scandate cathode cross-section samples. In some cases, $BaAl_2O_4$ particles are contiguous with Sc_2O_3 particles and/or envelop Sc_2O_3 particles.

(3) No evidence for chemical interaction or mixing between $BaAl_2O_4$ and Sc_2O_3 was observed, i.e. these oxide particles appear to remain distinct.

(4) Scanning nanobeam electron diffraction in the TEM showed that the crystal structure of W grains remains body-centered cubic in emission-tested scandate cathodes. The crystal structure and lattice constant of W particles have not changed as a result of the complex chemical reactions that occur during cathode fabrication, nor during activation or emission testing.

(5) 3D tomographic reconstruction revealed the interior microstructure of W grains in a scandate cathode. Interestingly, nanoscale Sc/Sc_2O_3 particles tend to cluster or align in certain regions of a given W grain, rather than being distributed uniformly throughout the W grain. This may be due to infiltration of Sc_2O_3 particles into W during the L-S processing stage, and subsequent entrapment of Sc/Sc_2O_3 within larger W grains during high-temperature processing and activation.

CHAPTER 6. STUDYING ON L-L SCANDATE CATHODES: PROBING THE BA-SC-O SURFACE LAYER AND 3D TOMOGRAPHY

6.1 Introduction

Recently scandate cathodes, also known as barium impregnated cathodes (B type cathodes) with the additive of scandia, have attracted significant attention due to significantly enhanced current density [6,10,44,73]. Scandate cathodes have been developed with various configurations, i.e., top-layer scandate cathode [60,61], pressed scandate cathode [58,59,65] and impregnated cathodes [9,23,44,73,139]. As reported, one top-layer scandate cathode even achieved high current density of 400 A/cm^2 at the temperature of 965 $^{\circ}C_b$ [53]. Among them, the impregnated scandate cathodes are, however, the most promising thermionic cathodes and have received extensive attention as they are relatively simpler for production and can deliver high current density as well.

Unlike the B type cathodes where the Ba-O dipole model has been well understood and accepted [69], the operation mechanism of scandate cathodes remains indistinct [93]. Various models were proposed as reflected from previously published articles. Two of them- Ba-Sc-O monolayer and thick (100 nm) Ba-Sc-O surface layer- have been widely discussed. More specifically, Yamamoto and Taguchi [8] claimed that Ba-Sc-O monolayer on cathode emitting surface yields copious emissions and, moreover, that the free Sc participating in formation of the surface layer was reduced by Ba from $Sc_2(WO_4)_3$. Hasker et al [60] hold the identical viewpoint that a Sc, Ba and O coverage of monolayer order is responsible for the exceptional emission capability of scandate cathodes. In addition, they hypothesized that the role of Sc is regulating surface oxygen concentration for approaching optimum O concentration on the emitting surface. However, in most recent two decades,

Wang et al [9,24,44,75,78] attributed the emission enhancement of scandate cathodes to a thick (100 nm) Ba-Sc-O layer on tungsten surface. It should be noted, however, that thickness-measurement of the thick Ba-Sc-O layer was derived from depth profile analysis using the regular auger electron spectrometry (AES) where effects of etching rate calibration and re-deposition are difficult to be completely avoided. Calibration of etching rate directly affects thickness evaluation and, in addition, re-deposition along with the etching process cannot be avoided and can influence thickness measurements as well. Apart from models of focusing on Ba-Sc-O surface layers, some other possible mechanisms are of course worthy of mention. Kordesch et al [140–142] suggested that vertically stacked Ba-Sc-O on W was unlikely; instead, a side by side located Sc and Ba on W was of higher possibility to govern electron emission. Similarly, as indicated by Forman and Lesny [46], the best electron emission yields were from sites where barium and oxygen were on top of scandium oxides.

As illustrated in our preceding papers [15,50,114], no thick (100 nm) Ba-Sc-O surface layer was observed through comprehensive (S)TEM examination. In this paper, attempts are made to explore the thin Ba-Sc-O layer on scandate cathodes surface and study the near-surface phases and nanostructures of scandate cathode made from L-L powders. The results provide evidence for identifying chemicals on scandate cathodes surfaces and are helpful for gaining a better understanding of the operation mechanism of scandate cathodes.

6.2 Materials and Methods

Two Scandate cathodes studied in this report were prepared by e beam inc., and developed with scandia doped tungsten powder that synthesized from liquid-liquid (L-L)

technique. Accordingly these two cathodes are L-L scandate cathodes, more specifically, one is the cathode#1 taken from the test vehicle of D0107 and the other is the cathode#4 taken from the test tube of N3907. In this paper the two L-L scandate cathodes aer noted as cathode #1 and cathode #2. In addition, the two scandate cathodes have been tested for 6768 hours and 9840 hours in separate close space diodes (CSD), respectively, prior to the performance of materials characterization.

Disparate to the technique of solid-liquid (L-S) which is a single precipitation process, the L-L approach is a co-precipitation process. Firstly, scandia and tungsten were dissolved into solutions separately. The two resulting solutions were then mixed together followed by being placed in a warming oven. Subsequently, precipitated drops that appear at the bottom of the container were extracted and then fired in a hydrogen atmosphere. As a result, scandia doped tungsten powder with a highly homogeneous distribution of scandia was produced which was then pressed and sintered to a pellet. Prior to the emission testing in CSD, the pellet was impregnated by barium-calcium-aluminates and then activated at the proper temperature.

Emission tests of scandate cathodes were performed at e beam incorporated. Surface morphological observation was carried out using a dual-beam FIB-SEM (Helios Nanolab 660) under the immersion mode. Chemical composition of phases on the cathodes' surfaces was measured through X-ray energy dispersive spectroscopy (EDS, Oxford X-max EDS detector) that was attached to the FIB-SEM. The lamella made for TEM observation was extracted from the cathode #2 with FIB and examined by the TEM (Taolos F200X). EELS spectrum and chemical maps were acquired using a dual-detector apparatus located within

the TEM (Taolos F200X). Nano-AES analysis was performed at the Lawrence Berkeley National Lab.

6.3 Results

6.3.1 Surface morphologies of L-L scandate cathodes

Two sets of back-scattered electron images that show surface morphology and elemental contrast information of cathode #1 and #2 are presented in Fig. 6.1. It can be seen from Figs. 6.1(a) and 1(b) that tungsten grains of cathode #1 are the size of approximately 1 μm and are highly faceted. Pores among tungsten grains are significantly obstructed by a material of a grey contrast (as shown by black arrow in Fig. 1b), indicating that this material has a lower atomic number than that of tungsten. In addition, a few dispersed smaller particles with a darker contrast can be discovered on either the tungsten surface or the surface of the grey colored stuff-material, as marked by the red arrow in Fig. 6.1 (b). Apart from that, numerous superfine nanoparticles on the order of 10 m can be barely seen on the tungsten surface. These are identified to be BaO dots as illustrated in our preceding papers [79,143]. Chemical composition of the surface decorating particles is studied through the technique of EDS. It turns out that the grey-color particles are Ba-Al oxide ($BaAl_2O_4$) and the dark-color nanoparticles are Sc_2O_3. These surface decorating particles are similar to that on L-S scandate cathode of outstanding electron emission. But it should noted that for well emitted L-S scandate cathode the pores between tungsten grains are unclogged and the decorating particles are primarily sticking to tungsten surfaces rather than filling the pores.

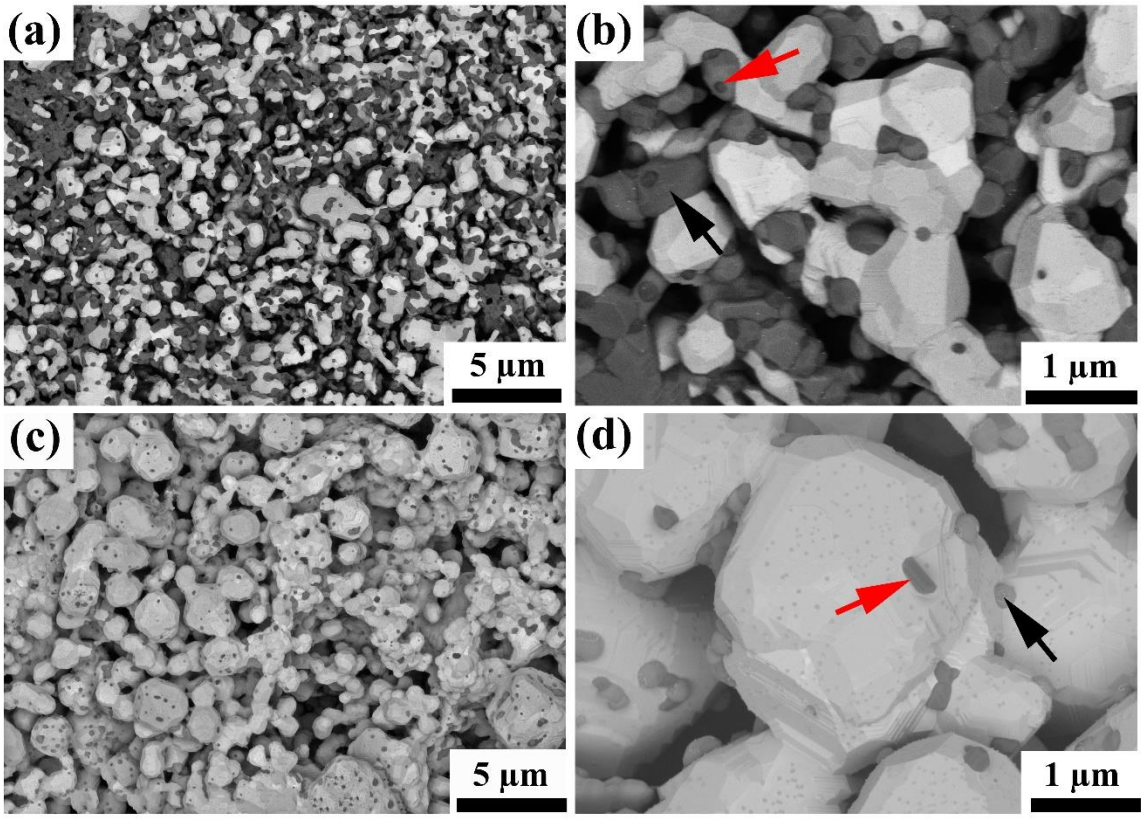

Figure 6.1 Back-scattered electron micrographs of scandate cathodes. Images are acquired with a FIB-SEM under the immersion mode. (a) and (b) from the cathode #1, (c) and (d) from the cathode #2.

Figs. 6.1 (c) and (d) display surface features of the scandate cathode #2. Similarly, tungsten particles are highly faceted and decorated by particles with various elemental contrast. However, pores between tungsten grains are unclogged for the scandate cathode #2. Analogous to the cathode #1, nanoparticles with grey contrast, dark contrast and superfine BaO dots can be observed either on sintering-neck locations or over tungsten surfaces. Similarly as illustrated by EDS analyses, the grey-color nanoparticle is Ba-Al oxide ($BaAl_2O_4$) and the dark colored nanoparticles are Sc_2O_3 which is identical to the case of cathode #1. Note that the density of surface decorating particles for cathode #2 is

remarkably smaller than that of cathode # 1 which may due to its significantly longer testing hours under high temperature (~ 850 $^{\circ}C_b$).

Analogous to what we did in chapter 4, Wulff-construction was used to determine the facets of tungsten particles in the L-L scandate cathodes, as presented in Fig. 6.2. For the sake of comparison one pair of SEM secondary electron images from a well-emitted L-S scandate cathode are put in Figs. 6.2 a and b while Figs. 6.2 c and d are two SEM micrographs acquired from the L-L scandate cathode #2. The insets are Wulff constructed crystal shape which have been tiled to mimic the corresponding SEM images.

It's found that for both the L-S and L-L scandate cathodes, the facets are identified to be {100}, {110} and {112} with a given normalized surface energy of 1.00:1.08:1.02 during the Wulff analysis. Also the {112} facets are dominant because they cover 69% of the total surface area with respect to the sum surface area of tungsten grains.

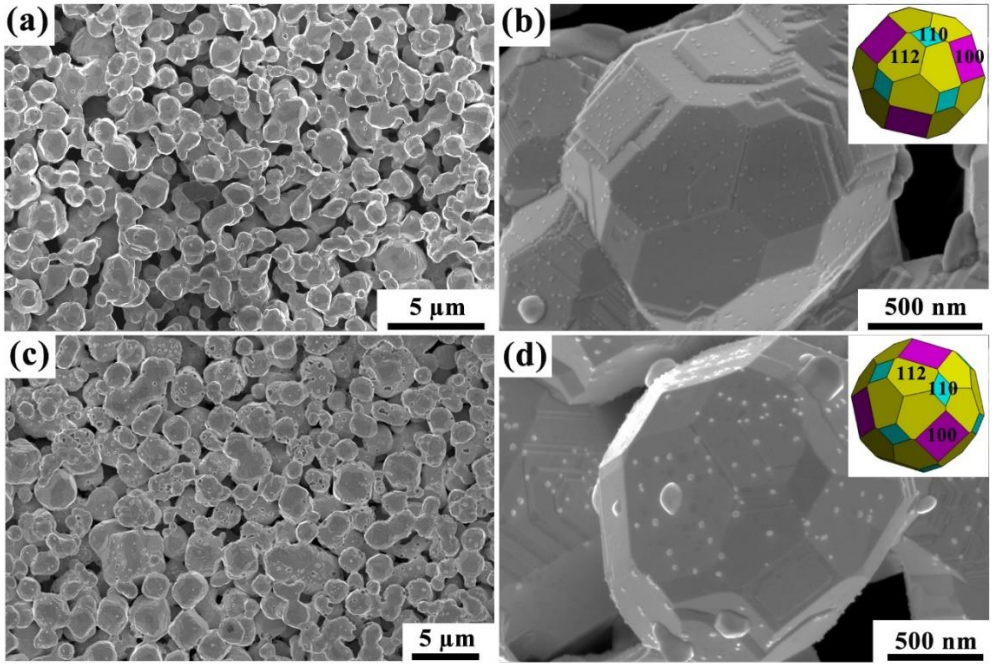

Figure 6.2 SEM images of scandate cathodes. (a), (b) a pair of SEM images from a L-S scandate cathode, (c), (d) are from a L-L scandate cathode #2. The insets in (b) and (d) are the corresponding Wulff shapes.

6.3.2 Emission performance of L-L scandate cathodes

L-L scandate cathodes #1 and #2 were assembled and tested in separate standard close space diodes for 6768 and 9840 hours, respectively. Current density as a function of brightness temperature (W) of the two cathodes are plotted, as displayed in Fig. 6.3. As can be seen, the knee points, defined by interception of extrapolations of space-charge-limited (SCL) line and temperature-limited (TL) line, of cathode #1 and cathode #2 are 860 $^{\circ}C_b$ and 831 $^{\circ}C_b$, individually. Low knee temperature implies excellent electron emission capabilities of these two scandate cathodes [10].

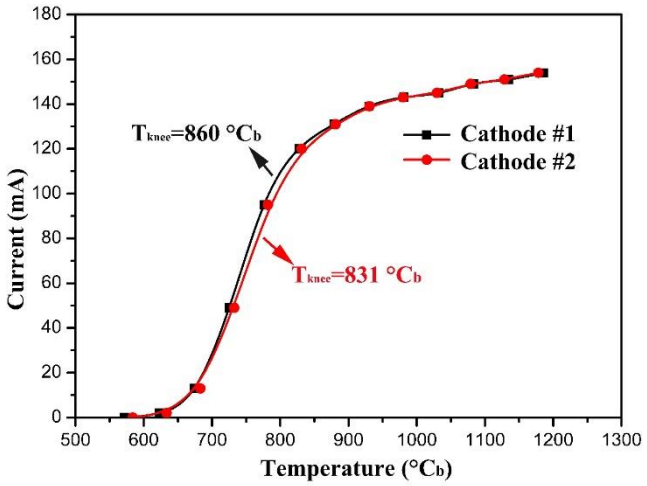

Figure 6.3 Plots of current versus brightness temperature (W).

6.3.3 Probing the Ba-Sc-O surface layer

For normal EDS, high voltage for generating sufficient characteristic x-rays is required which inevitably leads to a large interaction volume. As a result it is unbeneficial for analyzing the elements on the very surface of a given sample. Take scandate cathodes as an example: characteristic X-rays generated form the W-matrix can easily shade the signals coming from the surface elements, i.e., Sc, Ba and O during EDS analysis. Nano-

AES, however, employs a much lower excitation voltage (around 5 kV) and uses a highly focused electron beam (approximately 5 nm in spot size) as the primary beam and hence is capable of providing much higher spatial resolution.

To study elemental distribution on the surface of a scandate cathode, cathode #1 was examined by Nano-AES as exhibited in Fig. 6.4. One typical faceted tungsten grain that decorates with various particles was chosen for acquiring AES chemical maps. From Figs. 6.4(a), (c), (e) and (g), it can be seen that the mean SEM images of Sc, Ba, O and W show uniform contrast of each element which means that all these elements distributed homogeneously throughout the surface of the tungsten grain. In addition, as displayed in figs. 3(b), 3(d) and 3(f), it is evident that distributions of Sc, Ba, O and W are uniform excluding the sites of Ba-O rich or Sc-O rich surface decorating particles. Note that fractional contrast across elemental maps should not be considered while talking about distribution homogeneity of an individual element. However, from the perspective of quantitative evaluation, the overall fraction of Ba is appreciably lower than that of Sc as demonstrated by Figs. 6.4 (b) and (d). The possible reason is that Ba keeps dispensing and consuming while Sc is much more stable during the emission testing which lasted as long as 6768 hours.

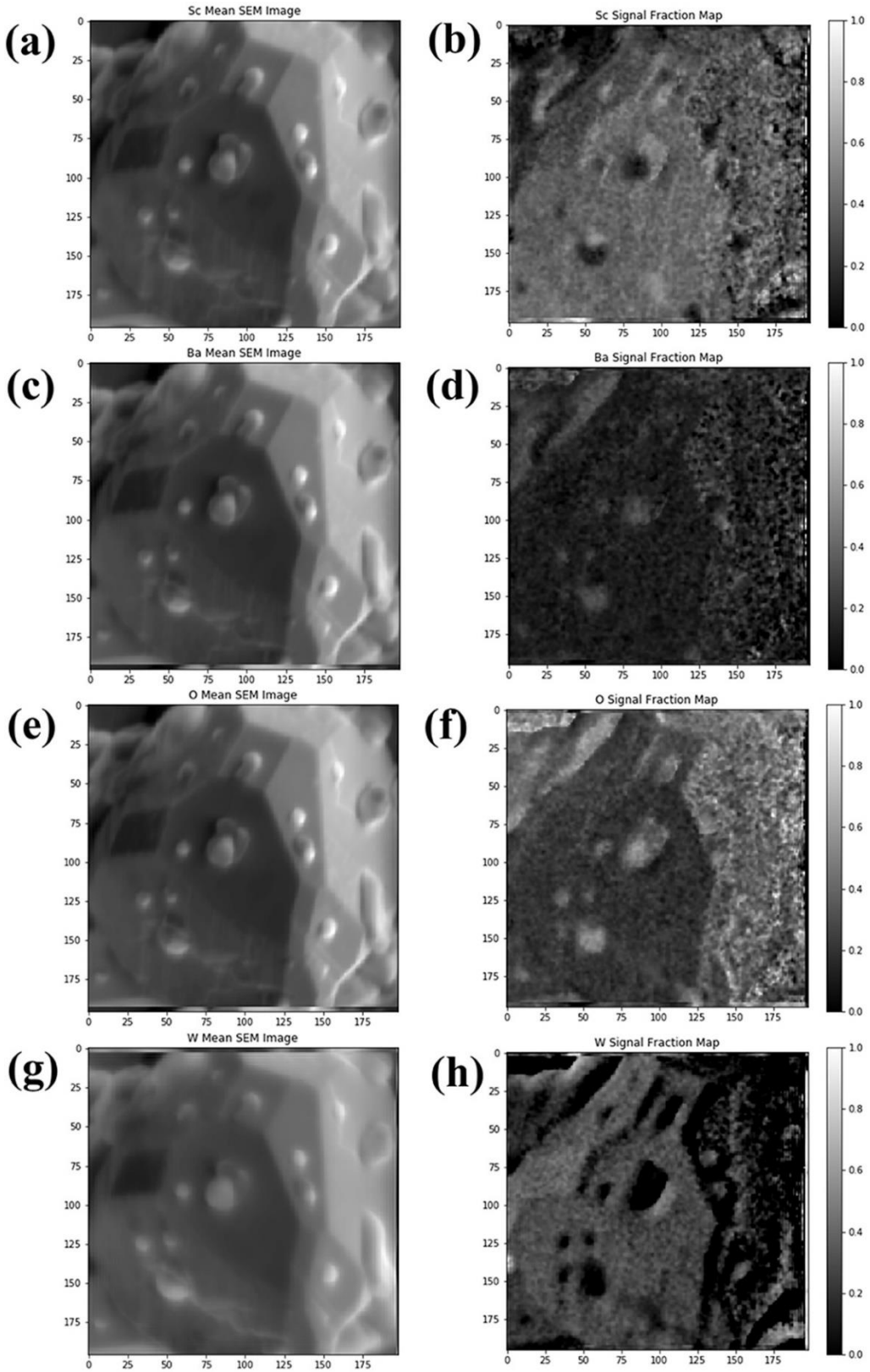

Figure 6.4 Nano-AES analysis on surface elemental distribution scandate cathode #1.

Furthermore, to explore the Ba-Sc-O surface layer one lamella was cut from cathode #2 and subsequently examined by TEM, as shown in Fig. 6.5. The STEM high angle annular dark field (HAADF) image in Fig. 6.5 (a) exhibits that a very thin layer (grey contrast) continuously covers the tungsten crystalline (white contrast). EELS chemical maps were collected at the boxed area in Fig. 6.5 (a) as displayed in Figs. 6.5 (b)-(e) with associated electron energy loss spectrum in Fig. 6.5 (e). It appears that signals of Sc, O and Ba show great agreement which means that the surface layer comprises these three elements. Additionally, it was determined that the thickness of the Ba-Sc-O surface layer is approximately 8.5 nm which is significantly thinner than the thick layer (100 nm) as claimed by Wang et al. Note that the Ba-Sc-O surface layer is slightly thicker at the sunken site where two facets meet; it may suggest that boundaries are favorable for formation and growth of the surface layer.

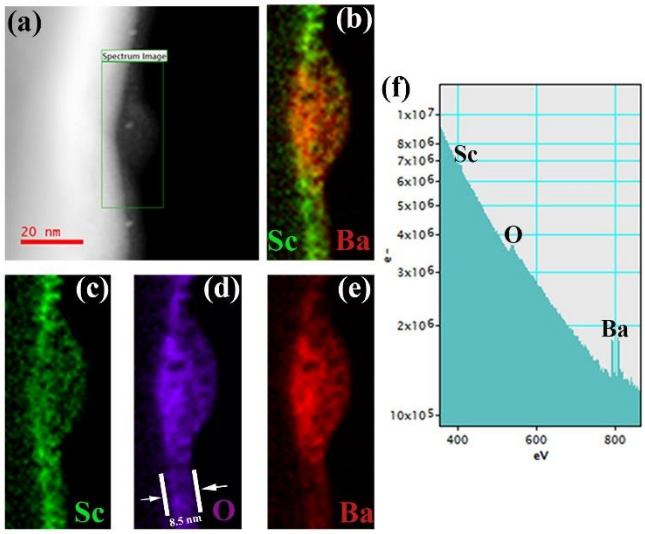

Figure 6.5 EELS chemical maps and corresponding electron energy loss spectrum. (a) HAADF image, green box inside indicates the area for EELS analysis; (b) layered chemical map showing Sc and Ba; (c), (d) and (e) maps of Sc, O and Ba; (f) electron energy loss spectrum.

To investigate the crystal structure of the Ba-Sc-O surface layer, nano-beam diffraction (NBD) was conducted, as presented in Fig. 6.6. The STEM image in Fig. 6.6 (a) shows an incomplete boundary of a W grain which is at the same site for the EELS maps acquirement in Fig. 6.5. Nano-beam diffraction was carried out by shifting the electron beam along the yellow solid line (from right to left) in Fig. 6.6 (a). As the electron beam progresses, the diffraction patterns alter significantly. Four typical sites that correspond to the pore-site, blurred starting layer, surface layer zone and the W body are marked as B-E in image Fig. 6.6 (a) and the corresponding diffraction patterns are exhibited in Fig. 6.6 (b)-(e), individually. At the pore-site (B), only the central transmitted spot arose as shown in Fig. 6.6 (b). While the diffraction pattern in Fig. 6.6 (c) shows a halo-shape with obscure concentric circle(s) implying the "very thin" blurred layer is more likely amorphous materials. This may result from the Ga^+ bombardment during the milling process for the TEM lamella preparation. At the site D, which refers to the Ba-Sc-O surface layer zone, apparently the diffraction pattern (Fig. 6.6 d) exhibits multiple concentric circles , implying that the surface layer constitutes of polycrystalline materials. Moreover, considering the step size during the nano-electron-beam scanning is a few nanometers, it is reasonable to infer that the size of the polycrystalline materials is of nanoscale. With the electron beam scanning into the W body, the diffraction pattern (Fig. 6.6 e) matches to a typical BCC structure oriented along a <132> zone axis.

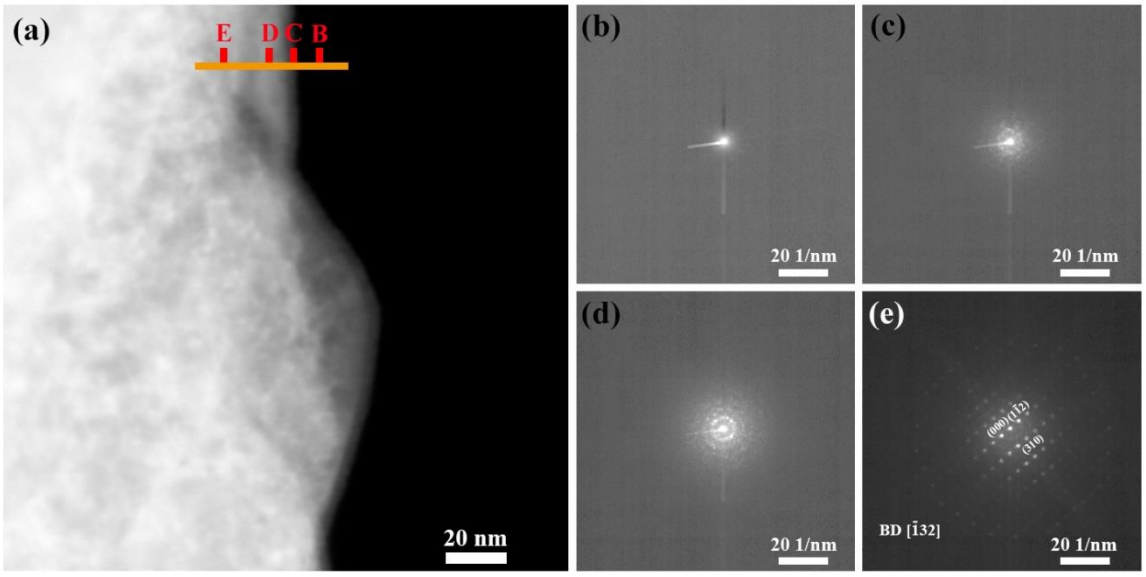

Figure 6.6 Nano-beam diffraction study on crystal structure of the Ba-Sc-O surface layer. (a) STEM image of a partial tungsten grain with the surface layer; (b)-(e) diffraction patterns correspond to the sites of B-E as indicated in image (a).

6.3.4 TKD and TEM tomography

As introduced in chapter 3, TKD has a higher spatial resolution than normal EBSD since for TKD the sample (electron-transparent lamella) is place along a vertical direction to the electron beam. As a result, the electron beam remains focused rather than being spread as in the case of regular EBSD and therefore has a significantly better resolution [11,144]. One lamella was lift-out and thinned from cathode #2 (L-L scandate cathode) to do the TKD test for studying the phases on cross section of the scandate cathode sample. The results are presents in Fig. 6.7, the image (a) displays the selected area for acquiring the phase map and which shows the tungsten grain and the oxide particle (at the center of the image). Fig. 6.7 (b) shows the inverse pole figure in which color indicates crystallographic orientation. It can be seen that the tungsten gains are presenting various crystallographic orientation, moreover, the oxide comprises several smaller grains and also

of different orientation. A phase map was acquired simultaneously as present in Fig. 6.7 (c) from which the oxide is determined to be $BaAl_2O_4$. It should be noted no Ba_2ScAlO_5 as claimed by Liu and Wang et al [64] was discovered as revealed by the phase map.

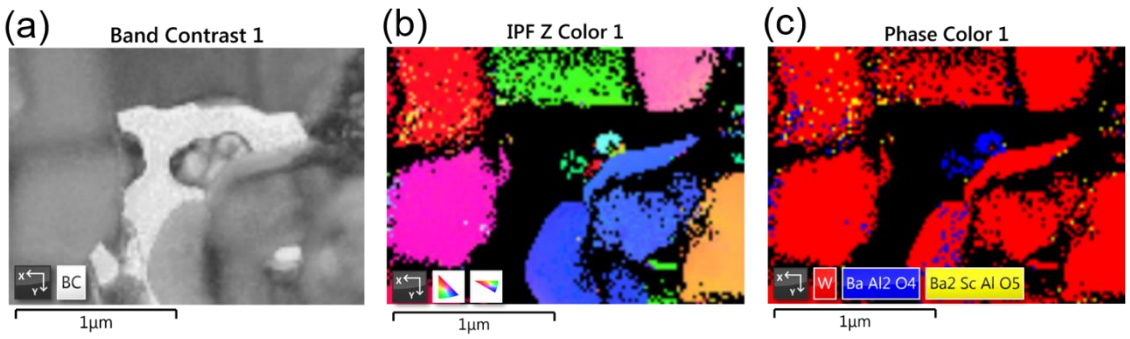

Figure 6.7 TKD results on a lamella extracted from L-L scandate cathode #2. (a) Forescatter diodes (FSD) image, (b) inverse pole figure and (c) phase map.

Another lamella was cut from the same cathode sample (L-L scandate cathode #2) and was applied for doing 3D tomography, as presented in Fig. 6.8. It can be found that the chunky particle (the most left one, and with and shape of cuboid and the size of about 100nm x 100nm x 300nm) shows consistent signals of Ba and Al and O which is supposed to be $BaAl_2O_4$ based on previous analysis and the TKD results. Inside the tungsten particle, a cluster of spherical shaped particles (with the diameter of 20-120nm) were found, and which display a strong signal of Sc and O. It should be addressed that the signals of O and Sc are not strictly agreed with each other which means the internal particles may be a mixture of Sc and Sc_2O_3. This agrees with the characterization results that we found from L-S scandate cathode [14], as thoroughly discussed in Chapter 5. Moreover, it is interesting to mention that there is separate $BaAl_2O_4$ particle was found inside the tungsten grain. This may due to the given tungsten initially formed some pores at where the impregnant

materials were filled and subsequently reacted with the tungsten. As one of the reaction products, the $BaAl_2O_4$ was left inside the pores.

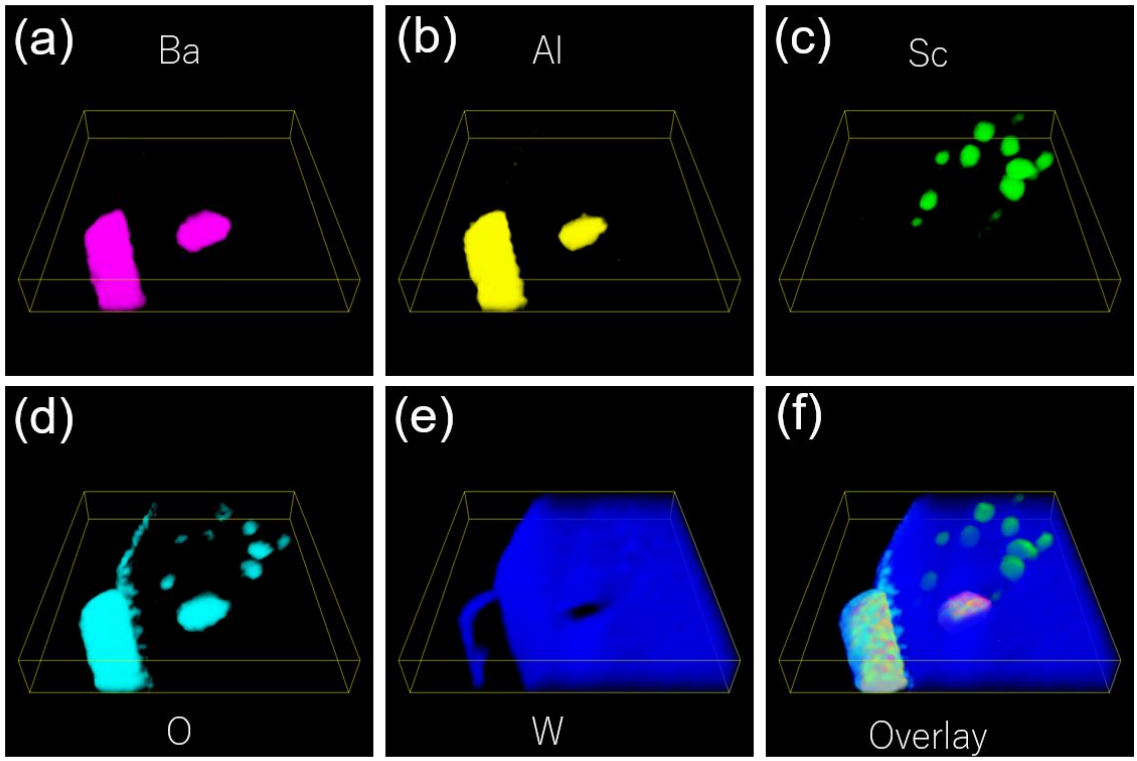

Figure 6.8 3D tomography on a lamella extracted from L-L scandate cathode #2. (a)-(e) 3D elemental distribution of Ba, Al, Sc, O and W, (f) 3D layered map. Note that the volume (x, y, z) = (906, 875, 133) nm.

The pristine powder prepared through the technique of L-L doping method was studied, as displayed in Fig. 6.9. The back-scattered image in Fig. 6.9 (a) presents the morphology of the powder: micron-scale tungsten particles are decorated with scandia nanoparticles, however, the tungsten surfaces were not completely covered. Superfine tungsten particles are mixed with nanoscale scandia particles, as indicated by the superfine white spots at the center areas in the image (a). We utilized FIB to cut one selected tungsten particle to investigate the internal features of the tungsten particles. Some pores with

various size were found as revealed by the cleaved surface in Fig. 6.9 (b), moreover, these pores were filled with scandia nanoparticles though it was not compactly stuffed. This may account for the formation of the oxide of $BaAl_2O_4$ locating inside tungsten grains as revealed by TEM 3D tomography as shown in Fig. 6.8. Because the impregnant of BaO-CaO-Al_2O_3 can reach the pores during the impregnation process and then react with the tungsten at the sites of wall pores. Eventually some of the inert products, e.g. $BaAl_2O_4$, are to be left.

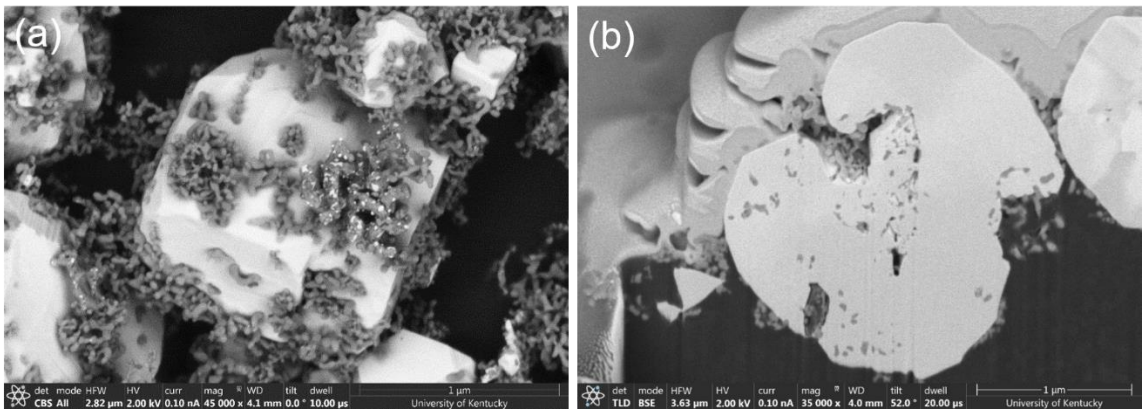

Figure 6.9 Back-scattered electron images of L-L scandia doped tungsten powder. (a) BSE image showing tungsten particles with scandia coverage, (b) cleaved surface of one tungsten particle showing internal pores with filled by scandia nanoparticles.

6.4 Discussion

As aforementioned the issue that operation mechanism of scandate cathode has not be fully understood seriously impedes its commercialization. Similar to the Ba-O dipole model for B type cathode, model(s) of Ba-Sc-O layer looks promising for scandate cathode. The bone of contention is, however, thickness of the Ba-Sc-O surface layer. From the semiconductor model (about 500 nm thick Ba-Sc-O layer) as claimed by Raju and Maloney [95] to the model of Ba-Sc-O monolayer proposed by Hasker [145], Zagwijin [109], and

Taguchi [8,146] and to the latest thick (100 nm) Ba-Sc-O surface layer as suggested by Wang and Liu [9,73,78].

To our best knowledge [9,24,63,72,73,75,78], no direct experimental evidence can be found for the Ba-Sc-O monolayer model. Moreover, as indicated in our preceding papers, the model of thick (100 nm) Ba-Sc-O surface layer was denied as no Ba-Sc-O layer on this order was discovered under (S)TEM examination. Here we succeed to image a thin Ba-Sc-O (~8nm) layer on cathode surface. The result differs to neither Ba-Sc-O monolayer nor the thick (100 nm) Ba-Sc-O surface layer. Considering the extremely small diffusion coefficient of Sc, thin Ba-Sc-O is reasonably easier to form than a thicker one. More detailed work, e.g., transformation route form initial Sc_2O_3 to the terminal Ba-Sc-O and its effect on decreasing work function, needs to be carried out for disclosing operation mechanism of scandate cathodes.

6.5 Conclusions

Surface chemicals of two scandate cathodes that emitted excellent were studied. Some conclusions could be derived.

(1) Tungsten grains on surfaces of both cathode #1 and cathode #2 are highly faceted and decorated with Ba-Al oxides, Sc_2O_3 and BaO nanoparticles. These features match typical surface characteristics of well emitted scandate cathodes.

(2) Knee temperatures of cathode #1 and cathode #2 are 860 $^{\circ}C_b$ and 831 $^{\circ}C_b$, respectively, which implies excellent emission capabilities.

(3) Elements of Sc, Ba and O distribute homogeneously throughout tungsten surface excluding sites of surface decorating particles of scandate cathodes.

(4) Thin Ba-Sc-O surface layer was imaged directly on cathode surface and its thickness was determined approximately 8 nm.

(5) The Ba-Sc-O surface layer constitutes of nano-sized polycrystalline materials as demonstrated by nano-beam diffraction pattern.

(6) Clustered Sc/Sc_2O_3 were found inside tungsten grains as revealed TEM 3D tomography. This is probably caused by the penetration of Sc_2O_3 into tungsten particles during the liquid-liquid doping process.

CHAPTER 7. SURFACE MICROSTRUCTURAL COMPARISON BETWEEN POISONED AND WELL EMITTED SCANDATE CATHODES

7.1 Introduction

Scandia doped tungsten impregnated cathodes (in short of scandate cathodes), one of the most promising thermal-electron emitting material, have attracted considerable attention and obtained continuous improvement in the recent decades [9,24,75,84,147]. In comparison with the conventional B-type cathodes, scandate cathode can provide a much higher current density at a lower working temperature. As can be found in literatures, Wang [72] showed that a space charge limited current density of over 30A/cm^2 has been routinely obtained for scandate cathodes. More impressively, as reported a laser ablation-deposited (LAD) coated thin film scandate cathode can reach the emission level of 400 A/cm^2 [53,148]. However, the scandate cathode has yet been extensively applied owing to several primary issues: emission uniformity, low reproducibility and the unclear operation mechanism responsible for the emission enhancement [6,10,149].

Apart from the high emission capabilities that we pursued for scandate cathodes another crucial perspective is the longevity and the corresponding failure mechanism of them. However, unfortunately, the factors determining the longevity of scandate cathode has yet been fully elucidated. According to the references [41,128,150–153], the life-limiting factors for scandate cathodes involve temperature, current induced intrinsic change, poisonous chemicals, ion bombardment and the resupply of active substances like Ba and Sc. More recently, as suggested by Yang et al [154], it was proved that a full restoring of emission can be obtained after scandate cathodes were exposed to air after a

re-activation process. Moreover, it has also been demonstrated that the poisoning pressure thresholds of residual gases for scandate cathodes are about half to one order of the magnitude higher than M type cathodes under the same temperature [154].

In previous chapters we have comprehensively studied surface characteristics of scandate cathode of outstanding emission performance (including both L-S and L-L scandate cathodes). As a complement, in this chapter, we investigate the surface characteristics of one typical poisoned scandate cathodes. Moreover, we compare the surface features the poisoned cathode with that of well emitted scandate cathodes. We aim at disclosing the surface disparities and correlating the surface characteristics with emission behavior of scandate cathodes. This may help us understand the fundamentals of scandate cathodes better.

7.2 Materials and methods

The scandate cathodes studied in this chapter were provided by the E-beam Incorporated. The poisoned scandate cathode (cathode #2 in the testing vehicle of N3808) was developed with L-L powder, detailed process for L-L doping approach can be found in chapter 3. The impregnant of the poisoned scandate cathode is $6BaO\text{-}1CaO\text{-}2Al_2O_3$. This cathode was then activated and tested for 4200 hours before studying its surface characteristics. The counterpart, well-emitting scandate cathodes are the same cathodes that have been studied in chapter 4, 5 and 6. Detailed information of these well emitted scandate cathode can be found the experimental part of the above 3 chapters.

The microstructure morphologies of both poisoned and good cathodes were observed using the Focused Ion Beam (FEI Helios Nanolab 660) equipped with back scattered electron detector. Note that it was under the immersion mode (2kV, 0.1nA) during the

morphological characterization which facilitates to acquire high resolution micrographs compared with using the free mode or regular scanning electron microscope. Chemical identification and semi-quantitative analysis was conducted with the Energy Dispersive X-ray Spectroscope (EDS) attached to the FIB facility. More specifically, the beam voltage applied was 20kV and the beam current was 0.8nA. Surface phases investigation was carried out using the X-ray Diffraction (D8) with Cu K_α radiation. Sample for atomic-level microstructure characterization was fabrication with the FIB and then studied employing the Transmission Electron Microscope (JEOL 2010F) with the acceleration voltage of 200kV.

7.3 Results and Discussion

7.3.1 Emission curves of the poisoned scandate cathode

The poisoned scandate cathode was activated and test in CSD for 4200 hours. The emission curves, current as a function brightness temperature (W), at 0 hour and 4200 hours were plotted in Fig. 7.1 As we stated before, the knee temperature defined as the intersection of extrapolation of temperature limited and the space charge limited, is a key parameter for evaluating the emission performance of a scandate cathode. As shown in Fig. 7.1 the knee point of this poisoned scandate cathode is 854 $^\circ C_b$ at the 0 hour (black curve) which is higher than that of the well emitting L-S scandate cathodes as discussed in chapter 4 and around to that of the L-L scandate cathode as indicated in chapter 5. However, as the red curve indicated the knee temperature of the cathode after running for 4200 hours becomes remarkably high since the space charge limited is not obvious as revealed by the end part of the curve (not reaching a “saturated” level). High knee temperature means the

scandate cathodes cannot reach its maximum emission even at a very high temperature. That is why it was judged as a poisoned one.

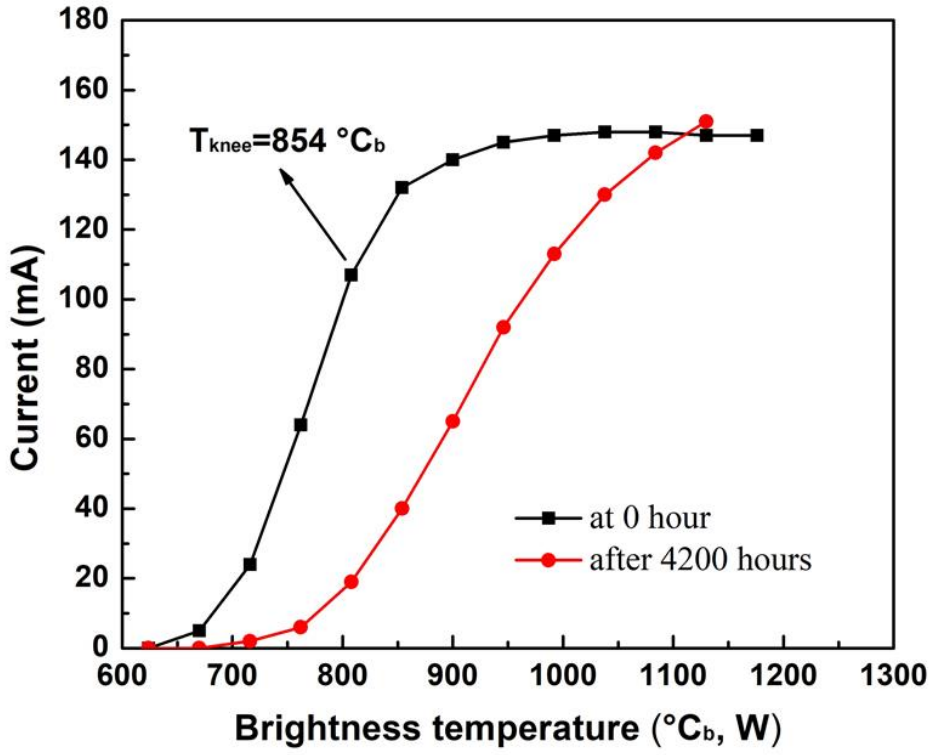

Figure 7.1 Emission curves of the poisoned scandate cathode. Black curve is the measurement at 0 hour while the red curve is after 4200 hours.

7.3.2 Morphology and surface particles identification

Surface morphology of the poisoned scandate cathode was observed using the FIB-SEM. Note that we use the immersion mode and image under 2kV and 0.1nA for acquiring high resolution micrographs, as displayed in Fig. 7.2. It can be seen from the Fig. 7.2 (a) and (b) that micron-scale tungsten particles are in the shape of quasi spherical. Moreover, three kinds of small decorating particles with different contrasts can be clearly observed: one is in grey color (100nm-300nm, marked as A), another is darker (50nm-100nm, marked as B) and the superfine spots (denoted as C). Furthermore, one remarkable characteristic is

that the pores between the tungsten particles in this poisoned scandate cathode are severely clogged, as can be seen in Fig. 7.2 (b). Figs. 7.2 (c) and (d) present a pair of images (one secondary electron imaging coupled with a corresponding back-scattered electron image), displaying that the tungsten particles are not strictly faceted. Instead one can find that some of the vertices and edges are rounded to a certain extent.

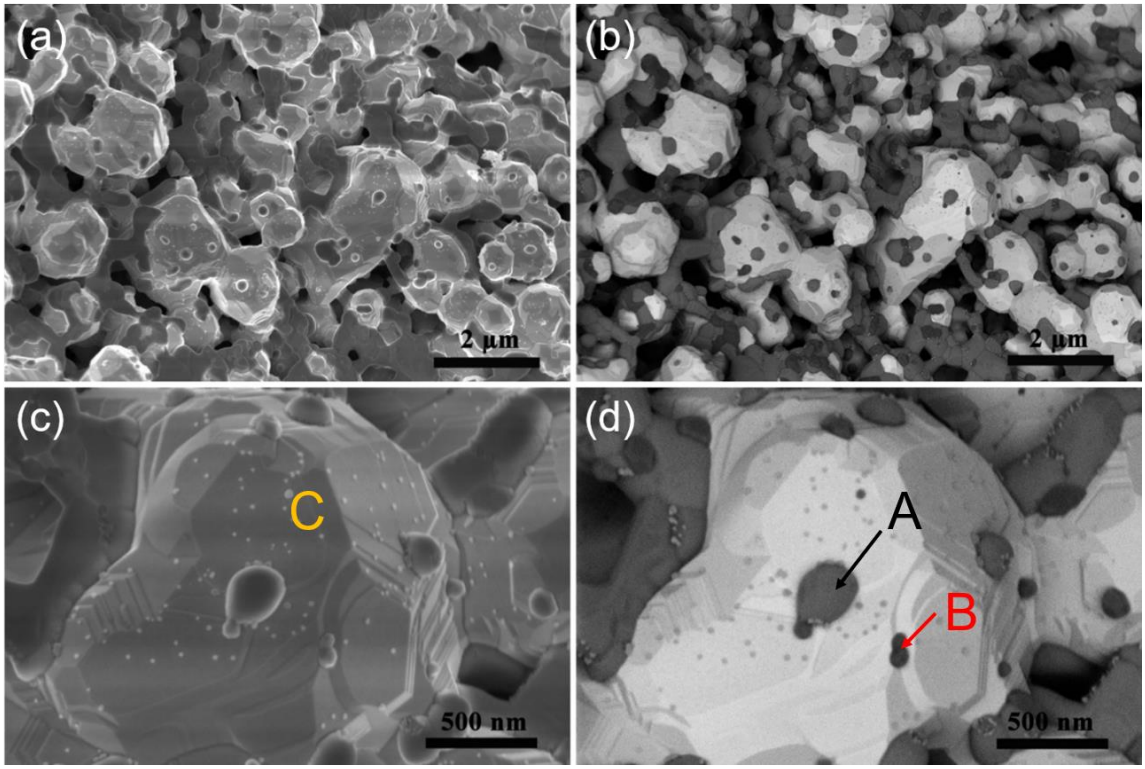

Figure 7.2 Scanning electron micrographs of the poisoned scandate cathode. (a) and (c) are secondary electron images, (b) and (d) are the corresponding back scattered electron images.

It is commonly accepted that the tungsten matrix having a homogeneous size is favorable for generating uniform pores which is important for scandate cathodes since at least the Ba replenishment is closely related to it. Consequently, we measured the average grain size of tungsten particles for both the poisoned scandate cathode and one good scandate cathode (cathode #1 studied in chapter 4), as shown in Fig. 7.2. About 500

tungsten particles were measured using the Image J for calculating the average grain size. It shows that for the poisoned scandate cathode tungsten particles range from 0.4 μm to 2.4 μm and with an averaged value of 1.1μm (± 0.32 μm). Similarly, the average size of tungsten particles for the good scandate cathode is 1.16μm (± 0.45 μm). No large difference in terms of the tungsten particle size is found between the poisoned and well emitted scandate cathodes. Moreover, both of the them, the measured average tungsten size is approximate to the reported number in Wang's work [9,76].

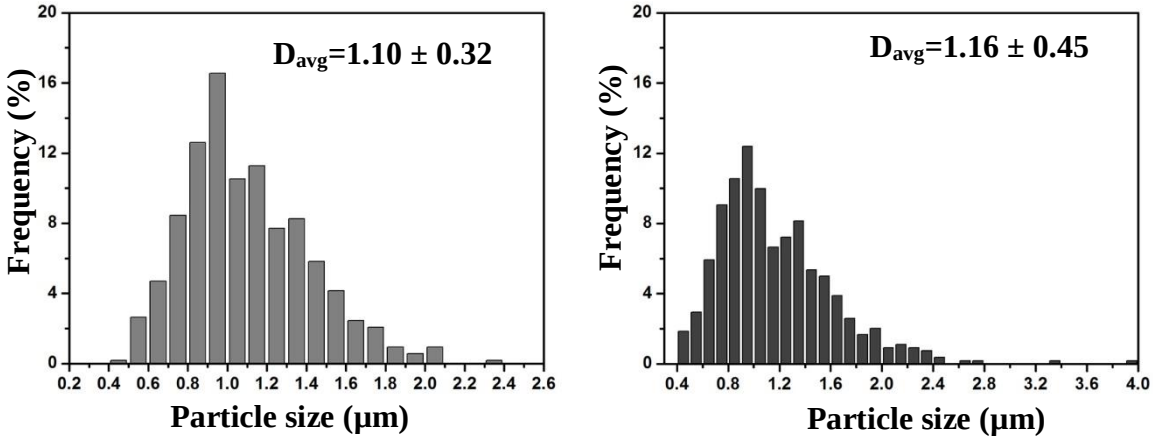

Figure 7.3. Size distribution of tungsten particles of poisoned (left) and healthy (right) scandate cathodes.

7.3.3 Chemical analysis on surface decorating particles

EDS is used to study the surface decorating particles for the poisoned scandate cathode, as presented in Fig. 7.4. The voltage for EDS measurements is 20kV for covering the characteristic X-rays for all the elements appearing in scandate cathodes. At least 5 points have been measured for obtaining the chemical composition of the surface particles of A and B. Note that the finest particles of C are too small to be measured with EDS. According to what we previously discussed [50], the particles C should be BaO which was

original Ba and oxidized to BaO due to air exposure. Specific measured chemical compositions of A and B are displayed in Table 7.1.

From table 7.1 the measured composition (at. %) of particle A is Ba (13.56), Al (17.3), O (33.97), Sc (1.17) and W (34.27). First the signal of W comes from the matrix-W and the slight amount of Sc may result from the neighboring Sc-rich particle (particle B). Considering that the ratio of Ba/Al is between 1:1 and 1:2 which correspond to the compounds of $BaAl_2O_4$ and $Ba_2Al_2O_5$. As a result, it is possible that particles A are mixture of the $BaAl_2O_4$ and $Ba_2Al_2O_5$ compounds. For the particle B, the measured composition (at.%) is Sc (14.64), O (29.01), Ba (1.13), Al (0.78), and W (54.44), implying that is to be Sc_2O_3 though the amount of O is little higher for fitting the stoichiometry of the Sc_2O_3 compound. This is may be due to the noise from the environment during the EDS analysis.

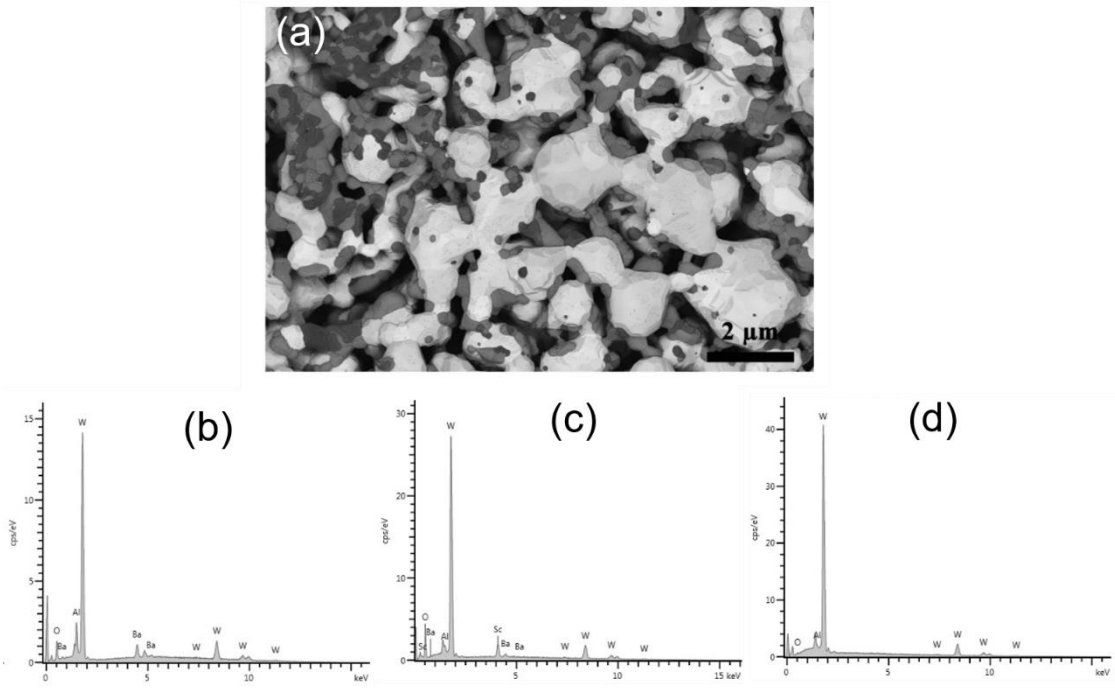

Figure 7.4 EDS analyses of the poisoned scandate cathode. (a) SEM image, (b)-(d) relative EDS spectra for particles A, B and the matrix-tungsten.

Table 7.1 Quantified results of particles A, B and the matrix-W for the poisoned scandate cathode.

Particles	O (at. %)	Al (at. %)	Sc (at. %)	Ba (at. %)	W (at. %)
A	33.97±7.17	17.03±2.24	1.17±0.72	13.56±0.84	34.27±9.69
B	29.01±5.02	0.78±1.70	14.64±4.18	1.13±0.77	54.44±8.82
tungsten	2.79±3.17	0.22±0.69	0±0	0.41±0.66	96.58±3.62

One EDS map acquired (under 20 kV and 0.8 nA) on a representative area on the surface of the poisoned scandate cathode, as shown in Fig. 7.5. The upper two images in Fig. 7.5 (a) and (b) display the area for EDS mapping and the layered map, below is the elemental maps of W, Al, Ba, Sc, O and C. It can be clearly seen that most of the surface particles A are jointed together and show well agreed signals of Ba, Al and O, which is consistent with the EDS quantified results. For the sites of B particles, the signal of Sc agrees well with O, implying that these particles are most likely to be the Sc_2O_3.

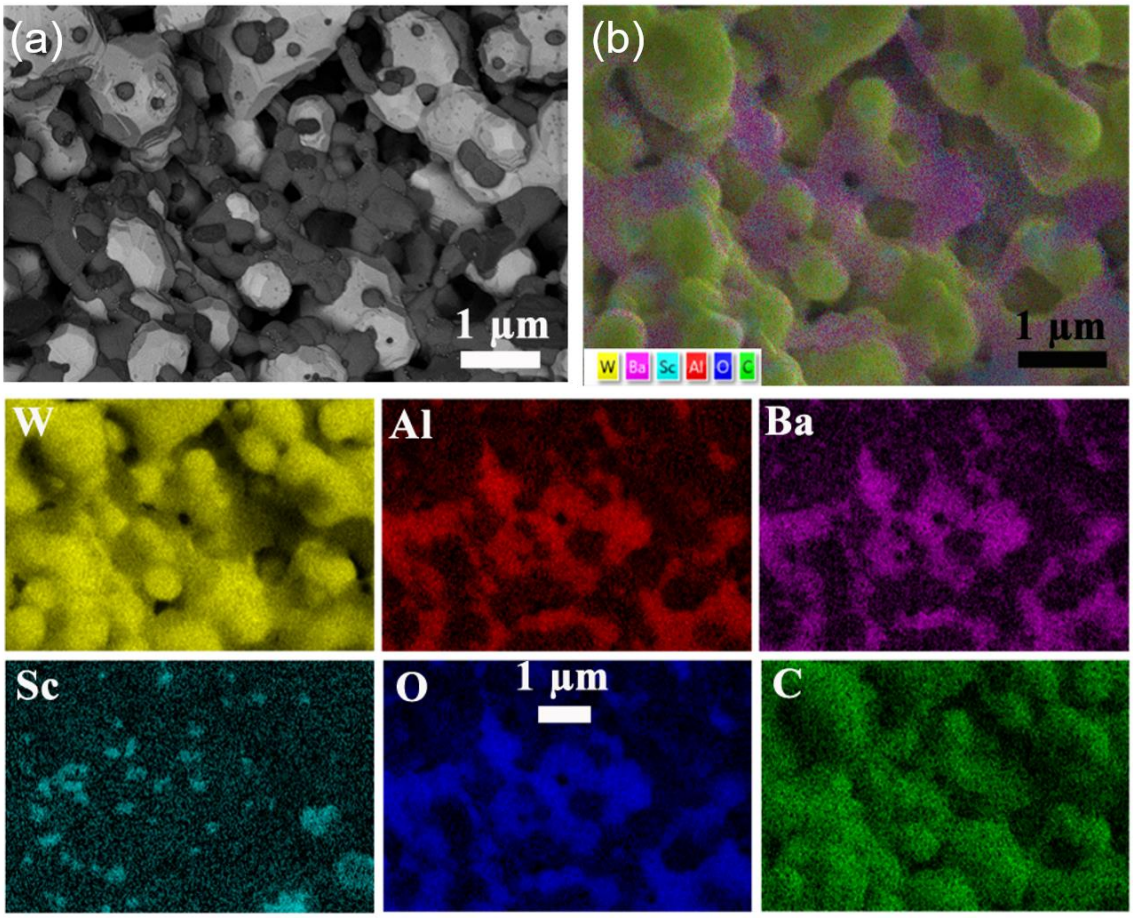

Figure 7.5 EDS mapping on a representative area of the poisoned scandate cathode. (a) SEM image showing the area for mapping, (b) layered image, below is the elemental maps of W, Al, Ba, Sc, O and C.

7.3.4 Faceting and rounding behavior of poisoned scandate cathode

In light of our previous work [50,88,114,155], it has been demonstrated that for well emitted scandate cathodes the tungsten particles are highly facetted with showing exclusive crystallographic planes of {100}, {110} and {112}. However, for the poisoned scandate cathodes, one can observe the rounding behavior (including edge rounding and vertex rounding) as aforementioned in the section of 7.1.2. In this part we will discuss the faceting and rounding behavior of tungsten crystal for the cathodes materials system.

Based on the theory of equilibrium crystal shape (ECS) yielding information on temperature-dependent surface free energy, at absolute zero polyhedral shapes are predicted with atomically sharp vertices and sharp edges [13,156,157]. As the temperature increases, rough regions will appear due to the entropic effects. Vertices first become rounded when the temperature is higher than the vertex rounding temperature (T_v) and then edges become rounded when the temperature exceeds the edge round temperature (T_e), as schematic illustrated by Fig. 7.6 [13].

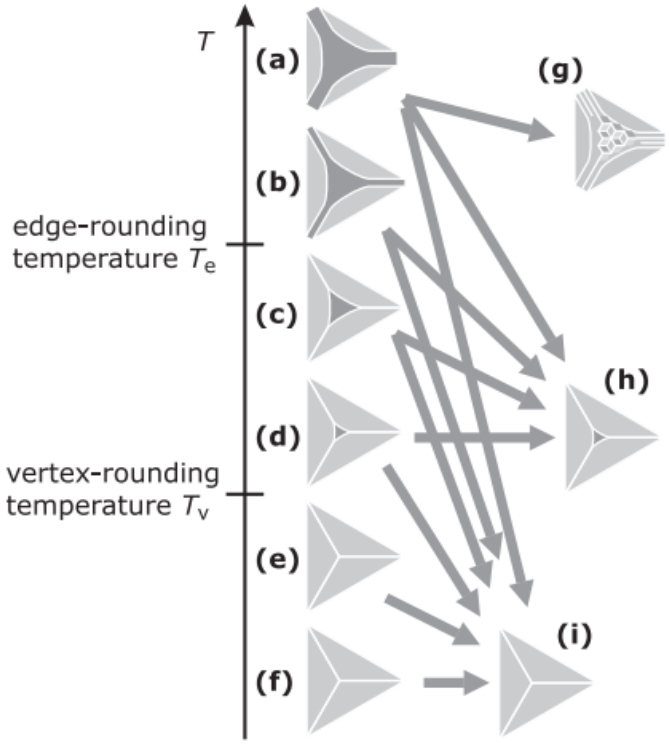

Figure 7.6. (a)-(f) the proposed equilibrium crystal shape in the vicinity of the crystal vertex depends on temperature. (g)-(i) The actual crystal shape observed after quenching. The observed shape depends on the cooling rat and may differ from the equilibrium shape. During quenching small step-like facets may be form as shown in (g) [13].

According to reference [13] the crystal shape of oxygen covered tungsten follows the evolution sequence starting with sharp polyhedral to undergoing vertices rounding and then

edge rounding as the temperature increases. Experimentally observed tungsten shapes from the poisoned scandate cathode along with temperature dependent theoretical crystal shapes are compared, as shown in Fig. 7.7. Note that the two characteristic temperatures denote T_v and T_e, namely the vertices rounding temperature and the edge rounding temperature. In another words, the crystal shape remains polyhedral when the temperature lowers than T_v, then the vertices first become rounded as the temperature exceeds T_v which is followed the edge rounding when the temperature is eventually higher than the T_e. As can be seen in Fig. 7.7, some of the tungsten shapes are sharp as indicated by the left SEM image in Fig. 7.7 b. However, majority of the tungsten shape are displaying rounded vertices and edges, as exhibited in the middle and right micrographs in Fig 7.7 (b).

As suggested by Szczepkowicz [13] the vertices rounding temperature for O covered W is 960K (~688 ˚C) and then edge rounding temperature is between 1300K~1400K (1028 ˚C ~1128 ˚C). Considering the activation temperature of scandate cathode is normally around 1150 $^{\circ}C_b$ (W) which is higher the T_e as indicated by Szczepkowicz [13]. It should be noted that though the activation recipe for all the scandate cathodes is almost identical, the distinct vertex-rounding and edge-rounding imply that the poisoned scandate cathode may undergo abnormal high temperature during the impregnation, or activation or the emission-testing processes. The abnormal high temperature is possibly responsible for the poisoned behavior for scandate cathodes. In addition, as studied by Tracy and Blakely [117,158] the faceting behavior of tungsten is sensitive the pressure of oxygen. More specifically the thermal faceting of the (100), (112), and (111) transforming to (110) were observed in the presence of oxygen at pressures between 10^{-8}~10^{-6} torr [117]. In addition as suggested by the reference [13], oxygen is known to raise the anisotropy of the surface

free energy of tungsten thus to induce pronounced thermal faceting of the surface. Based on these, one speculation for the rounding behavior occurred for the poisoned scandate cathodes is that the oxygen content exceeds one specific range within which the vertices and edge are sharp. In more recent publications [94,101], it was suggested that Sc may play a crucial role in regulating oxygen concentration on the surface of scandate cathodes. Moreover, as discussed in the references [50,155], different facets have various surface energy and work function which directly influence the electron emission of scandate cathodes.

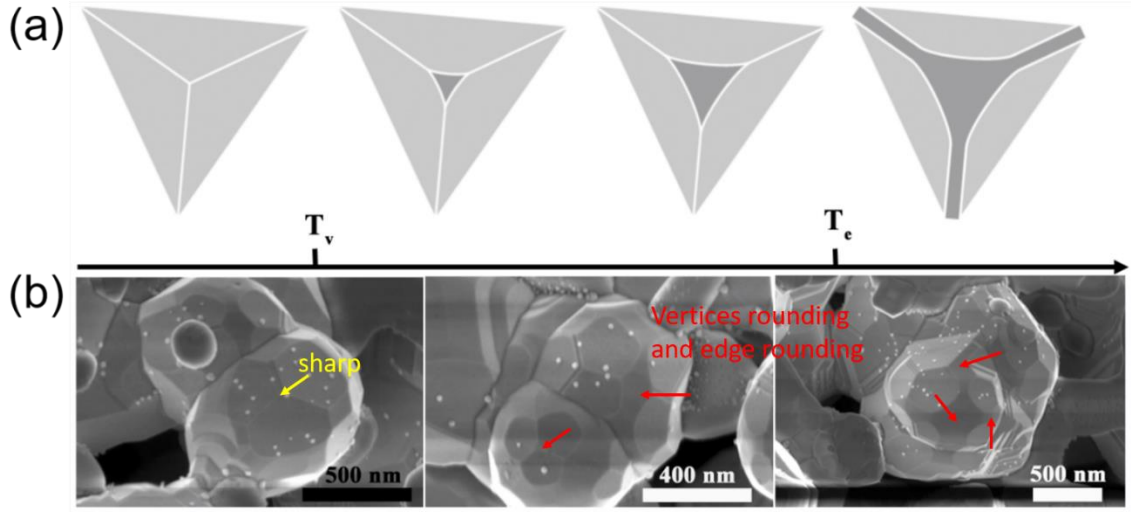

Figure 7.7 Theoretical and experimental tungsten crystal shape for the poisoned scandate cathode. (a) [13] Crystal shape follows a function of temperature on the basis of Equilibrium Crystal Shape (ECS), T_v and T_e are vertex-rounding and edge-rounding temperature, respectively. (b) Experimentally observed tungsten shapes form the poisoned scandate cathode, showing vertices rounding and edge rounding.

7.4 Conclusions

The surface morphological characteristics and surface decorating particles for poisoned scandate cathodes have been studied in comparison with the well-emitting scandate cathodes. Moreover, the faceting and rounding behavior for the tungsten shapes

has been discussed in terms of temperature and oxygen concentration. Some conclusion can be drawn based on the analysis:

(1) The knee temperature of the poisoned scandate cathodes becomes rather high after the emission testing for 4200 hours though its initial knee point is reasonable.

(2) Though the tungsten grain size between the poisoned scandate cathode and the excellent scandate cathode (the cathode #1 in chapter 4) is roughly equivalent, the pores on poisoned scandate cathode surface are severely clogged rather than in an open state as observed for the good scandate cathode.

(3) The surface decorating particles for the poisoned scandate cathode are probably $Ba_2Al_2O_5$ (or mixture of $Ba_2Al_2O_5$ and $BaAl_2O_4$), Sc_2O_3 and the superfine BaO.

(4) For well-emitting scandate cathode, the tungsten particles are highly facetted, the poisoned scandate cathode, however, underwent vertices rounding and edge rounding. This may cause by abnormal high temperature or high oxygen concentration.

CHAPTER 8. CONCLUSIONS AND FUTURE WORK

In this doctoral work, various scandate cathodes (including L-S scandate cathodes of good emission, L-L scandate cathodes of good emission, poisoned scandate cathodes) were synthesized and characterized in detail from the perspectives of surface phases, surface morphologies, and cross-section nanostructures, etc. Various scandia doped tungsten powders (prepared through the L-S and L-L doping techniques) and the pristine pure tungsten powder were also analyzed. The materials characterization work was carried out using state-of-the-art electron microcopies and the surface analytical techniques, e.g., XPS and Nano-AES. The electron emission capabilities of these scandate cathodes were also tested and evaluated.

First, thorough surface characterization has been performed on scandate cathodes exhibiting excellent emission capabilities, and it has been demonstrated that well emitted scandate cathodes share some representative surface characteristics.

1) Scandate cathodes of outstanding emission capabilities have significant low knee temperatures: for good L-S scandate cathodes, the knee points range from 820 $^{\circ}C_b$ to 837 $^{\circ}C_b$; for good L-L scandate cathodes, the knee temperature is 830-860 $^{\circ}C_b$. In addition, the transition from the temperature limit to space charge limit in the curves of current density as a function of brightness temperature is sharp which means the cathode can reach an optimum electron emission at a relatively lower temperature.
2) Scandate cathodes of excellent emission share some surface features: micron-scale tungsten particles are equiaxed and exhibit highly degree of surface

faceting; tungsten grains are decorated with three different types of nanoscale particles which are $BaAl_2O_4$ (~100 nm), Sc_2O_3 (~100 nm) and BaO (~10 nm).

3) Through Wulff-construction analysis, facets constituting the surfaces of tungsten grains for well emitted scandate cathodes are determined to be {100}, {110} and {112} crystallographic planes. It should be noted that according to the Wulff analysis, the normalized surface energies for these facets are 1.00: 1.08: 1.02. Moreover, the facets of {112} dominate the surface area of tungsten grains with a surface area percent of 69%. Each {100} or {110} facet is surrounded by four {112} facets. In addition, ledges and microfacets only exist in the neighboring facet-pairs of {100}/{112}, {110}/{112} and {112}/{112}, indicating the tungsten grains are approaching their equilibrium shape during high temperature cathode operation.
4) The smallest nanoparticles (~10nm) are identified to be BaO based on experimental calculation coupled with theoretical analysis. Moreover, it is believed that metallic Ba covering cathode surface at the operating temperature transforms to dispersed hemispheres after the cooling process. The Ba is then oxidized due to air exposure and forms the BaO nanodots. The quantity of Ba is determined to be half monolayer (0.5 (+0.05/-0.12) ML), indicating a full coverage of Ba on cathode (tungsten) surface during the operation.
5) No Ba-Sc-O surface layer on the order of 100 nm was found on scandate cathode surface based on detailed (S)TEM examination on lamellae extracted from the cathodes. This contradicts the model of “100 nm Ba-Sc-O” proposed and developed by Wang et al.

In addition, near-surface microstructures have been studied in detail with studying on the cross-section samples extracted from good L-S scandate cathodes. Based on the results, some conclusion can be drawn.

1) The majority of particles that attached to the surfaces and edges of tungsten grains are $BaAl_2O_4$ (with the size of several hundreds of nanometers). In addition, $BaAl_2O_4$ particles are contiguous with Sc_2O_3 or envelop Sc_2O_3 particles.
2) The oxides of $BaAl_2O_4$ and Sc_2O_3 appear to be physically separate to each other, as revealed by 3D tomogram, indicating that there is no chemical interaction or mixing between them.
3) Scanning nanobeam electron diffraction showed that the crystal structure of W grains remains body-centered cubic in the scandate cathodes after emission testing, implying that the crystal structure of the matrix-W did not change significantly as a result of the complex chemical reactions that took place during the impregnation, activation and operation processes.
4) 3D tomographic reconstruction revealed that a certain amount of Sc/Sc_2O_3 appear inside of W grains. Interestingly, these nanoscale Sc/Sc_2O_3 tend to cluster or align in certain region of a given W grain, rather than distributed uniformly throughout the W grains. This phenomenon may due to the infiltration of Sc_2O_3 particles into W during the L-S doping process. Moreover, it is found that the entrapped Sc/Sc_2O_3 contains many superfine W with the diameter of 1-10 nm as revealed by high-resolution EDS.

Regarding the model of 100 nm Ba-Sc-O surface layer, it is maybe safe to say that we have not found the Ba-Sc-O surface layer with this thickness after comprehensive

characterization on multiples scandate cathode samples. However, one inspiring result is that we found a very thin Ba-Sc-O surface layer (about 8 nm) using the technique of EELS in conjunction with STEM on a well emitted L-L scandate cathode surface. This provides new insights, to some extent, to unravel the emission mechanism of scandate cathodes though it remains unclear. Consequently, it should be noted that, according to the results in this work, neither the model of "100 nm Ba-Sc-O surface layer" nor the model of "Ba-Sc-O monolayer" is accurate for scandate cathodes. One possible model is a thin Ba-Sc-O (less than 10 nm) responsible for then emission enhancement for scandate cathode as presented and discussed in chapter 6.

Based on the availability of facilities and our current understanding on scandate cathodes, some future work can be performed as a continuation of this research.

1) Study on materials change during the activation process of scandate cathodes. In our lab we are developing a "cathode characterization chamber" with which the activation process can be studied directly with analyzing the gas change using the residual gas analyzer (RGA). The chamber can be heated to a maximum temperature of 1400 ˚C which is higher than the normal activation temperature of scandate cathodes (~1150 ˚C_b). Performing this research is imperative for gaining a better understanding of the activation process for scandate cathodes. We could use the RGA to conduct quantitative studies in terms of materials change, e.g., Ba(g), O_2, Ca(g) and even the free Sc, that occurred during activation. All these results will provide valuable insights into clarifying the activation process of scandate cathodes.

2) Measure work function of scandate cathode at high temperature. In our lab, another important component of the "cathode characterization chamber" is the Kelvin probe enabling us to measure the work function at elevated temperatures. It is challenging to measure the work function of thermionic cathodes at high temperature and none of this work has been carried out for scandate cathodes till to date according to author's knowledge. By conducting this research we can get to know how does the work function vary during the activation and operating periods. A relation can be built between the variation of work function and the materials change analyzed by RGA as described in last point.

3) In-situ SEM observation on tungsten morphological change under high temperature. According to this research we found that scandate cathode of excellent electron emission share some typical surface features. One of them is that tungsten particles are highly faceted with showing exclusive facets of {100}, {110} and {112}. Also we have analyzed the cathode before activation and emission-testing (impregnated pellet) and found that the tungsten grains are not faceted. With considering these, it should be helpful to do some in-situ SEM study on the morphology of tungsten under high temperature and to figure out what triggers the morphological alteration. This is important since different facets have different work function which directly influence the emission capabilities of scandate cathode according to the Richardson equation. In addition, we can try to figure out what control the morphology evolution for the cathode materials system and then we may be able to "design" cathodes with a specific shape favorable to electron emission.

4) Conduct computation work for studying the effect of thin Ba-Sc-O surface layer (1-10 nm) on emission properties of scandate cathode. One of the most inspiring discoveries in this research is that we identified a thin Ba-Sc-O surface layer (~8 nm) on emitting surface of a well emitted L-L scandate cathode. This result fundamentally differs to the previous models (Ba-Sc-O monolayer or the 100 nm Ba-Sc-O surface layer) and should be very important for understanding and developing a new (revised) emission model for scandate cathodes.

With the further research on scandate cathodes, the author believe that we will get a better understanding the materials system of scandate cathodes. With solving those problems for scandate cathodes, we will eventually realize the application of scandate cathodes in VEDs and other important devices.

APPENDIX . TERMS IN THERMIONIC DISPENSER CATHODES

A series of terms are frequently used in the cathode research community as well as in this thesis. For the sake of helping read this thesis, some of the frequently used terms are explained and listed below.

(1) Dispenser cathodes: dispenser cathodes correspond to cathodes where the active substances can be continuously replenished from body to the surface to maintain the electron emission.

(2) Thermionic emission: thermionic emission is a term describing the emission of electrons from a given material at a temperature which the electrons within the material have adequate kinetic energy to overcome the potential barrier keeping them confined to the materials.

(3) Temperature limited emission: temperature limited emission means the thermionic emission of electrons limited solely by temperature.

(4) Space charge limited emission: temperature limited emission only spans at a finite range of temperature which means the current density is no longer increasing with temperature at a very huge temperature. Under this situation the only way to increase current at the anode is to apply a potential, as a result the current density is therefore a function of applied potential. Emission of this type is called space charge limited emission. We usually use the Child's Law, also referred as three halve power law, which is [5]:

$$J = \frac{4\varepsilon_0}{9}\sqrt{\frac{2e}{m_e}}\frac{V_a^{3/2}}{d^2} \approx 2.3\times10^{-6}\frac{V_a^{3/2}}{d^2}$$

Where J is the current density, ε_0 is the permittivity of free space, e is the charge of an electron, m_e is the mass of an electron, V_a is the anode voltage and d is the spacing between the anode and the cathode.

(5) Transition from temperature limited to space charge limited current: this term typically refers to a range of temperatures from temperature limited to space limited charge in the curve of current density versus temperature. The shape of the transition region provides insight for evaluating the emission characteristics of cathodes like emission uniformity.

(6) Knee temperature: knee temperature is an important parameter in emission testing cathodes that derives from current density versus temperature plot. It is the intersection of lines linear fitted to temperature limited region and space charge limited region respectively.

(7) Work Function: work function is defined as the energy required for an electron to move from the Fermi level to the vacuum lever and whose magnitude equals to potential difference between the two levels.

(8) Schottky effect: the Schottky effect is also called field enhanced thermionic emission. With applying an electric field, the surface barrier lowers by an amount ΔW and increase the emission current. It can be described using a revised Richardson equation [37]. Though a small external is not enough to induce pure field emission, it is still lower the barrier for thermionic emission.

$$J = AT^2 \, \mathrm{e}^{\frac{-(\Phi - \Delta W)}{kT}}$$

(9) Schottky plot: based on the schottky effect surface barrier for thermal emission decreased by applying an external potential. A more precise modified Richardson equation [5] is expressed as

$$J = AT^2 \, e^{\frac{-(\Phi - \sqrt{\frac{eF}{4\pi\varepsilon_0}})}{kT}} \approx AT^2 \exp[\frac{1}{T}(\frac{-\phi}{k} + 4.4\sqrt{\frac{V}{d}})]$$

Where V is the anode voltage and d is the effective spacing between anode and cathode. It is difficult to determine magnitude of d precisely since multiple factors, like shape of the emitting surface, temperature and thermal expansion, could make an influence on that.

A schottky plot is simply a plot of ln(J) versus $V^{1/2}$ at various temperatures. These plots can be used to determine the zero-field current density J0 by extrapolating from the linear portion of the plot corresponding to temperature limited emission to zero applied voltage.

(10) Brightness temperature: Brightness temperature ($^{\circ}C_b$) is often used in thermionic cathodes which is a unit of temperature. It was measured using an optical pyrometer focused on the molybdenum support body whose temperature is identical to the cathode itself.

References

1. Thomas, R.E.; Gibson, J.W.; Haas, G.A.; Abrams, R.H. Thermionic Sources For High-Brightness Electron Beams. *IEEE Trans. Electron Devices* **1990**, *37*, 850–861.

2. Forman, R. A proposed physical model for the impregnated tungsten cathode based on Auger surface studies of the Ba-O-W system. *Appl. Surf. Sci.* **1979**, *2*, 258–274.

3. Hasker, J.; Stoffelen, H.J.H. "Alternative" auger analysis reveals important properties of M-type and scandate cathodes. *Appl. Surf. Sci.* **1985**, *24*, 330–339.

4. Wang, Y.; Wang, J.; Liu, W.; Zhang, K.; Li, J. Development of high current-density cathodes with scandia-doped tungsten powders. *IEEE Trans. Electron Devices* **2007**, *54*, 1061–1070.

5. Swartzentruber, P.D. Microstructure and Work Function of Dispenser Cathode Coatings : Effects on Thermionic Emission. **2014**.

6. Kirkwood, D.M.; Gross, S.J.; Balk, T.J.; Beck, M.J.; Booske, J.; Busbaher, D.; Jacobs, R.; Kordesch, M.E.; Mitsdarffer, B.; Morgan, D.; et al. Frontiers in Thermionic Cathode Research. *IEEE Trans. Electron Devices* **2018**, *65*, 2061–2071.

7. Sasaki, S.; Yaguchi, T.; Nonaka, Y.; Taguchi, S.; Shibata, M. Surface coating influence on scandate cathode performance. *Appl. Surf. Sci.* **2002**, *195*, 214–221.

8. Yamamoto, S.; Watanabe, I.; Taguchi, S.; Sasaki, S.; Yaguchi, T. Formation mechanism of a monoatomic order surface layer on a sc-type impregnated Cathode. *Jpn. J. Appl. Phys.* **1989**, *28*, 490–494.

9. Wang, Y.; Wang, J.; Liu, W.; Li, L.; Wang, Y.; Zhang, X. Correlation between emission behavior and surface features of scandate cathodes. *IEEE Trans. Electron Devices* **2009**, *56*, 776–785.

10. Vancil, B.; Brodie, I.; Fellow, L.; Lorr, J.; Schmidt, V. Scandate Dispenser Cathodes With Sharp Transition and Their Application in Microwave Tubes. **2014**, *61*, 1754–1759.

11. Wilkinson, A.J.; Britton, T. Ben Strains , planes , and EBSD Electron back scatter

diffraction (EBSD) has made an impressive impact. *Mater. Today* **2012**, *15*, 366–376.

12. Sneddon, G.C.; Trimby, P.W.; Cairney, J.M. Transmission Kikuchi diffraction in a scanning electron microscope : A review. *Mater. Sci. Eng. R* **2016**, *110*, 1–12.

13. Szczepkowicz, A. Oxygen-covered tungsten crystal shape: Time effects, equilibrium, surface energy and the edge-rounding temperature. *Surf. Sci.* **2011**, *605*, 1719–1725.

14. Liu, X.; Vancil, B.K.; Beck, M.J.; Balk, T.J. Near-Surface Material Phases and Microstructure of Scandate Cathodes. *Materials (Basel).* **2019**, *12*, 1–15.

15. John Balk, T.; Liu, X.; Zhou, Q.; Maxwell, T.; Beck, M.J.; Vancil, B. Materials characterization of surface phases in scandate cathodes. In Proceedings of the 2018 IEEE International Vacuum Electronics Conference, IVEC 2018; 2018.

16. Forman, R. The role of oxygen in the low work function surface complex of barium on oxygen on tungsten (substrate). *Appl. Surf. Sci.* **1986**, *25*, 13–31.

17. Cronin, J.L. Modern Dispenser Cathodes. *IEEE Proc.* 1981, 19–31.

18. Li, J.; Yan, S.; Shao, W.; Chen, Q.; Zhu, M. Investigation and application of impregnated scandate cathodes. *Appl. Surf. Sci.* **2003**, *215*, 49–53.

19. Levi, R. Improved "Impregnated Cathode". *J. Appl. Phys.* **1955**, *26*, 638–640.

20. Wang, S. Scandate cathode for TWT. *Appl. Surf. Sci.* **2005**, *251*, 114–119.

21. Zhang, X.; Wang, J.; Wang, Y.; Liu, W.; Zhou, M.; Gao, Z. Investigation of Influence of Surface Nanoparticle on Emission Properties of Scandia-Doped Dispenser Cathodes. *Funct. Mater. Lett.* **2013**, *06*, 1350040.

22. Liang, W.; Wang, Y.; Wang, J.; Liu, W.; Yang, F. DC emission characteristic of nanosized-scandia-doped impregnated dispenser cathodes. *IEEE Trans. Electron Devices* **2014**, *61*, 1749–1753.

23. Wang, J.; Li, L.; Liu, W.; Wang, Y.; Zhao, L.; Wang, Y. Preparation and

characterization of scandia and Re doped tungsten matrix impregnated cathode. *J. Phys. Chem. Solids* **2007**, *68*, 2209–2215.

24. Wang, Y.; Wang, J.; Liu, W.; Zhang, X.; Li, L. Emission mechanism of high current density scandia-doped dispenser cathodes. *J. Vac. Sci. Technol. B, Nanotechnol. Microelectron. Mater. Process. Meas. Phenom.* **2011**, *29*, 04E106.

25. Jenkins, R. A review of thermionic cathodes. *Vacuum* **1969**, *19*, 353–359.

26. Kapustin, V.I.; Li, I.P.; Shumanov, A.V.; Lebedinskii, Y.Y.; Zablotskii, A.V. Physical operating principles of scandate cathodes for microwave devices. *Tech. Phys.* **2017**, *62*, 116–126.

27. Shroff, A.M.; Palluel, P.; Tonnerre, J.C. Performance and life tests of various types of impregnated cathodes. *Appl. Surf. Sci.* **1981**, *8*, 36–49.

28. Rittner, E.S.; Rutledge, W.C.; Ahlert, R.H. On the mechanism of operation of the barium aluminate impregnated cathode. *J. Appl. Phys.* **1957**, *28*, 1468–1473.

29. Shih, A.; Yater, J.E.; Hor, C. Ba and BaO on W and on Sc2O3coated W. *Appl. Surf. Sci.* **2005**, *242*, 35–54.

30. Higuchi, T.; Nakamura, O.; Matsumoto, S.; Uda, E. Pore geometry of dispenser cathode surface vs. emission characteristics, and Ba recovery characteristics after ion bombardment. *Appl. Surf. Sci.* **1999**, *146*, 51–61.

31. Koenig, M.F.; Grant, J.T. XPS studies of the chemical state of Ba on the surface of impregnated tungsten dispenser cathodes. *Appl. Surf. Sci.* **1985**, *20*, 481–496.

32. Tonnerre, J.C.; Brion, D.; Palluel, P.; Shroff, A.M. Evaluation of the work function distribution of impregnated cathodes. *Appl. Surf. Sci.* **1983**, *16*, 238–249.

33. Forman, R. Surface studies of barium and barium oxide on tungsten and its application to understanding the mechanism of operation of an impregnated tungsten cathode. *J. Appl. Phys.* **1976**, *47*, 5272–5279.

34. Ralph, F. Surface Studies of Thermionic Cathodes and the Mechanism of Operation of an Impregnated Tungsten Cathode. *Nasa Tech. Note* **1991**, *39*, 1545–1552.

35. Makarov, A.P.; Kultashev, O.K. A work model for barium dispenser cathodes with the surface covered by metal Os, Ir or Os <Ir> W alloy layer. *Appl. Surf. Sci.* **1997**, *111*, 56–59.

36. Swartzentruber, P.D.; Detisch, M.J.; Balk, T.J. In-vacuo work function measurement of dispenser cathodes. *2016 IEEE Int. Vac. Electron. Conf. IVEC 2016* **2016**, 5–6.

37. Li, J.; Yu, Z.; Shao, W.; Zhang, K.; Gao, Y.; Yuan, H.; Wang, H.; Huang, K.; Chen, Q.; Yan, S.; et al. High current density M-type cathodes for vacuum electron devices. *Appl. Surf. Sci.* **2005**, *251*, 151–158.

38. Isagawa, S..; Higuchi, T..; Kobayashi, K. Application of M-type cathodes to high-power cw klystrons. In Proceedings of the 2nd International Vacuum Electron Sources Conference; 1998; pp. 1–18.

39. Yin, S.; Zhang, Y. Emission mechanism and technical progresses for M-type cathodes. *2012 IEEE 9th Int. Vac. Electron Sources Conf. IVESC 2012* **2012**, 467–468.

40. Chen, D.S.; Lindau, I.; Hecht, M.H.; Viescas, A.J.; Nogami, J.; Spicer, W.E. Surface studies of the tungsten dispenser cathode. *Appl. Surf. Sci.* **1982**, *13*, 321–328.

41. Liu, W.; Wang, Y.; Zhu, X.; Ynag, Y.; Yang, F.; Wang, J. Investigation on robustness of Nanosized-Scandia Doped Dispenser Cathodes. *2016 IEEE Int. Vac. Electron. Conf. IVEC 2016* **2016**, 2–3.

42. Lai, C.; Wang, J.; Zhou, F.; Liu, W.; Hu, P.; Wang, C.; Wang, R.; Miao, N. Preparation and surface characteristics of Re3W matrix scandate cathode: An experimental and theoretical study. *Appl. Surf. Sci.* **2018**, *440*, 763–769.

43. Barik, R.K.; Singh, A.K.; Shukla, S.; Singh, T.P.; Raju, R.S.; Park, G.S. Development of Nanoparticle-Based High Current Density Cathode for THz Devices Application. *IEEE Trans. Electron Devices* **2016**, *63*, 1715–1721.

44. Wang, J.; Li, L.; Liu, W.; Wang, Y.; Wang, Y.; Zhou, M. Sc2O3-W matrix impregnated cathode with spherical grains. *J. Phys. Chem. Solids* **2008**, *69*, 2103–

2108.

45. Vancil, B.; Schmidt, V.; Lorr, J.; Brodie, I. Scandate cathode with sharp transition. *14th IEEE Int. Vac. Electron. Conf. IVEC 2013 - Proc.* **2013**, *2*, 2–3.

46. Lesny, G.; Forman, R. Surface Studies on Scandate Cathodes and Synthesized Scandates. *IEEE Trans. Electron Devices* **1990**, *37*, 2595–2604.

47. Gs, G.; Geittner, P.; Lydtin, H.; Ritz, A. Emission properties of top-layer scandate cathode prepared by LAD. *Appl. Surf. Sci.* **1997**, *111*, 11–17.

48. Zagwijn, P.M.; Frenken, J.W.M.; Van Slooten, U.; Duine, P.A. A model system for scandate cathodes. *Appl. Surf. Sci.* **1997**, *111*, 35–41.

49. Shao, W.; Zhang, K.; Li, J.; Yan, S.; Chen, Q. Gas poisoning investigations of scandate and M-type dispenser cathodes. *Appl. Surf. Sci.* **2003**, *215*, 54–58.

50. Liu, X.; Zhou, Q.; Maxwell, T.L.; Vancil, B.K.; Beck, M.J.; Balk, T.J. Scandate cathode surface characterization: Emission testing, elemental analysis and morphological evaluation. *Mater. Charact.* **2019**, *148*, 188–200.

51. Wang, J.; Wang, Y.; Liu, W.; Li, L.; Wang, Y.; Zhou, M. Emission property of scandia and Re doped tungsten matrix dispenser cathode. *J. Alloys Compd.* **2008**, *459*, 302–306.

52. Lai, C.; Wang, J.; Zhou, F.; Liu, W.; den Engelsen, D.; Miao, N. Emission and evaporation properties of 75 at.% Re-25 at.% W mixed matrix impregnated cathode. *Appl. Surf. Sci.* **2018**, *427*, 874–882.

53. Gärtner, G.; Geittner, P.; Lydtin, H.; Ritz, A. Emission properties of top-layer scandate cathodes prepared by LAD. *Appl. Surf. Sci.* **1997**, *111*, 11–17.

54. Figner, A.L.; Judinskaja, R.N.A.V. Metal-porous body having pores filled with barium scandate 1967, 3–5.

55. Cronin, J.L. Modern Dispenser Cathodes. *IEE Proc. I - Solid State Electron Devices* 1981, *128*, 19–32.

56. Oostrom, A. Van; Augustus, L. Activation and early life of a pressed barium

scandate cathode. *Appl. Surf. Sci.* **1979**, *2*, 173–186.

57. Wang, J.; Liu, W.; Wang, Y.; Li, L.; Zhou, M. A study of pressed scandate dispenser cathode. *2008 IEEE Int. Vac. Electron. Conf. IVEC with 9th IEEE Int. Vac. Electron Sources Conf. IVESC* **2008**, 70–71.

58. Wang, J.; Liu, W.; Li, L.; Wang, Y.; Wang, Y.; Zhou, M. A study of scandia-doped pressed cathodes. *IEEE Trans. Electron Devices* **2009**, *56*, 799–804.

59. Cui, Y.; Wang, J.; Liu, W.; Wang, Y.; Zhou, M. Characterization of scandia doped pressed cathode fabricated by spray drying method. *Appl. Surf. Sci.* **2011**, *258*, 327–332.

60. Hasker, J.; Van Esdonk, J.; Crombeen, J.E. Properties and manufacture of top-layer scandate cathodes. *Appl. Surf. Sci.* **1986**, *26*, 173–195.

61. Uda, E.; Nakamura, O.; Matsumoto, S.; Higuchi, T. Emission and life characteristics of thin film top-layer scandate cathode and diffusion of Sc2O3and W. *Appl. Surf. Sci.* **1999**, *146*, 31–38.

62. Sasaki, S.; Yaguchi, T.; Mori, N.; Taguchi, S.; Shibata, M. Nonuniform emission distribution on a scandate impregnated cathode. *Appl. Surf. Sci.* **1999**, *146*, 17–21.

63. Wang, J.; Yang, Y.; Liu, W.; Wang, Y.; Wang, J. Advances in High Emission Sc 2 O 3 -W Matrix Cathode Materials. **2016**, *46*, 20–26.

64. Liu, W.; Zhang, K.; Wang, Y.; Pan, K.; Gu, X.; Wang, J.; Li, J.; Zhou, M. Operating model for scandia doped matrix scandate cathodes. *Appl. Surf. Sci.* **2005**, *251*, 80–88.

65. van Oostrom, A.; Augustus, L. Activation and early life of a pressed barium scandate cathode. *Appl. Surf. Sci.* **1979**, *2*, 173–186.

66. Hasker, J.; Esdonk, J.V.A.N.; Crombeen, J.E. Properties and manufacture of top-layer scandate cathodes. *Appl. Surf. Sci.* **1986**, *26*, 173–195.

67. Yamamoto, S.; Taguchi, S.; Watanabe, I.; Sasaki, S. Electron Emission Enhancement of a (W-Sc2O3) -Coated Impregnated Cathode by Oxidation of the

Coated Thin Film. *Jpn. J. Appl. Phys.* **1988**, *27*, 1411–1414.

68. Yamamoto, S.; Taguchi, S.; Aida, T.; Kawase, S. Study of metal film coating on Sc2O3 mixed matrix impregnated cathodes. *Appl. Surf. Sci.* **1984**, *17*, 517–529.

69. Hasker, J.; Crombeen, C. Scandium Supply After Ion Bombardment on Scandate Cathodes. *IEEE Trans. Electron Devices* **1990**, *37*, 2589–2594.

70. Wang, J.; Wang, Y.; Tao, S.; Li, H.; Yang, J.; Zhou, M. Scandia-doped tungsten bodies for Sc-type cathodes. *Appl. Surf. Sci.* **2003**, *215*, 38–48.

71. Yang, F.; Wang, J.; Wang, Y.; Liu, W.; Zhu, X. Investigation of Nanosized-Scandia-Doped Dispenser Cathodes With Machined Surfaces. *IEEE Trans. Electron Devices* **2016**, *63*, 1728–1733.

72. Wang, Y.; Wang, J.; Liu, W.; Liang, W.; Yang, F. Recent progresses on nanosized-scandia-doped dispenser cathodes. *IEEE Int. Vac. Electron. Conf. IVEC 2014* **2014**, 51–52.

73. Wang, Y.; Wang, J.; Liu, W.; Zhang, K.; Li, J. Development of high current-density cathodes with scandia-doped tungsten powders. *IEEE Trans. Electron Devices* **2007**, *54*, 1061–1070.

74. Zhao, J.; Li, N.; Li, J.; Barnett, L.R.; Banducci, M.; Gamzina, D.; Munir, Z.A.; Luhmann, N.C. High current density and long-life nanocomposite scandate dispenser cathode fabrication. *IEEE Trans. Electron Devices* **2011**, *58*, 1221–1228.

75. Yuan, H.; Gu, X.; Pan, K.; Wang, Y.; Liu, W.; Zhang, K.; Wang, J.; Zhou, M.; Li, J. Characteristics of scandate-impregnated cathodes with sub-micron scandia-doped matrices. *Appl. Surf. Sci.* **2005**, *251*, 106–113.

76. Wang, J.; Lu, H.; Liu, W.; Wang, Y.; Li, L.; Zhou, M. A Study of Scandia Doped Tungsten Nano-Powders. *J. Rare Earths* **2007**, *25*, 194–198.

77. Vancil, B.; Ohlinger, W.L.; Green, M.C.; Osborne, C.; Schmidt, V.; Vancil, A. New Findings on Powder Synthesis for Scandate Cathode Matrices. *IEEE Trans. Electron Devices* **2018**, *65*, 2077–2082.

78. Liu, W.; Zhang, K.; Wang, Y.; Pan, K.; Gu, X.; Wang, J.; Li, J.; Zhou, M. Operating model for scandia doped matrix scandate cathodes. *Appl. Surf. Sci.* **2005**, *251*, 80–88.

79. Liu, X.; Zhou, Q.; Maxwell, T.L.; Vancil, B.; Beck, M.J.; Balk, T.J. Characterization of a Scandate Cathode : High-Resolution Imaging , Chemical Analysis , and Emission Testing. *J. Vac. Sci. Technol. A* **2018**, 1–34.

80. Zhou, Q.; Liu, X.; Maxwell, T.; Vancil, B.; Balk, T.J. Ba x Sc y O z Adsorptions on W (001), (110), (112): Structural Stability , Work Functions and Equilibrium Crystal Shape. *Appl. Surf. Sci. Submitt.* **2017**, 1–26.

81. Koppius, O.G. Impregnateds for dispenser cathodes 1973.

82. van Stratum, A.J.A.; van Os, J.G.; Blatter, J.R.; Zalm, P. Barium-aluminum-scandate dispenser cathode 1977.

83. Eindhoven, T.U.; Magnificus, D.R. Surface Analysis of Thermionic Dispenser Cathodes. *Appl. Surf. Sci.* **2000**, *191*, 153–165.

84. Wang, Y.; Wang, J.; Liu, W. Development of scandate cathode and its prospect-A review. *2012 IEEE 9th Int. Vac. Electron Sources Conf. IVESC 2012* **2012**, 41.

85. Roquais, J.M.; Poret, F.; Le Doze, R.; Ricaud, J.L.; Monterrin, A.; Steinbrunn, A. Barium depletion study on impregnated cathodes and lifetime prediction. *Appl. Surf. Sci.* **2003**, *215*, 5–17.

86. Tomich, D.H.; Mescher, J.A.; Grant, J.T. Surface composition and barium evaporation rate of “pedigreed” impregnated tungsten dispenser cathodes during accelerated life testing. *Appl. Surf. Sci.* **1987**, *28*, 34–52.

87. Beck, M.J.; Zhou, Q.; Liu, X.; Maxwell, T.; Vancil, B.; Balk, T.J. The dipole model at the atomic scale: Explaining variations in work function due to configurational and compositional changes in Ba/Sc/O adsorbates on W (001), (110), and (112). In Proceedings of the 2018 IEEE International Vacuum Electronics Conference, IVEC 2018; 2018.

88. Zhou, Q.; Liu, X.; Maxwell, T.; Balk, T.J.; Beck, M.J.; Vancil, B. Mapping conditions for the formation of high-performance scandate cathodes: New insights into the role of sc. In Proceedings of the 2018 IEEE International Vacuum Electronics Conference, IVEC 2018; 2018.

89. Jacobs, R.M.; Morgan, D.; Booske, J.H. Emission energy barriers of scandate surfaces with adsorbed Ba and Ba-O using density functional theory. *14th IEEE Int. Vac. Electron. Conf. IVEC 2013 - Proc.* **2013**, 3–4.

90. Brodie, I.; Vancil, B. Electron emission microscopy of scandate cathode emission sites. *2016 29th Int. Vac. Nanoelectron. Conf. IVNC 2016* **2016**, 1–2.

91. Li, J.; Wang, H.; Yu, Z.; Gao, Y.; Chen, Q.; Zhang, K. Emission mechanism of high current density thermionic cathodes. *8th IEEE Int. Vac. Electron. Conf. IVEC 2007* **2007**, *2440*, 143–144.

92. Maloney, C.E. Characterization of an Impregnated Scandate Cathode Using a Semiconductor Model. *IEEE Trans. Electron Devices* **1994**, *41*, 2460–2467.

93. Muller, W. Work functions for models of scandate surfaces. *Appl. Surf. Sci.* **1997**, *111*, 30–34.

94. Jacobs, R.; Morgan, D.; Booske, J. Work function and surface stability of tungsten-based thermionic electron emission cathodes. *APL Mater.* **2017**, *5*.

95. Raju, R.S.; Maloney, C.E. Characterization of an Impregnated Scandate Cathode Using a Semiconductor Model. *IEEE Trans. Electron Devices* **1994**, *41*, 2460–2467.

96. Wright, D.A. Thermionic emission from oxide coated cathodes. *Proc. Phys. Soc. Sect. B* **1949**, *62*, 188–203.

97. Zhang, X.Z.; Wang, Y.M.; Wang, J.S.; Liu, W. Study of surface nano-particles of scandate cathodes. *Proc. - 2010 8th Int. Vac. Electron Sources Conf. Nanocarbon, IVESC 2010 NANOcarbon 2010* **2010**, 353–354.

98. Cui, Y.; Wang, J.; Liu, W. Preparation and characterization of scandia-doped tungsten powders prepared by a spray-drying method. *Res. Chem. Intermed.* **2011**,

37, 341–350.

99. Yamamoto, S. Fundamental physics of vacuum electron sources. *Reports Prog. Phys.* **2006**, *69*, 181–232.

100. Yamamoto, S.; Taguchi, S.; Watanabe, I.; Kawase, S. Electron emission properties and surface atom behavior of an impregnated cathode coated with tungsten thin film containing sc2o3. *Jpn. J. Appl. Phys.* **1986**, *25*, 971–975.

101. Zhou, Q.; Liu, X.; Maxwell, T.; Vancil, B.; Balk, T.J.; Beck, M.J. BaxScyOz on W (0 0 1), (1 1 0), and (1 1 2) in scandate cathodes: Connecting to experiment via μO and equilibrium crystal shape. *Appl. Surf. Sci.* **2018**, *458*, 827–838.

102. Trimby, P.W. Ultramicroscopy Orientation mapping of nanostructured materials using transmission Kikuchi diffraction in the scanning electron microscope. *Ultramicroscopy* **2012**, *120*, 16–24.

103. Zucker, R. V.; Chatain, D.; Dahmen, U.; Hagege, S.; Carter, W.C. New software tools for the calculation and display of isolated and attached interfacial-energy minimizing particle shapes. *J. Mater. Sci.* **2012**, *47*, 8290–8302.

104. Liu, W.; Wang, Y.; Wang, J.; Wang, Y.; Vancil, B. Emission characteristics of nanosized scandia-doped dispenser cathodes in open electron-gun structures. *IEEE Trans. Electron Devices* **2011**, *58*, 1241–1246.

105. Yuan, H.; Gu, X.; Pan, K.; Wang, Y.; Liu, W.; Zhang, K.; Wang, J.; Zhou, M.; Li, J. Characteristics of scandate-impregnated cathodes with sub-micron scandia-doped matrices. *Appl. Surf. Sci.* **2005**, *251*, 106–113.

106. Mroz, M.; Tenney, S.; Savina, T.; Kordesch, M.E. Thermionic emission microscopy of scandium thin film dewetting on W(100). *AIP Adv.* **2018**, *8*.

107. Wang, J.; Lu, H.; Liu, W.; Wang, Y.; Li, L.; Zhou, M. A Study of Scandia Doped Tungsten Nano-Powders. *J. Rare Earths* **2007**, *25*, 194–198.

108. Gärtner, G.; Geittner, P.; Raasch, D.; Wiechert, D.U. Supply and loss mechanisms of Ba dispenser cathodes. *Appl. Surf. Sci.* **1999**, *146*, 22–30.

109. Zagwijn, P.M.; Frenken, J.W.M.; van Slooten, U.; Duine, P.A. A model system for scandate cathodes. *Appl. Surf. Sci.* **1997**, *111*, 35–41.

110. Makarov, A.P.; Bersneva, E.U.; Zemchikhin, E.M.; Chistova, G.I. Emission properties, microstructure and surface composition of scandate impregnated cathodes with tungsten and a tungsten-rhenium matrix. *2014 10th Int. Vac. Electron Sources Conf. IVESC 2014 2nd Int. Conf. Emiss. Electron. ICEE 2014 - Proc.* **2014**, 2–3.

111. Lamartine, B.C.; Czarnecki, J. v.; Haas, T.W. Coadsorption of Ba and O on polycrystalline W. *Appl. Surf. Sci.* **1986**, *26*, 61–76.

112. Zhang, X.; Wang, J.; Wang, Y.; Liu, W.; Zhou, M.; Gao, Z. Investigation of influence of surface nanoparticle on emission properties of scandia-doped dispenser cathodes. *Funct. Mater. Lett.* **2013**, *6*, 1–5.

113. Zhao, J.; Gamzina, D.; Li, N.; Li, J.; Spear, A.G.; Barnett, L.; Banducci, M.; Risbud, S.; Luhmann, N.C. Scandate dispenser cathode fabrication for a high-aspect-ratio high-current-density sheet beam electron gun. *IEEE Trans. Electron Devices* **2012**, *59*, 1792–1798.

114. Zhou, Q.; Liu, X.; Maxwell, T.; Vancil, B.; Balk, T.J.; Beck, M.J. BaxScyOzon W (0 0 1), (1 1 0), and (1 1 2) in scandate cathodes: Connecting to experiment via μOand equilibrium crystal shape. *Appl. Surf. Sci.* **2018**, *458*, 827–838.

115. Nichols, M.H. The thermionic constants of tungsten as a function of crystallographic direction. *Phys. Rev.* **1940**, *57*, 297.

116. Fall, C.J.; Binggeli, N.; Baldereschi, A. Theoretical maps of work-function anisotropies. *Phys. Rev. B - Condens. Matter Mater. Phys.* **2002**, *65*, 1–6.

117. Tracy, J.C.; Blakely, J.M. A study of facetting of tungsten single crystal surfaces. *Surf. Sci.* **1968**, *13*, 313–336.

118. Liu, W.; Wang, J.; Wang, Y.; Cui, Y.; Zhang, X.; Zhou, M. XRD analysis of scandate cathodes. *2011 IEEE Int. Vac. Electron. Conf. IVEC-2011* **2011**, 407–408.

119. Norman, H.; Shoenbeck, L.; Shafer, R.; Ohlinger, W. Barium source material development for reservior hollow cathodes. *40th A/AA/ASME/SAE/ASEE Jt. Propuls. Conf. Exhib.* **2004**, 4209.

120. Schoenbeck, L. Investigation of Reactions Between Barium Compounds and Tungsten in a Simulated Reservoir Hollow Cathode Environment, Georgia Institute of Technology, 2005.

121. Wako, A.H.; Dejene, F.B.; Swart, H.C. Combustion synthesis, characterization and luminescence properties of barium aluminate phosphor. *J. Rare Earths* **2014**, *32*, 806–811.

122. Zhang, L.W.; Wang, L.; Zhu, Y.F. Synthesis and performance of BaAl2O4 with a wide spectral range of optical absorption. *Adv. Funct. Mater.* **2007**, *17*, 3781–3790.

123. Zhu, Z.; Li, X.; Hong, L.; Li, Y.; Sun, C.; Cao, Y. Synthesis and characterization of BaAl2O4 nanorods by a facile solvothermal method. *Mater. Lett.* **2012**, *86*, 1–4.

124. Wang, J.; Lai, C.; Liu, W.; Yang, F.; Zhang, X.; Cui, Y.; Zhou, M. Effect of scandia doping method on the emission uniformity of scandate cathode with Sc2O3–W matrix. *Mater. Res. Bull.* **2013**, *48*, 3594–3600.

125. Wang, J.; Li, L.; Liu, W.; Wang, Y.; Zhao, L.; Wang, Y. Preparation and characterization of scandia and Re doped tungsten matrix impregnated cathode. *J. Phys. Chem. Solids* **2007**, *68*, 2209–2215.

126. Vancil, B.; Ohlinger, W.; Green, M.; Osborne, C.; Schmidt, V.; Vancil, A. New Findings on Powder Synthesis for Scandate Cathode Matrices. **2017**, 0–5.

127. Fan, H.Y. Thermionic emission from an oxide-coated cathode. *J. Appl. Phys.* **1943**, *14*, 552–560.

128. Gaertner, G.; Barratt, D. Life-limiting mechanisms in Ba-oxide, Ba-dispenser and Ba-Scandale cathodes. *Appl. Surf. Sci.* **2005**, *251*, 73–79.

129. Li, J.; Wei, J.; Feng, Y.; Li, X. Effect of CaO on phase composition and properties of aluminates for barium tungsten cathode. *Materials (Basel).* **2018**, *11*, 1–10.

130. Jones, D.; McNeely, D.; Swanson, L.W. Surface and emission characterization of the impregnated dispenser cathode. *Appl. Surf. Sci.* **1979**, *2*, 232–257.

131. Ingram, P.K.; Wilson, G.J.; Devonshire, R. Measurement of the local work function of dispenser cathodes using an SPM technique. *Appl. Surf. Sci.* **1999**, *146*, 363–370.

132. Makarov, A.P.; Kultashev, O.K. A work model for barium dispenser cathodes with the surface covered by metal Os, Ir or Os <Ir> W alloy layer. *Appl. Surf. Sci.* **1997**, *111*, 56–59.

133. Swartzentruber, P.D.; John Balk, T.; Effgen, M.P. Correlation between microstructure and thermionic electron emission from Os-Ru thin films on dispenser cathodes. *J. Vac. Sci. Technol. A Vacuum, Surfaces, Film.* **2014**, *32*, 040601.

134. Taguchi, S.; Aida, T.; Yamamoto, S. Investigation of Sc2O3 Mixed-Matrix Ba-Ca Aluminate-Impregnated Cathodes. *IEEE Trans. Electron Devices* **1984**, *31*, 900–903.

135. Gibson, J.W.; Thomas, R.E.; Haas, G.A. Investigation of Scandate Cathodes: Emission, Fabrication, and Activation Processes. *IEEE Trans. Electron Devices* **1989**, *36*, 209–214.

136. Lei, C.; Wang, J.; Zhou, F.; Liu, W.; den Engelsen, D.; Miao, N. Emission and evaporation properties of 75 at.% Re-25 at. % W mixed matrix impregnated cathode. *Appl. Surf. Sci.* **2018**, *427*, 874–882.

137. Holzer, L.; Indutnyi, F.; Gasser, P.; Much, B.; Wegmann, M. Three-dimensional analysis of porous BaTiO3 ceramics using FIB nanotomography. *J. Microsc.* 2004, *216*, 84–95.

138. Slooten, U. Van; Duine, P.A. Scanning Auger measurements of activated and sputter cleaned Re-coated scandate cathodes. **1997**, *111*, 24–29.

139. Barik, R.K.; Singh, A.K.; Shukla, S.; Singh, T.P.; Raju, R.S.; Park, G.S. Development of Nanoparticle-Based High Current Density Cathode for THz Devices Application. *IEEE Trans. Electron Devices* **2016**, *63*, 1715–1721.

140. Mroz, M.; Tenney, S.; Savina, T.; Kordesch, M.E.; Mroz, M.; Tenney, S.; Savina, T.; Kordesch, M.E. Thermionic emission microscopy of scandium thin film dewetting on W (100) Thermionic emission microscopy of scandium thin film dewetting on W (100). **2018**, *065114*.

141. Kordesch, M.E.; Vaughn, J.M.; Wan, C.; Jamison, K.D. Model scandate cathodes investigated by thermionic emission microscopy. *Proc. - 2010 8th Int. Vac. Electron Sources Conf. Nanocarbon, IVESC 2010 NANOcarbon 2010* **2010**, *102*, 41–42.

142. Wan, C.; Kordesch, M.E. Tungstate formation in a model scandate thermionic cathode. *J. Vac. Sci. Technol. B, Nanotechnol. Microelectron. Mater. Process. Meas. Phenom.* **2013**, *31*, 011210.

143. Zhou, Q.; Liu, X.; Maxwell, T.; Vancil, B.; Balk, T.J.; Beck, M.J. BaxScyOz on W (001),(110), and (112) in Scandate Cathodes: Connecting to Experiment via μO and Equilibrium Crystal Shape. *Appl. Surf. Sci.* **2018**.

144. Hu, J.; Garner, A.; Ni, N.; Gholinia, A.; Nicholls, R.J.; Lozano-Perez, S.; Frankel, P.; Preuss, M.; Grovenor, C.R.M. Identifying suboxide grains at the metal-oxide interface of a corroded Zr-1.0%Nb alloy using (S)TEM, transmission-EBSD and EELS. *Micron* **2015**, *69*, 35–42.

145. Hasker, J.; Crombeen, J.E.; Van Dorst, P.A.M. Comment on Progress in Scandate Cathodes. *IEEE Trans. Electron Devices* **1989**, *36*, 215–219.

146. Yamamoto, S.; Taguchi, S.; Aida, T.; Kawase, S. Some fundamental properties of Sc2O3 mixed matrix impregnated cathodes. *Appl. Surf. Sci.* **1984**, *17*, 504–516.

147. Yuan, H.; Gu, X.; Pan, K.; Wang, Y.; Liu, W.; Zhang, K.; Wang, J.; Zhou, M.; Li, J. Characteristics of Scandate-type cathode with sub-micron structure Sc2O3 doped tungsten bodies. *IVESC2004 - 5th Int. Vac. Electron Sources Conf. Proc.* **2004**, *1*, 150–152.

148. Bao, J.X.; Wan, B.F.; Wang, P.J. Preparation and performance analysis of barium dispenser cathodes. *Vacuum* **2007**, *81*, 1029–1034.

149. Shih, A.; Yater, J.E.; Hor, C. Scandate cathode fundamentals: interactions of Ba, O

and Sc on W. *IVESC 2004. 5th Int. Vac. Electron Sources Conf. Proc. (IEEE Cat. No.04EX839)* **2004**, 57–58.

150. Wijangco, M.; Grant, T. Application of modern image analysis to quantify dispenser cathode surface condition. *Vac. Electron. Conf. 2004. IVEC 2004. Fifth IEEE Int.* **2004**, 146–147.

151. Kovaleski, S.D.; Burke, T. Life Model of Hollow Cathodes Using a Barium Calcium Aluminate Impregnated Tungsten Emitter. *27th Int. Electr. Propuls. Conf.* **2001**, 15–19.

152. Springer, R.W.; Haas, T.W. Auger electron spectroscopy study of cathode surfaces during activation and poisoning. I. the barium-on-oxygen-on-tungsten dispenser cathode. *J. Appl. Phys.* **1974**, *45*, 5260–5263.

153. Sharma, A.K.; Chopra, A.K.; Mathew, R. Emission poisoning studies on impregnated tungsten dispenser cathode under CO2, and O2 environment. *Appl. Surf. Sci.* **1989**, *40*, 97–101.

154. Yang, Y.; Wang, Y.; Liu, W.; Pan, Z.; Li, J.; Wang, J. Robustness investigation on nanosized-scandia-doped dispenser cathodes. *IEEE Trans. Electron Devices* **2018**, 1–5.

155. Liu, X.; Zhou, Q.; Maxwell, T.L.; Vancil, B.; Beck, M.J.; Balk, T.J. Analysis on faceted tungsten grains on the surfaces of scandate cathodes fabricated from L-S and L-L powders. *2018 IEEE Int. Vac. Electron. Conf.* **2018**, 323–324.

156. Szczepkowicz, A.; Bryl, R. From hill-and-valley faceting to global faceting of a crystal: Oxygen-covered tungsten. *Surf. Sci.* **2004**, *559*, 1–4.

157. Szczepkowicz, A.; Bryl, R. Observation of vertex-rounding transition for a crystal in equilibrium: Oxygen-covered tungsten. *Phys. Rev. B - Condens. Matter Mater. Phys.* **2005**, *71*, 10–13.

158. Tracy, J.C.; Blakely, J.M. The kinetics of oxygen adsorption on the (112) and (110) planes of tungsten. *Surf. Sci.* **1969**, *15*, 257–276.

Vita

Xiaotao Liu was born in Jingzhou, Hubei, China. He graduated from Central South University (China) with a Bachelor's degree of Powder Materials Science and Engineering (Powder Metallurgy) in 2012 and a Master's degree of Materials Engineering in 2015. He joined Dr. Balk's research group at University of Kentucky since Aug. 8th 2015 for the pursuit of a Ph.D. degree in Materials Science and Engineering.

Papers

Peer reviewed journal papers

1. **X. Liu,** B. K. Vancil, M. J. Beck and T. J. Balk, "Near-Surface Material Phases and Microstructure of Scandate Cathodes", Materials, 2019 12 (4), 636. doi:10.3390/ma12040636
2. **X. Liu**, Q. Zhou, T. L. Maxwell, B. K. Vancil, M. J. Beck and T. J. Balk, "Scandate Cathode Surface Characterization: Emission Testing, Elemental Analysis and Morphological Evaluation", Materials Characterization, 2019 (148), pp. 188-200. doi: 10.1016/j.matchar.2018.12.013
3. Q. Zhou, **X. Liu**, T. L. Maxwell, B. K. Vancil, T. J. Balk and M. J. Beck, "BaxScyOz on W (001), (110), and (112) in Scandate Cathodes: Connecting to Experiment via μO and Equilibrium Crystal Shape", Applied Surface Science, 2018 (458), pp. 827-838. doi: 10.1016/j.apsusc.2018.07.060
4. **X. Liu**, H. Ding, C. Yang, F. Liu, L. Huang, L. Jiang, "Microstructure and Mechanical Properties of Hot Extruded P/M FGH96 Superalloy", The Chinese Journal of Nonferrous Metals, 2016 (02), pp. 354-364.
5. C. Yang, **X. Liu**, J. Si, F. Liu, L. Jiang, "Processing Map and Cracking Behavior of Hot Extruded Powder Metallurgy Superalloy FGH96 During Hot Compression", The Chinese Journal of Nonferrous Metals, 2015 (10), pp. 2707-2719.
6. **X. Liu**, B. K. Vancil, M. J. Beck and T. J. Balk, "Unveiling the Ba-Sc-O Semiconducting Layer on the Emitting Surface of Scandate Cathodes", (2019, in preparation).
7. **X. Liu** and T.J. Balk, "Synthesis and Characterization of Nanoporous Stainless Steel via Thermal Dealloying", (2019, in preparation).

8. Q. Zhou, **X. Liu**, Mujan Seif, T. J. Balk and M. J. Beck, "Development of Scandate Cathode: A Review" (2019, in preparation).

Conference papers

1. **X. Liu**, Q. Zhou, T. Maxwell, B. K. Vancil, M. J. Beck, T. J. Balk, "Analysis of Faceted Tungsten Grains on the Surfaces of Scandate Cathodes Fabricated from L-S and L-L Powders", 2018 IEEE International Vacuum Electronics Conferences, pp. 323-324.
2. **X. Liu**, Q. Zhou, T. Maxwell, B. K. Vancil, M. J. Beck, T. J. Balk, "Characterization of Scandate Cathode at Different Stages of Processing", 2018 IEEE International Vacuum Electronics Conferences, pp. 233-234.
3. T. J. Balk, **X. Liu**, T. Maxwell, Q. Zhou, M. J. Beck, B. K. Vancil, "Materials Characterization of Surface Phases in Scandate Cathodes", 2018 IEEE International Vacuum Electronics Conferences, pp. 329-330.
4. Q. Zhou, **X. Liu**, T. Maxwell, B. K. Vancil, T. J. Balk, M. J. Beck, "Mapping Conditions for the Formation of High-Performance Scandate Cathodes: New Insights into the Role of Sc", 2018 IEEE International Vacuum Electronics Conferences, pp. 325-326.
5. T. L. Maxwell, **X. Liu**, Q. Zhou, M. J. Beck, B. K. Vancil, T. J. Balk, "Scandate Cathode Work Function Measurements at Elevated Temperature", 2018 IEEE International Vacuum Electronics Conferences, pp. 229-230.
6. M. J. Beck, Q. Zhou, **X. Liu**, T. Maxwell, B. K. Vancil, T. J. Balk, "The Dipole Model at the Atomic Scale: Explaining Variations in Work Function due to Configurational and Compositional Changes in Ba/Sc/O Adsorbates on W (001), (110), and (112)", 2018 IEEE International Vacuum Electronics Conferences, pp. 43-44.

Reviewed papers for journals

1. Metallurgical and Materials Transactions A (reviewed paper: 1)